מכון ויצמן למדע
WEIZMANN INSTITUTE OF SCIENCE

Thesis for the degree
Doctor of Philosophy

By

Alexander Kozlov

ϕ meson production in $d+Au$ and $Au+Au$ collisions at $\sqrt{s_{NN}}$ = 200 GeV using the PHENIX detector at RHIC

Advisor: Prof. Itzhak Tserruya

November 19, 2007

Submitted to the Scientific Council of the
Weizmann Institute of Science
Rehovot, Israel

ProQuest LLC
789 East Eisenhower Parkway
P.O. Box 1346
Ann Arbor, MI 48106-1346

I would like to dedicate this thesis to my little princess, Katya, my beloved wife, Anastasia, without whose support I would not have been able to complete this work and to my parents who have supported my thirst for knowledge all the way since the I remember myself.

Acknowledgments

A Ph.D. project carried out within the field of experimental particle physics relies on support, advice and encouragement of many people and it is my pleasure to thank all of them who made this thesis possible.

First of all, I express my sincere gratitude to my thesis supervisor Prof. Itzhak Tserruya for his guidance and support in the work leading to this dissertation. Professor Tserruya introduced me to the world of High Energy Physics and thus opened a new chapter in my life. From the beginning of my thesis research he has always being a patient, providing encouragement and valuable advices. His constructive criticisms at many critical points during my thesis work guided me to have a better understanding of the subject and resulted in a significant improvement of the quality of this thesis. I am especially grateful to him for his warm-hearted help in difficult moments of my life.

I would like to express my sincere thanks to Prof. Zeev Fraenkel and Dr. Ilia Ravinovich for their constant support, advices and encouragement during my research period. I also thank to Dr. Lev Shekhtman for sharing with me his experience on hardware.

I am thankful to the members of the Heavy-Ion Group at the Weizmann Institute, former and present ones, for their help, many fruitful discussions and friendly atmosphere in the group. I express my thanks to Alexander Milov, Boris Khachaturov, Alexander Cherlin, Dipali Pal & Debsankar Mukhopadhyay, Anand Dubey, Maxim Naglis and Deepali Sharma.

I thank to all the staff of the design department of the Weizmann Institute, the workshop, electronics and computing groups of the Physics Department for their help in my work. I am especially thankful to the Physics Department Secretary for their kind help and support which made my studies at the Weizmann Institute and stay in Israel much comfortable and enjoyable.

I would like to acknowledge the support by the Israel Science Foundation, the MINERVA Foundation and the Nella and Leon Benoziyo Center of High Energy Physics Research.

Abstract

The production of the ϕ meson in relativistic heavy-ion collisions is considered to be an important and powerful tool in the search for the predicted phase transition in hot and dense matter into a new state of matter referred to as a Quark-Gluon Plasma (QGP) that is characterized by the deconfinement of quarks and gluons and the restoration of chiral symmetry.

In particular, the ϕ meson may be sensitive to chiral symmetry restoration that could manifest itself through the modification of the ϕ-meson spectral properties (peak position and/or width) and changes in the yield measured through the e^+e^- channel compared to the K^+K^- channel.

This thesis comprises two parts. The first part is devoted to studies of the ϕ-meson production using the PHENIX detector which is the only experiment at the Relativistic Heavy-Ion Collider (RHIC) at BNL capable of measuring the ϕ meson via the dielectron decay mode. The thesis presents the first simultaneous measurement of the ϕ-meson production via the e^+e^- and K^+K^- decay channels in $Au+Au$ collisions at $\sqrt{s_{NN}}$ = 200 GeV using about one billion minimum bias events collected by PHENIX during Run 4 in 2004. The obtained results include the transverse mass distribution, the centrality dependence of the yield and the inverse slope parameter of the ϕ meson measured in the two decay channels. The results indicate a possible increase of the ϕ-meson yield in the dielectron channel with respect to the kaon one. The results are compared to measurements at lower energies at the AGS and SPS. The line-shape analysis of the ϕ meson from the $\phi \rightarrow K^+K^-$ analysis in $Au+Au$ collisions channel is presented as well. These results are complemented by the measurement of $\phi \rightarrow e^+e^-$ in the $d+Au$ collisions at $\sqrt{s_{NN}}$ = 200 GeV which provides an essential reference for comparison to the measurements in $Au+Au$ collisions.

The limited capability of the present configuration of the PHENIX detector to measure dielectron pairs from the decay of the light vector mesons and the low-mass pair continuum is expected to be greatly improved by the PHENIX upgrade with a Hadron Blind Detector (HBD) proposed and developed by our group at the Weizmann Institute. The second part of this thesis gives a description pf the HBD concept, the main elements of the detector and the results of a comprehensive R&D program that was undertaken to demonstrate the concept validity.

Contents

List of Figures

Chapter 1

Introduction

1.1 Quarks, gluons and QGP

It is now well established that hadrons are not the fundamental building blocks of matter, but rather contain more elementary particles, known as quarks [1–3]. According to the quark model, all hadrons are built up of quarks bound together in different ways. All the hadrons discovered so far are bound states of six $\frac{1}{2}$-spin quark and anti-quark flavors: up (u, $\bar{u}$), down (d, $\bar{d}$), strange (s, $\bar{s}$), charm (c, $\bar{c}$), bottom (b, $\bar{b}$) and top (t, $\bar{t}$). In this model the meson state consists of a quark and an anti-quark, $q\bar{q}$. The baryons (anti-baryons) are made of three quarks, qqq (anti-quarks, $\bar{q}\bar{q}\bar{q}$).

The existence of baryons containing three identical quarks motivated the introduction of a new quantum number, the *color charge*, to satisfy the Pauli principle. The color charge exists in three varieties: *red*, *blue* and *green*. However since all hadrons observed experimentally are neutral in their color charge the three quarks in the baryon must be selected in a colorless combination, *red-blue-green*, irrespectively of the quark flavors. The meson must have a quark of particular color and an anti-quark of the anti-color of the quark.

The interaction between quarks is described by the gauge theory of the strong force called Quantum Chromodynamics (QCD). In the QCD framework quarks of different colors interact by exchanging massless gauge fields, gluons. There are eight gluons which carry color charge and therefore interact both with quarks and gluons by exchanging other gluons.

The coupling constant of the strong interaction α_s depends on the momentum transfer of the interaction. At long distances (low momentum transfer) the coupling constant is strong leading to the phenomena of *quark confinement* and *chiral symmetry breaking*. Quark confinement is well known in nature reflected in the fact that quarks can be observed only in bound states (confined) as constituents of composite particles called hadrons. The quarks inside hadrons possess dynamically generated masses in the range of hundreds MeV, therefore leading to the approximate *chiral symmetry breaking*.

In contrast to that, at short distances (high momentum transfer), the coupling constant α_s decreases logarithmically leading to the effect of *asymptotic freedom* of quarks. In this regime the coupling constant is small and QCD processes can be described using perturbative methods.

The non-perturbative regime of QCD is treated by lattice QCD (lQCD) calculations, where the gauge theory of QCD is formulated on a discrete lattice of space-time. This approach has the advantage that it retains the fundamental characteristics of QCD and makes it possible to use computational methods to calculate the properties of quarks and gluons, e.g. the thermodynamic equation of state for strongly interacting matter, based on first principles.

Numerical calculations of QCD on the lattice predict a phase transition from a hadronic state at low energy densities to a new state of free quarks and gluons under conditions of high temperature and/or density in the system. This new state of matter is called the *Quark-Gluon Plasma* (QGP) [4]. In the QGP the quark confinement is broken, i.e. color degrees of freedom can propagate over distances much larger then the size of a hadron, and the approximate *chiral symmetry* of QCD is restored.

The latest and most accurate predictions of the phase transition are given by numerical solutions of the QCD Lagrangian on a lattice [5], see Fig. 1.1. There is a sharp transition of the energy density ε/T^4 at a critical temperature $T_c \approx 170$ MeV for different numbers of quark flavors. The expectation for an ideal gas with quark and gluon degrees of freedom, the Stefan-Boltzmann limit of the energy density, is also shown in Fig. 1.1. It is not reached even for temperatures four times larger than the critical temperature, indicating that the often used description of the QGP as a free gas of weakly interacting quarks and gluons may not be applicable at these temperatures [5].

A sketch of the current understanding of the phase diagram for the transition from a hadron gas to the QGP is shown in Fig. 1.2. At a vanishing baryon density ρ the critical temperature T_c of the phase transition is expected to be around ~ 170 MeV. At zero temperature the critical density for the phase transition is expected to be in the range between 5 and 10 times the ground state density of nuclear matter of $\rho_0 \approx 0.15$ GeV/fm^3. The two extreme cases of high-T and high-ρ phase transitions are connected to each other,

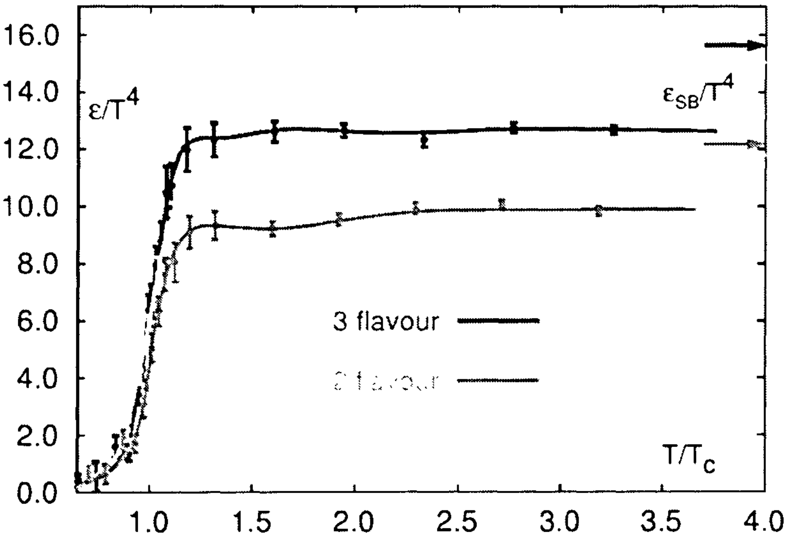

Figure 1.1: Lattice calculation of energy density in QCD [5], ε/T^4 as a function of the number of active quark flavors: 2 flavor (u, d), 3 flavor (u, d, s).

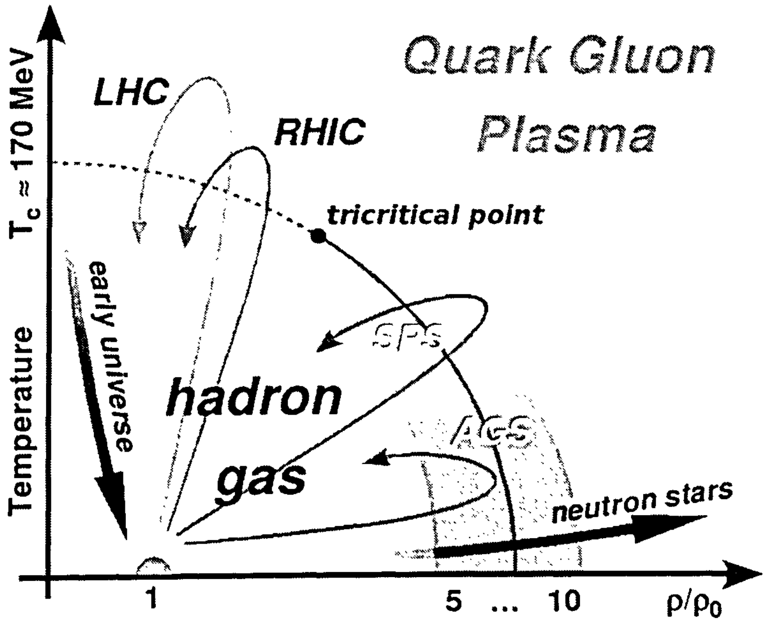

Figure 1.2: QCD phase diagram.

forming a phase boundary T_c (ρ). For $T(\rho) < T_c$ (ρ) the matter is effectively described in terms of hadronic degrees of freedom (baryons and mesons), whereas for T (ρ)> T_c (ρ) the effective degrees of freedom are the quarks and gluons.

Another ongoing discussion to which lQCD provides valuable insight is the nature of the phase transition. Recent developments in lQCD [6] indicate that the equation of state shows a critical point (Fig. 1.2) at a finite baryon density at which the phase transition turns from a rapid crossover (phase boundary is shown by dashed line) to a first order phase transition (solid line).

This transition is also interesting for cosmology and astrophysics. In the Big Bang scenario all the matter of the universe was in a QGP phase with high temperature and zero baryon density some 10 μs after the Big Bang. On the other hand the low temperature and high baryon density limit of the QGP, or even more exotic states of matter at zero temperature, may today exist in the center of neutron stars.

A second phase transition associated with QGP, closely related to the topic of this work, deals with the *chiral symmetry* of the QCD Lagrangian [7] and governs the spectrum of the lowest mass hadrons. The *chiral symmetry* is a $SU(3)_L \times SU(3)_R$ symmetry for the QCD Lagrangian in the limit of vanishing quark masses. This symmetry has several important implications. First, the quark helicity[1] is conserved in the strong interaction. Introducing the left and right chirality components of the quark fields, $q_{L,R} = \frac{1}{2}(1 \mp \gamma_5)q$, this would imply that the QCD Lagrangian can describe the dynamics of the left-handed, q_L, and right-handed, q_R, quarks separately. Second, the chirally symmetric spectrum of the hadronic multiplets is degenerate.

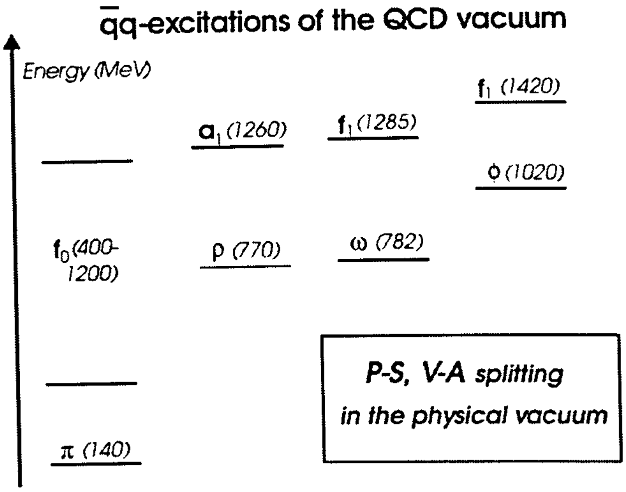

Figure 1.3: Experimentally measured spectrum of low-mass mesons.

---

[1] Helicity is the sign of the spin projection on its momentum direction.

However in the physical world, chiral symmetry is apparently spontaneously broken because the measured mass spectra of the chiral partners are split (Fig. 1.3). For example ρ(770)- and $a_1(1260)$-mesons show a large mass splitting (Δm = 500 MeV/c^2). Therefore, the ground state, i.e. the QCD vacuum, is not invariant under a chiral transformation. In particular, this leads to the formation of a *quark condensate*:

$$\langle \bar{q}q \rangle \equiv \langle \bar{q}_L q_R + \bar{q}_R q_L \rangle, \tag{1.1}$$

which is considered to be an order parameter of the chiral phase transition.

The *chiral condensate* vanishes in the chiral symmetric phase but becomes finite $\langle \bar{q}q \rangle \simeq$ -250 [MeV]^3 [8] in the asymmetric phase corresponding to a dynamical mixing of left- and right-handed quarks in the ground state. Fig. 1.4 shows the dependence of the *chiral condensate* on the temperature T and baryon density ρ of the system [9]. The dot indicates the position for normal nuclear matter and the shaded areas the regions, where experiments at different heavy-ion accelerators are expected to test the restoration of the *chiral symmetry*.

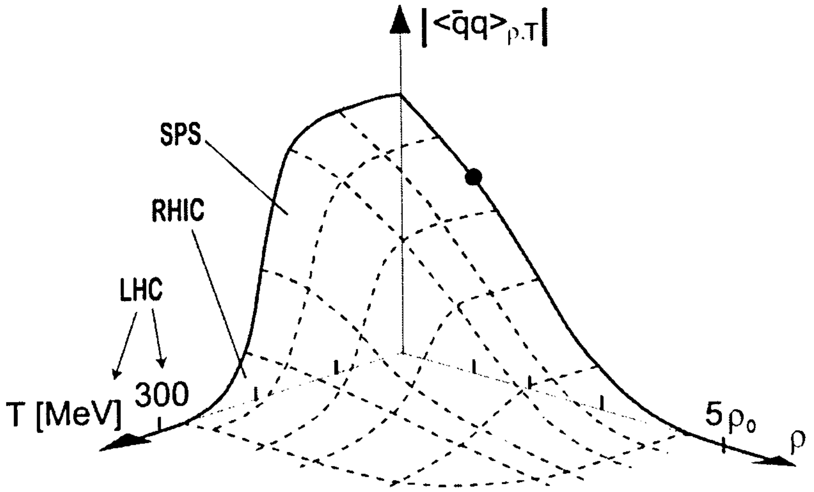

Figure 1.4: The *chiral condensate* as function of baryon density ρ and temperature T.

The spontaneously broken *chiral symmetry* has several important consequences on the hadronic properties and manifests itself in several ways:

(i) The QCD vacuum contains at any given time a certain number of $q\bar{q}$ pairs. These pairs can interact with a (massless) quark traversing the vacuum and change its helicity, as if it has mass. So it is most likely that the *chiral condensate*, $\langle \bar{q}q \rangle$, is responsible for generation of the *constituent* quark mass $m_q^* \simeq 350$ MeV which constitutes the major portion of the visible mass in the universe.

(ii) The existence of eight nearly massless bosons, so-called *Goldstone* bosons which can be identified with the light pseudo-scalar mesons, the pions, kaons and eta. The non-vanishing value of their mass is due to the explicit symmetry breaking. In the case of the pions the mass term is small.

(iii) hadronic states are split within the chiral multiplets with a substantial mass difference of $\Delta M \simeq 0.5$ GeV/c^2 .

1.2 Relativistic heavy-ion collisions

Significant progress in the heavy-ion program achieved in the last two decades at the accelerators around the world opened new perspectives in the experimental studies of strongly interacting matter at extreme conditions. The temperatures and energy densities obtained in the modern facilities are sufficient to study the possible transitions to the QGP phase which is perhaps the only QCD phase transition that can by studied in the laboratory [10].

The experimental heavy-ion program started at the BEVALAC at Berkeley, the UNILAC at Darmstadt in the mid-70's at energies 1-2 GeV per nucleon and expanded at the AGS (11-15 GeV per nucleon or $\sqrt{s_{NN}} \sim 5$ GeV) at Brookhaven National Laboratory and the SPS (158-200 GeV per nucleon or $\sqrt{s_{NN}} \sim$ 17-20 GeV) at CERN in the late 80's.

A new era in the search for the Quark Gluon Plasma started with the Relativistic Heavy-Ion Collider (RHIC) and associated physics program at Brookhaven National Laboratory that started operation in 2000 [11].

RHIC is a modern accelerator complex dedicated to the exploration of ultra-relativistic heavy-ion collisions. It is a very flexible machine in the choice of the colliding species and energies, colliding polarized protons at c.m. energies up to $\sqrt{s} = 500$ GeV and gold ions at c.m. energies up to $\sqrt{s_{NN}} = 200$ GeV , per pair of colliding nucleons. Details of the RHIC will be discussed in Section 2.1.

1.3 Probing hot and dense matter with the ϕ meson

The collision of heavy nuclei at high energies is a very short (a few fm/c) and complex dynamical process which ultimately results in a system consisting of thousands particles. In order to reconstruct the hot and dense early stage of the collision and study the dynamics of the processes leading to the very complicate final state a variety of experimental observables has been proposed. A comprehensive survey of the QGP signatures can be found in [12, 13].

Among these probes the production of the ϕ meson in nucleus-nucleus collisions is of considerable interest. The nature of the ϕ meson makes it a unique and powerful probe for the QGP phase. It can provide information on the possible *quark deconfinement* and *chiral symmetry restoration* expected in relativistic heavy-ion collisions. These new phenomena could manifest themselves in:

- ⇒ an enhancement of the ϕ-meson production due to strangeness enhancement.
- ⇒ modification of the ϕ spectral properties (peak position and/or width).
- ⇒ changes in the ϕ yield measured through the e^+e^- channel as compared to the K^+K^- channel.

1.3.1 The ϕ meson

The ϕ meson is a vector meson with *hidden strangeness* ($s\bar{s}$). Its quantum numbers, spectral properties and decay modes of interest in this work are listed in Table 1.1.

Table 1.1: ϕ-meson properties from PDG [14].

quark content	$s\bar{s}$	
quantum numbers, $I^G(J^{PC})$	$0^-(1^{--})$	
mass, (MeV/c^2)	$m = 1019.460 \pm 0.019$	
Full width, (MeV/c^2)	$\Gamma = 4.26 \pm 0.05$	
Decay mode:	$\phi \rightarrow K^+K^-$	$\phi \rightarrow e^+e^-$
Branching ratio:	$(49.2 \pm 0.6)\times 10^{-2}$	$(2.97 \pm 0.04)\times 10^{-4}$

1.3.2 The ϕ-meson production

The ϕ meson is the lightest hadron with *hidden strangeness*, $s\bar{s}$. Therefore in relativistic heavy-ion collisions its production is sensitive to the strangeness content of the created matter and affected by he Okubo-Zweig-Iizuka (OZI) rule. The OZI rule implies the suppression of the strong interaction processes with unconnected quark lines [2, 15, 16]. For example, since the ϕ-meson mass is slightly larger than the K^+K^- threshold the decay of the ϕ to K^+K^- is less favorable from the energy and phase space consideration than decay to $\phi \rightarrow \pi^+\pi^-\pi^0$. However the later decay requires the annihilation of the $s\bar{s}$ pair and therefore according to the OZI rule is suppressed. The OZI suppressed $\phi \rightarrow \pi^+\pi^-\pi^0$, and allowed, $\phi \rightarrow K^+K^-$, decay modes are shown in the left and right diagrams on Fig. 1.5.

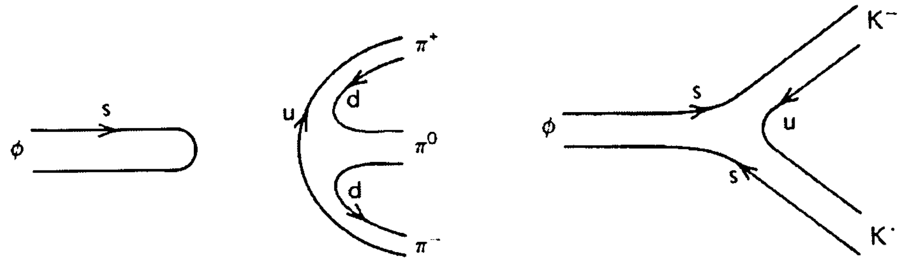

Figure 1.5: The diagrams of the $\phi \rightarrow \pi^+\pi^-\pi^0$ (left) and $\phi \rightarrow K^+K^-$ (right) decay modes.

The OZI rule is directly related to the asymptotic freedom of the strong interaction. In a process involving the strong interaction, when the initial and final states are connected by gluons only, the gluons must carry enough energy to create a quark and anti-quark pair. The coupling constant for these gluons is small since they are relatively energetic, especially for those gluons to produce heavier $s\bar{s}$ or even $c\bar{c}$ pairs. A small coupling constant means a small interaction magnitude, resulting in suppression of the ϕ decay and production in elementary collisions where no strangeness is available in the projectile/target.

Rafelski and Muller have conjectured that transition to the QGP phase is characterized by a large abundance of strange quarks [17, 18]. At temperatures below T_c the quark production is dominated by the *up* and *down* flavors. As the temperature approaches T_c and exceeds the rest mass of the $s\bar{s}$ pairs, $2m_s \simeq 300$ MeV, the strange quarks have similar probability to be produced. The copious production of strange quarks may lead to an increase in the ϕ yield since it can be formed by coalescence of strange quarks, bypassing the OZI rule. Enhanced production of the ϕ meson in heavy-ion collisions was suggested as a signature of QGP formation by Shor [19].

1.3.3 In-medium modification of the ϕ-meson spectral shape

The spectral properties of the vector mesons, *i.e.* the resonance widths and positions, under extreme conditions of temperature and density have been the subject of extensive theoretical studies. A variety of models have been used, including the Brown-Rho scaling based on an effective chiral Lagrangian [20], the QCD sum-rule approach [21], expanding thermal fireball model [22] and others. Theory predicts that the width and/or position of the resonances may be modified under extreme conditions of density and temperature and these modifications are considered to be important signals of the approximate restoration of chiral symmetry.

Among the vector mesons the ϕ is of particular interest due to several attractive features. First, the ϕ peak is well separated from the other resonances in the mass spectrum. Second, the scattering cross-section of the ϕ meson with non-strange hadrons is small [19]. Therefore the information about the primordial matter is less liable to be lost. Finally, the ϕ meson decays both to kaon pairs and, more rarely, to lepton pairs, both of which are detectable in high energy nuclear experiments.

The measurements of the hadronic *vs.* leptonic decay channels has long been suggested as a powerful tool to test possible in-medium modifications of the ϕ meson spectral properties. The ϕ-meson mass is close to the two-kaon threshold, m_ϕ - 2 $m_K \simeq 32$ MeV. Therefore, even small changes in the spectral properties of the ϕ or K can have an impact on the branching ratio of the $\phi \rightarrow K^+K^-$ decay. For example, models predicting a drop of the ϕ mass lead to the suppression of the dominant decay channel to K^+K^- pairs. In this case the relative branching ratios of the hadronic and leptonic decay channels should change dramatically.

The dileptons interact with the medium only electromagnetically providing a clean information on the ϕ meson properties at the time of decay while the hadronic channel could be affected by rescattering of the secondary kaons in the medium. Several theoretical attempts taking into account the in-medium modifications (mass and broadening) of kaons and ϕ mesons show an excess of the ϕ yield from the dilepton channel *vs.* the K^+K^- channel by a factor between 1.1 and 1.6 [23, 24].

The predictions on the mass and width of the ϕ meson from various models are summarized in Table 1.2. All models predict a decrease of the ϕ mass value varying from several ten up to about hundred of MeV/c^2 . More dramatic predictions are made for the modification of the ϕ width, which is expected to increase by several or even ten multiples above the PDG value of 4.26 MeV/c^2 .

Table 1.2: Theoretical predictions for the changes in the ϕ-meson properties.

Authors	Predictions, M_ϕ and Γ_ϕ in GeV/c^2
Lissauer and Shuryak [25]	$\Gamma_\phi \rightarrow 3\ \Gamma_\phi^{vacuum}$ at $T \approx T_c$
Bi and Rafelski [26]	$\Gamma_\phi \rightarrow 0.010$ at $T \approx T_c$
Blaizot and Mendez Galain [27]	$M_\phi \rightarrow 2M_K$ at $T \approx T_c$
Ko, Levai, Qiu and Li [28]	$M_\phi \rightarrow 0.990$, $\Gamma_\phi \rightarrow 0.400$ at $\rho_c \approx 5\rho_0$
Asakawa and Ko [29]	$M_\phi \rightarrow 0.750$ at $T \approx T_c$ and $\rho_c \approx 4\rho_0$
Asakawa and Ko [30, 31]	Double ϕ peak structure, $M_\phi^{lowpeak} \approx 0.880$ at $T \approx T_c$
Kuwabara [32]	$M_\phi \rightarrow 0.900$ at $\rho_c \approx 2\rho_0$
Song [33]	$M_\phi \rightarrow 1.000$ at $T = 200$ MeV
Bhattacharyya [34]	$M_\phi \rightarrow 1.000$, $\Gamma_\phi \rightarrow 0.028$ at $T = 200$ MeV
Smith and Haglin [35]	$\Gamma_\phi \rightarrow 0.014 \sim 0.028$ at $T \approx T_c$
Pal, Ko and Lin [23]	$M_\phi \rightarrow 0.970$, $\Gamma_\phi \rightarrow 0.045$ at $\rho_c \approx 2\rho_0$
Rapp (2002) [22]	Tail towards low masses (see Fig. 1.6)

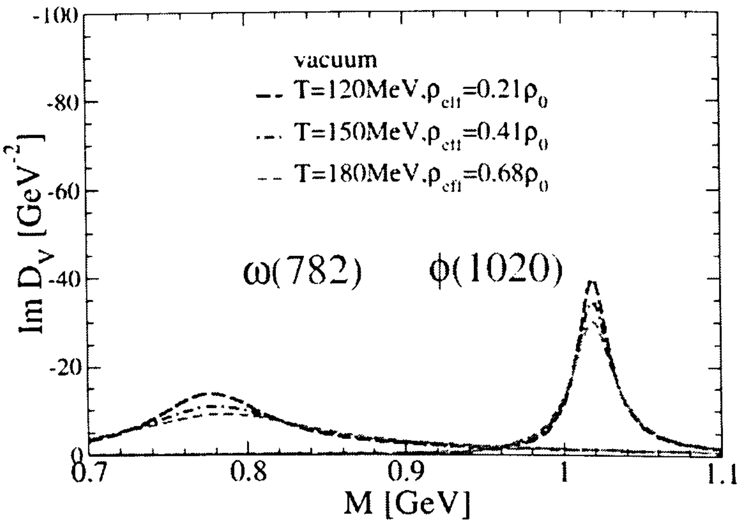

Figure 1.6: Spectral functions of the ω and ϕ mesons in vacuum (solid lines) as well as in hot baryon-poor hadronic matter as expected under RHIC conditions (long-dashed, dash-dotted and short-dashed lines) [22].

1.4 Experimental background at low energies.

Studies of the ϕ production Experimentally, the ϕ-meson production in heavy ion collisions has been studied for different colliding energies and species by various experiments at the AGS (BNL) and SPS (CERN) facilities. It has also been studied in elementary reactions.

The first measurements of the ϕ meson at AGS energies was performed by the E802/E859 collaboration in 14.6 GeV/c $Si+Au$ collisions using identified K^+K^- pairs [36]. The ϕ yield measured relative to the K^- production in the 7% most central collisions was found to be consistent with the production in $p+p$ collisions. The E917 collaboration studied the ϕ production in $Au+Au$ collisions at a beam energy 11.7 GeV/c as a function of collision centrality [37]. The measured ϕ yield per participant showed a steady rise toward central collisions which was stronger than that of non-strange mesons as seen from the increasing ϕ/π ratio with centrality. The ratios ϕ/K^+ and ϕ/K^- were approximately flat with the number of participants. The ϕ yield, ϕ/π and ϕ/K^+ ratios measured by the E917 collaboration are shown in Fig. 1.7. The peak position, m_ϕ, and width, Γ_ϕ, extracted from the fit of the signal distribution by the E802 and E917 experiments were found in agreement with the PDG values [36, 37]. No measurement of ϕ production through the $l\bar{l}$ decay channel was performed at the AGS.

At SPS energies, the ϕ production was explored in central nucleus-nucleus collisions at a beam energy of 158A GeV/c by several collaborations. The ϕ rapidity density, dN/dy measured in central Pb + Pb collisions via the muon decay channel by the NA50 collaboration [38] is about a factor 2-4 higher than the one obtained by the NA49 experiment via the K^+K^- channel in the same transverse momentum range [39]. In addition, the transverse momentum spectra determined by NA50 and NA49 have different inverse slope parameters, both in the absolute value and in the trend as a function of the number of participants. NA49 observes a significantly higher T parameter value, and an increase with centrality, while NA50 observes no dependence on centrality. It has been argued that the incompatibility between the two measurements could be attributed to the different channels probed [40].

The CERES collaboration reported results on the first attempt to measure the ϕ-meson production through e^+e^- and K^+K^- decay channels simultaneously within the same experiment. Both the ϕ rapidity density and shape of the transverse momentum spectra from the two decay channels were measured in central Pb + Au collisions at E_{lab} = 158A GeV/c [41] and found to be in agreement within the large experimental errors mainly of the e^+e^- decay channel. The CERES results could rule out a possible

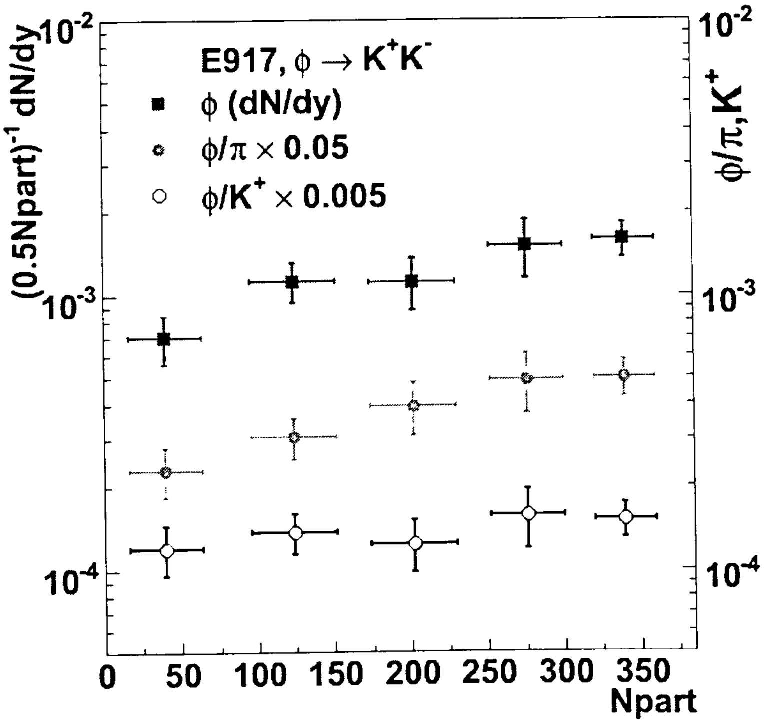

Figure 1.7: The ϕ yield per participant (solid squares), and the ϕ/π (solid circles) and ϕ/K^+ (open circles) ratios as a function of number of participants measured by the E917 collaboration [37].

enhancement of the ϕ yield in the leptonic *vs.* hadronic decay channel by a factor larger than ~ 2. Fig. 1.8 shows a comparison of the m_T spectra measured by NA49, NA50 and CERES.

Recently, the NA60 collaboration presented high quality results of the $\phi \rightarrow \mu^+\mu^-$ decay in $In+In$ collisions at 158*A* GeV/*c* [42]. The inverse slope as well as the average m_T parameters measured by NA60 as a function of centrality agree with the values measured by NA49.

The results obtained by the CERES and NA60 collaborations point to the conclusion that the difference between the NA49 and NA50 measurements cannot be attributed to the different decay channels probed.

Studies of the ϕ meson in-medium modifications The lifetime of the fireball created in relativistic heavy-ion collisions is smaller compared to the lifetime of the ϕ meson, $\tau_\phi \approx 46$ fm/*c*. Therefore, only a small fraction of the ϕ mesons will decay inside the fireball and if their spectral function is affected in the medium a distortion of the line-

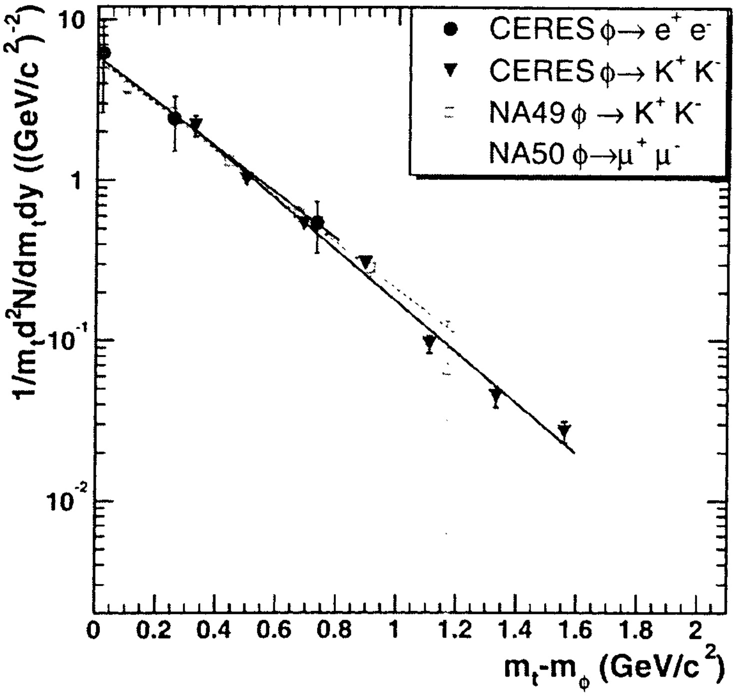

Figure 1.8: Transverse mass distribution of ϕ mesons measured by CERES in K^+K^- (triangles) and e^+e^- (circles) decay mode [41] compared to the results from NA49 (squares) [39] and NA50 (diamonds) [38]. The CERES spectra are scaled to account for the different measurement conditions. Error bars are statistical and systematic errors in the kaon channel are shown as boxes.

shape could be observed. For example, a low-mass tail should develop if the meson mass decreases in the medium. The observation of such distortion is very difficult but possible under good signal to background condition and with a high mass resolution through the dilepton decay channel. And indeed, the ϕ-meson modification was seen at normal nuclear matter by the E325 experiment at KEK proton synchrotron. Having an excellent mass resolution σ_{exp} = 10.7 MeV/c^2 and S/B ratio of the order of $\sim$ 1 the experiment reported recently on the first observation of spectral modification of the ϕ meson in cold nuclear matter trough the $\phi \rightarrow e^+e^-$ decay channel in 12 GeV $p+Cu$ interactions [43, 44]. The spectrum of the low momentum e^+e^- pairs ($\beta\gamma < 1.25$) is shown in Fig. 1.9. The tail to lower masses is interpreted as the evidence for the modification of the ϕ-meson line shape. This observation is in qualitative agreement with theoretical studies that link the ϕ-meson mass to the chiral condensate and predict that the ϕ-meson mass decreases even at normal nuclear matter density [45–47]. It should be emphasized that a similar enhancement of the ω- meson low-mass tail was observed by the E325 [48] experiment in 12 GeV $p+A$

collision and by CBELSA/TAPS [49] in the photo-production of ω mesons on nuclei.

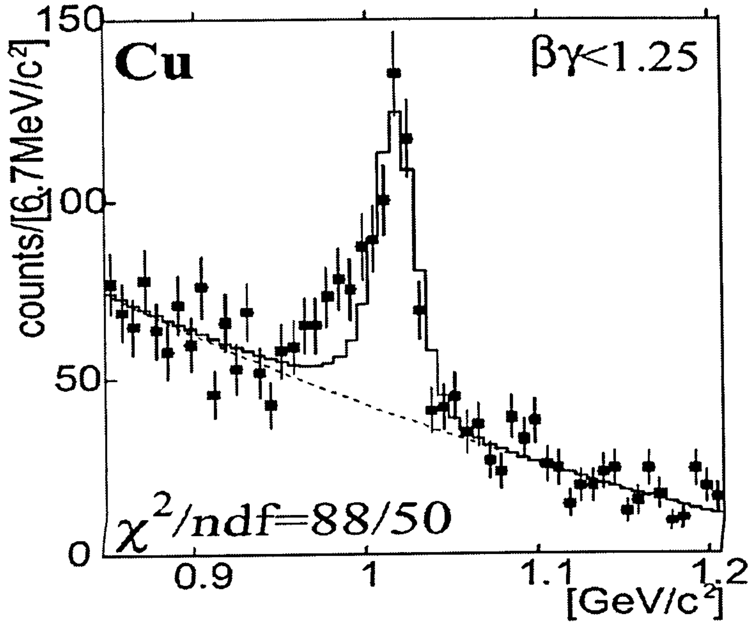

Figure 1.9: The e^+e^- invariant mass spectrum for the ϕ at low momentum region ($\beta\gamma_\phi < 1.25$) measured by the E325 experiment at KEK PS [43, 44].

At SPS experiments the observation of such modifications is extremely difficult due to poor signal to background ratio or limited mass resolution in the ϕ-mass region. The pioneering CERES dielectron results and the more recent NA60 dimuon results showed the clear evidence of in-medium modifications of the ρ-meson in $Pb+Au$ and $In+In$ collisions at 158 A GeV/c [50, 51]. However the studies of the ϕ meson through the e^+e^- and $\mu^+\mu^-$ decay channels by the CERES ($\sigma_{exp} \sim 7\%$ at m_ϕ at $S/B \sim 1/20$) and NA60 (σ_{exp} = 23 MeV/c^2 at m_ϕ) experiments, respectively, did not provide any conclusive or precise result on the ϕ-meson spectral function.

1.5 Thesis outline

As discussed in Section 1.3.3 the study of the ϕ-meson via hadronic and leptonic decay channels is considered to be a sensitive probe for in-medium modifications of the ϕ meson. The PHENIX detector has the capability to measure the ϕ-meson production through the e^+e^- and K^+K^- decay channels simultaneously. Furthermore, with its excellent mass resolution the PHENIX detector has the potential to measure precisely the properties of the light vector mesons. However in the present detector configuration the capability to measure e^+e^- pairs in the low-mass region is severely limited due to the huge combinatorial background originating from unrecognized γ-conversions and π^0-Dalitz decays resulting in very large statistical and systematic uncertainties. To solve this problem we have developed a Hadron Blind Detector (HBD) - a novel Čerenkov detector which will considerably improve the capability of the PHENIX detector to measure low-mass electron pairs.

This thesis comprises two parts:

a) we present the measurements of the ϕ-meson production through the e^+e^- and K^+K^- decay channels in $Au+Au$ collisions at $\sqrt{s_{NN}}$ = 200 GeV and through the e^+e^- decay channel in $d+Au$ collisions at $\sqrt{s_{NN}}$ = 200 GeV using the PHENIX detector at Relativistic Heavy-Ion Collider (RHIC)

b) We describe and present the main results of the HBD R&D program.

The experimental facilities including the RHIC accelerator complex and the PHENIX detector are introduced in Chapter 2. This is followed by the description of the analysis methods given in Chapter 3 and by the presentation of results and discussions given in Chapter 4. Finally, in Chapter 5 the concept, main elements and results of a comprehensive R&D program in the HBD will be presented.

Chapter 2

Experimental apparatus

2.1 Relativistic Heavy-Ion Collider

The Relativistic Heavy Ion Collider (RHIC) [11] at Brookhaven National Laboratory is a collider-type accelerator with two accelerating rings. This is a very flexible machine. It is capable of accelerating a wide variety of species from protons to Au ions up to a maximum center of mass energy of $\sqrt{s_{NN}}$ = 200 GeV for heavy ion beams and $\sqrt{s}$ = 500 GeV for protons.

A schematic diagram of the whole RHIC complex, including the various facilities used to produce and pre-accelerate the beams of particles is shown in Fig. 2.1. The RHIC complex consists of Tandem Van de Graaff, Linear Accelerator (LINAC) for proton injection, booster, Alternating Gradient Synchrotron (AGS) and RHIC main rings. The collider consists of two concentric accelerator/storage rings on a common horizontal plane, one (*Blue Ring*) for clockwise and the other (*Yellow Ring*) for counter-clockwise beams. The rings have a circumference of approximately $\sim$ 3.8 km and are designed to intersect at six locations. In four of the six collision points, there are detectors designed to study heavy-ion collisions: STAR [52], PHOBOS [53], BRAHMS [54] and PHENIX [55].

Since the commissioning of RHIC in June 2000, there have been six running periods which have delivered four $Au+Au$ physics runs, two $Cu+Cu$ physics run, one $d+Au$ physics run and five $p+p$ physics runs. The main parameters of the RHIC are presented in Table 2.1.

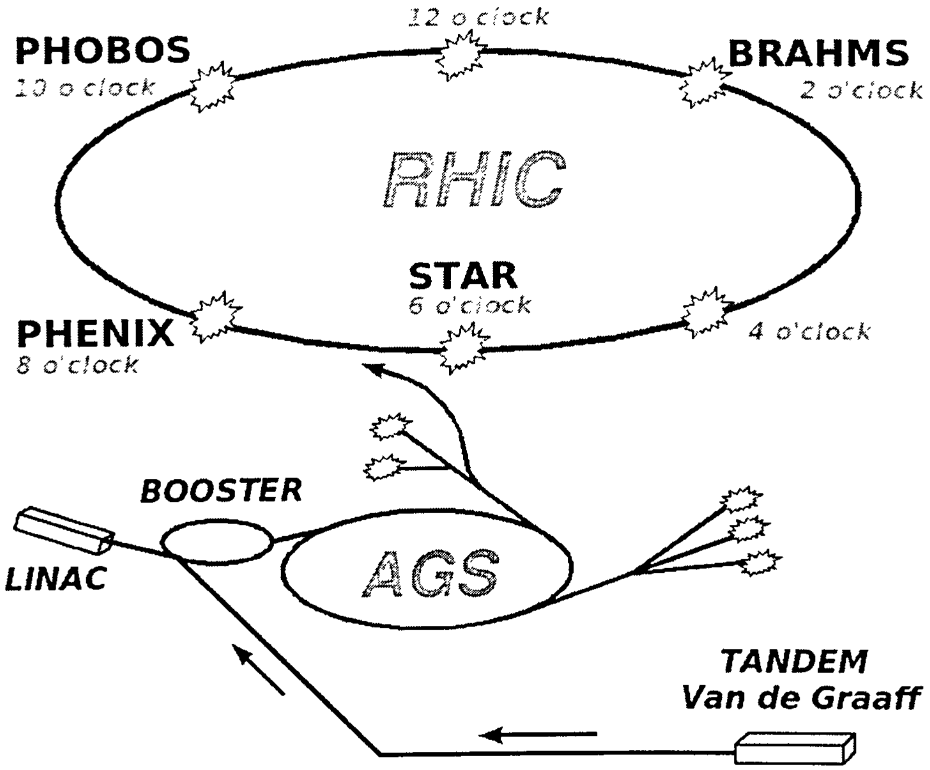

Figure 2.1: The Relativistic Heavy Ion Collider (RHIC) accelerator complex at Brookhaven National Laboratory.

Table 2.1: Summary of the RHIC main parameters.

Number of acceleration rings	2	
Number of bunches per ring	60	
Bunch spacing	213 ns	
Beam life time	~ 10 hours	
Number of interaction regions	6	
	$Au+Au$ collisions	$p+p$ collisions
Maximum energy $\sqrt{s_{NN}}$	200	500
Number of particles per bunch	$\sim 10^{9}$	$\sim 10^{11}$
Mean luminosity at top energy ($cm^{-2}s^{-1}$)	2×10^{26}	1.4×10^{31}
Maximum event rate (kHz)	~14	~8000

2.2 The PHENIX detector

2.2.1 Overview

Out of the four experiments associated with the heavy-ion program at the RHIC, PHENIX is the only detector specially designed to measure electromagnetic probes as well as hadrons.

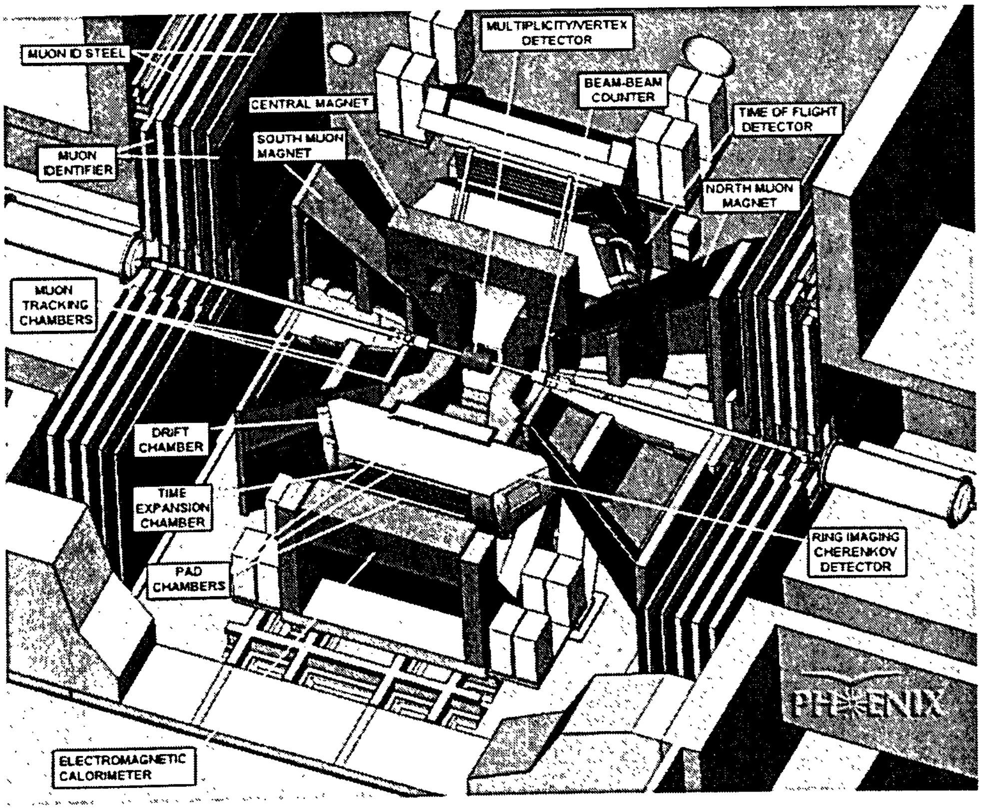

Figure 2.2: The PHENIX detector set-up.

The layout of the PHENIX detector is shown in Fig. 2.2. It consists of four spectrometers: two central arm spectrometers, each covering 90° in azimuth and $|\eta| < 0.35$ and operating in an axial magnetic field parallel to the beam axis provided by the Central Magnet (CM) and two forward muons spectrometers with full azimuthal coverage in the pseudo-rapidity range $1.1 < |\eta| < 2.4$ and dedicated magnets that provide a radial magnetic field. The Central Magnet utilizes two coils, outer and inner, that can be energized in different configurations to achieve the required magnetic field levels, depending on physics requirements. During the first three runs only the outer central coils were energized giving an effective field integral of $\int Bdl = 0.78$ (T$\cdot$ m). Following the convention accepted in PHENIX and in this thesis, the field configuration with only outer coils energized is referred as $+$ and $-$ for the normal and reversed fields, respectively. In 2004 the inner coil was added to the central arm magnet system as part of the original design of the PHENIX detector. With the inner coil it is possible to perform measurements with different magnetic field configurations in the central arm:

- $++$ and $--$ configuration, left panel in Fig. 2.3. These field configurations give an effective field integral of $\int Bdl = 1.15$ (T$\cdot$ m) which improves the momentum resolution.
- $+-$ compensating mode, right panel in Fig. 2.3. The operation with an opposite coil polarization (the effective field integral of $\int Bdl = 0.43$ (T$\cdot$ m)) results in an almost field free region close to the vertex up to a radial distance of $\sim$ 60 cm. This configuration is essential for the operation of the HBD detector (see Chapter 5).

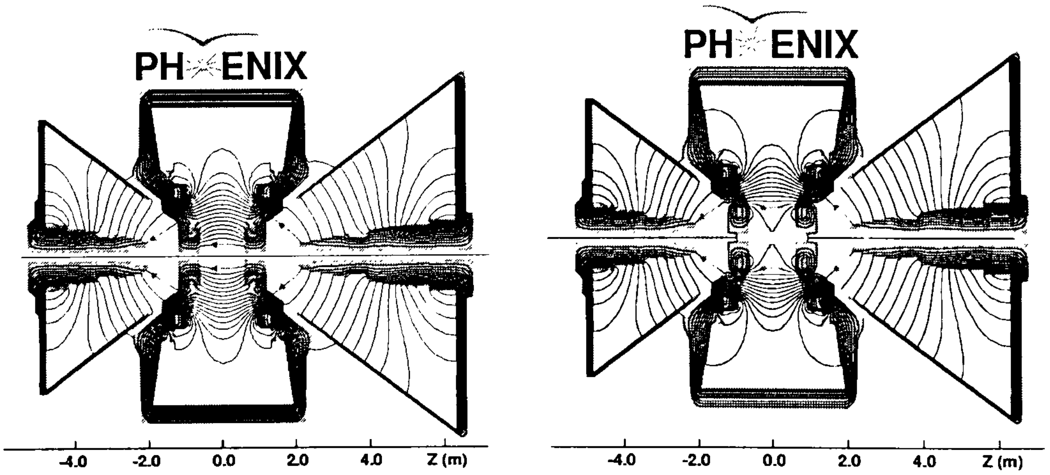

Figure 2.3: Magnetic field lines in the PHENIX detector, for the two central magnet coils in $++$ (left) and $+-$ (right) modes.

The configuration of the PHENIX detector in Run 3 and X, Y and Z of the global PHENIX coordinate system are shown in Fig. 2.4. The collisions take place inside the beam pipe which is surrounded by the Multiplicity and Vertex Detector (MVD). The first detector in the Central Arm shown on the top panel of Fig. 2.4 is the Drift Chamber (DC). Together with the Pad Chambers (PC1) positioned on the back side of the DC, it gives high resolution tracking of particles and provides the momentum measurement.

The Pad Chambers are followed by the Ring Imaging Cerenkov detector (RICH), which provides electron identification. In the West Arm the RICH is followed by two

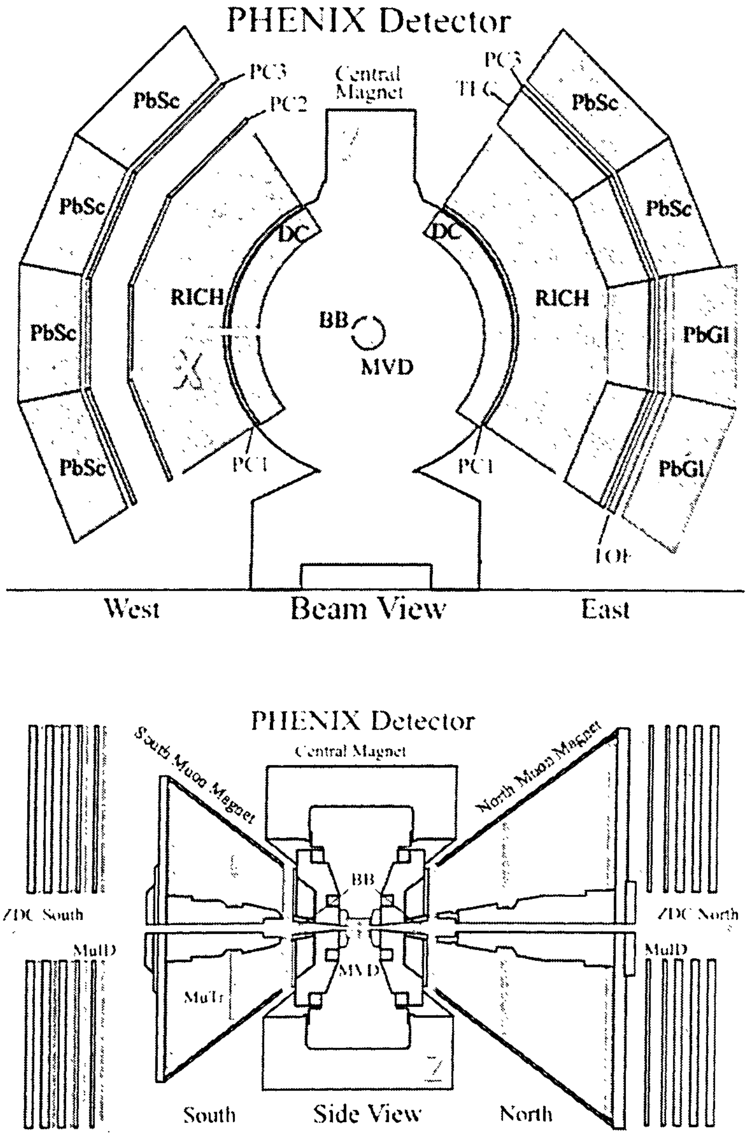

Figure 2.4: View of the PHENIX detector in Run 3 across (top) and along (bottom) the beam direction. The PHENIX global coordinate system X, Y, Z is also shown.

sets of Pad Chambers (PC2 and PC3). In the East Arm the RICH is followed by a Time-Expansion Chamber followed by Pad Chambers (PC3) and a Time-of-Flight (TOF) wall that covers the lower two sectors of the East Arm.

The last layer of the Central Arms is the Electro-Magnetic Calorimeter (EMC). Two types of calorimeters are used in PHENIX: the lead-scintillator (PbSc) in the West arm and two upper sectors of the East arm and the lead-glass (PbGl) behind the TOF wall.

The muon arm of the PHENIX is shown on the bottom panel of Fig. 2.4. It consists of the Muon Trackers (MuTr) contained inside the lampshade of the Muon Magnets followed by the panels of the Muon Identifier (MuID).

The configuration of the PHENIX detector in Run 4 is almost identical to the Run 3 configuration with the following changes:

- The Multiplicity/Vertex Detector (MVD) used in Run 3 was partially disassembled in Run 4. The barrel part was removed and only the end-cups were used. This reduced the amount of material in the central part of the PHENIX detector reducing the background of electrons from conversions.
- In Run 4 the PHENIX detector was upgraded with an Aerogel Čerenkov detector, installed in the West Arm, in front of one sector of the EMCal, to improve particle identification at high p_T.

2.2.2 PHENIX performance

The collision species, energy, and integrated luminosity of the various runs are listed in Table 2.2. The analysis presented in this report is based on the $d+Au$ data taken in Run 3 and the $Au+Au$ data taken in Run 4 both at $\sqrt{s_{NN}}$ = 200 GeV. Details on the Run 3 and Run 4 conditions are given in Table 2.3.

Table 2.2: List of the physics runs and corresponding parameters in the PHENIX experiment.

RUN	Year	Species	$\sqrt{s_{NN}}$ (GeV)	$\int Ldt$	N$_{evt}$ (10^6)
Run 1	2000	$Au+Au$	130	1 mb^{-1}	10
Run 2	2001/2002	$Au+Au$	200	24 mb^{-1}	170
		$p+p$	200	0.15 pb^{-1}	3700
Run 3	**2002/2003**	$d+Au$	**200**	**2.74** nb^{-1}	**5500**
		$p+p$	200	0.35 pb^{-1}	6600
Run 4	**2003/2004**	$Au+Au$	**200**	**241** μb^{-1}	**1530**
		$Au+Au$	62.4	0.35 pb^{-1}	58
Run 5	2004/2005	$Cu+Cu$	200	3.06 nb^{-1}	1780
		$Cu+Cu$	62.4	190.2 μb^{-1}	425
		$p+p$	200	3.78 pb^{-1}	85100
Run 6	2006	$p+p$	200	2.7+7.5 pb^{-1}	

Table 2.3: Details on the PHENIX Run 3 and Run 4 conditions.

	Run 3	Run 4
Maximum trigger rate (kHz)	~ 1.2	~ 1.8
Archiving rate (MB/s)	~ 120	~ 350
Minimum bias event size (kbyte/event)	130	180

2.2.3 The PHENIX subsystems used in the analysis

The analysis described below utilizes mainly a set of detectors for global event characterization and three sets of detectors from the central arm:

- High resolution tracking devices to define the trajectory and momentum of the particle.
- Detectors for electron identification.
- Detectors for kaon identification.

Global detectors The centrality and minimum bias trigger are determined by the beam-beam counters (BBC) [56] and zero-degree calorimeters (ZDC) [57] located at each side of the interaction point around the beam direction. BBC (see the bottom panel of Fig. 2.4) consists of two identical counters BBC^{North} and BBC^{South} each equipped with an array of 64 quartz Čerenkov detectors and positioned 1.4 m from the interaction point. The BBC's also provide the z-coordinate of the collision vertex (z_{vtx}) and the time reference (t^0_{BBC}) for the time-of-flight measurements. z_{vtx} and t^0_{BBC} are determined as

$$t^0_{BBC} = \frac{1}{2}(t^{North}_{BBC} + t^{South}_{BBC}); \qquad z_{vtx} = \frac{c}{2}(t^{North}_{BBC} - t^{South}_{BBC}); \tag{2.1}$$

where t^{North}_{BBC} and t^{South}_{BBC} are the collision time measured with respect to the RHIC collider clock by the BBC_{North} and BBC_{South}. The BBC has a high time resolution $\tau = 52 \pm 4$ ps which allows to measure the vertex position in central $Au+Au$ collisions with an accuracy better than 0.3 cm.

The ZDC's are small transverse area hadron calorimeters, ZDC^{North} and ZDC^{South} (see the bottom panel of Fig. 2.4) positioned 18 m from the interaction point along the beam axis.

Tracking detectors The charged particle momentum and trajectory are determined by the Drift Chamber (DC) and the Pad Chambers (PC) [58]. The PHENIX Drift Chamber system is a multiwire detector of cylindrical shape located at a radial distance of 244 cm from the beam line. Each DC arm covers 90° in azimuth, $|\eta| < 0.35$ and consists of six wire planes stacked radially:

- The X1 and X2 wire planes perform precise track measurements in the $r - \varphi$ plane.
- U1,V1 and U2,V2 wire modules are placed after X1 and X2, respectively. They contribute to the measurements of the z-coordinate of the track and reduce tracking ambiguities.

The main purpose of the DC is an accurate measurement of charged particle tracks in the $r - \varphi$ plane used to determine the transverse momentum p_T. The momentum resolution is given by:

$$\delta p/p = \sigma_{m.s.} \oplus \sigma_{DC} \cdot p(GeV/c) \tag{2.2}$$

where $\sigma_{m.s.}$ is the contribution due to multiple scattering and σ_{DC} is the intrinsic momentum resolution of the DC. The measured value of σ_{DC} scales with the magnetic field strength and was found to be $\sim$ 1.1 and 0.76% in Run 3 and Run 4, respectively. The multiple scattering term $\sigma_{m.s.}$ is below 1%.

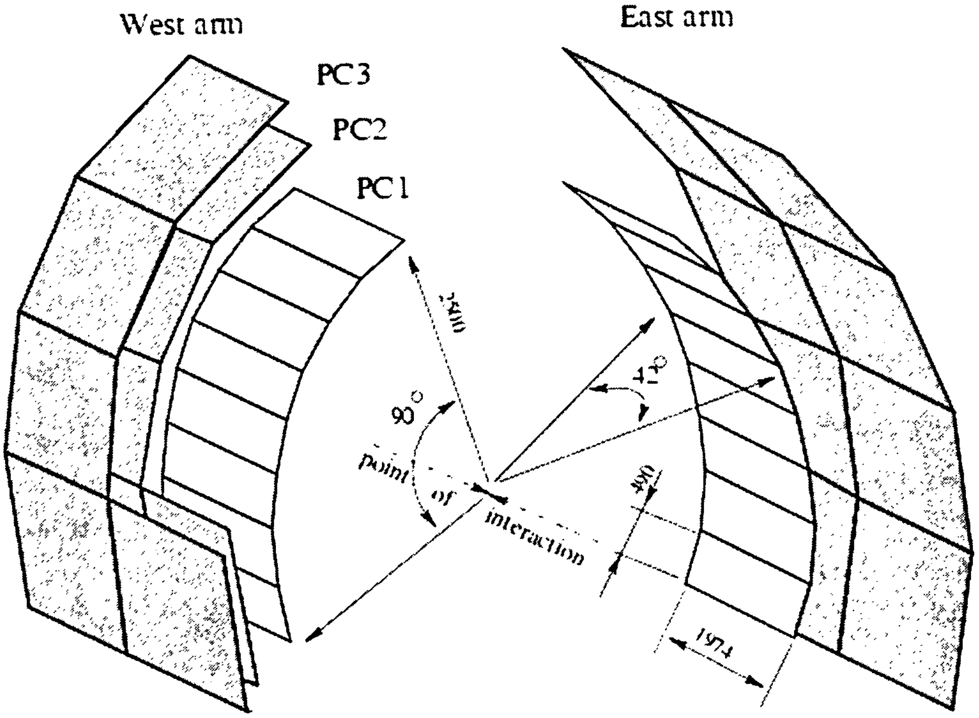

Figure 2.5: The Pad Chamber system of the PHENIX detector. There are three layers (PC1, PC2 and PC3) in the West arm and two layers (PC1 and PC3) in the East arm.

The Pad Chambers consist of three layers (PC1, PC2 and PC3) of multiwire proportional chambers with a novel pixel-readout scheme [59]. The main purpose of the PC system is to determine 3D spatial points along the particle trajectory outside the magnetic field which are used for both the determination of the longitudinal component of the momentum, p_z and the pattern recognition. Fig. 2.5 shows the radial location of the PC's in the central tracking arms. The first pad chamber layer (PC1) is located at the outer edge of the Drift Chamber at a distance of 249 cm from the beam line, the second layer (PC2) is located at a radial distance of 419 cm on the West arm only and the third layer (PC3) is at 498 cm from the interaction point. Out of the three layers, PC1 is of primary importance for the track reconstruction since it provides essential z-information of the track with a very high precision of about 1.7 mm.

Detectors for electron identification The key element in the electron identification is a Ring Imaging Čerenkov Counter (RICH) [60]. It is a large CO_2 gas volume detector with a thin mirror which reflects Čerenkov light onto an array of photo-multiplier tubes (PMT) that are situated outside of the spectrometer acceptance. The RICH is capable of identifying electrons and reject pions up to $p_T \sim 4.8$ GeV/c at the level of $\sim 10^3$ in a single track environment.

The PHENIX software reconstructs rings of Čerenkov photons and associates them with incident charged tracks. Each ring is characterized by the number of PMT hits, $n0$ or $n1$[1], by the deviation of the reconstructed ring center from the projection of the associated track onto the PMT array, *disp*, and by a ring quality factor, Q_{ring}, which shows the difference of the reconstructed ring shape from the expected one.

Further electron identification is provided by the Electromagnetic Calorimeter (EMCal) [61]. It covers the full acceptance of the central arm and measures the spatial position and energy of electrons and photons produced in the collision. The EMCal system consists of 8 large sectors, 6 Lead-Scintillator (PbSc) and two Lead-Glass modules. Electrons generate an electromagnetic shower in the EMCal and deposit almost all their energy while hadrons lose only a small fraction of their energy. Therefore by requiring the particle energy to match the measured momentum ($E/p \approx 1$) one can reduce significantly the hadronic background and extract a clean sample of electrons.

The eID criteria and pion rejection factor were studied in detailed in a single electron measurements [62–64] demonstrated the pion rejection factor at the level of $\sim 10^2$-10^4 while preserving more than 90% of electron signal.

---

[1] n0 and n1 are the number of PMTs within a ring of 3.4-8.4 cm and in a disk of 11 cm radius, respectively, around the track projection point onto the plane of PMTs.

Detectors for kaon identification The kaons are identified using the high-resolution Time-Of-Flight (TOF) wall and the EMCal (PbSc) detector. The TOF wall has a "T"-profile with 8 panels on the upper part of the "T" and 2 panels on the lower part (see Fig. 2.6). The TOF has a maximum coverage of $|\eta| < 0.35$ in pseudorapidity and $\Delta\varphi = 45°$ in azimuthal angle. It has a time resolution of $\simeq 115\ ps$ and excellent π/K separation in the momentum range $0.3 < p(GeV/c) < 2.5$. The PbSc detector has a much larger acceptance, covering the entire west arm (EMCal_{west}) and half of the east (EMCal_{east}). However, the time resolution of the PbSc is $\simeq 450\ ps$ which allows a clear π/K separation in the momentum range $0.3 < p(GeV/c) < 1$ [1]

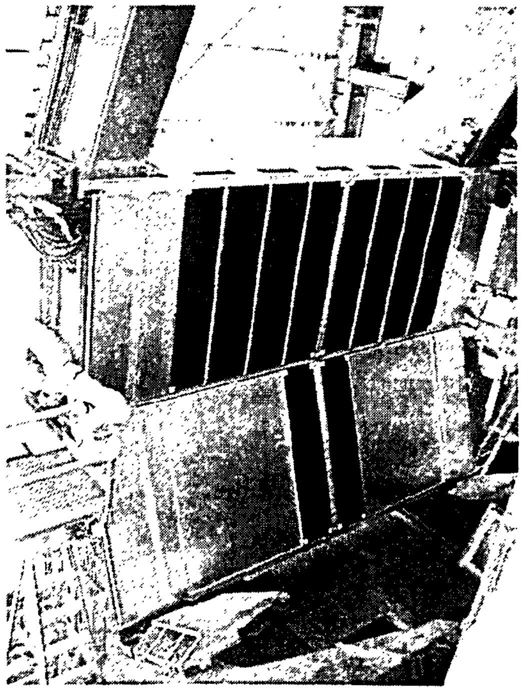

Figure 2.6: The TOF wall mounted in PHENIX.

2.3 PHENIX Data Acquisition and offline reconstruction

2.3.1 Data Acquisition

The investigation of different colliding species, ranging from polarized protons to gold ions, requires not only a versatile detector with specialized subsystems, but also a flexible data acquisition (DAQ) and a triggering system that can handle the high interaction rates of approximately 500 kHz in $p+p$ collisions and the large event sizes in high multiplicity $Au+Au$ events at a rate of a few kHz [65].

To cover the broad range of a possible QGP signatures in heavy ion collisions and to explore the regime of hard scattering at large transverse momenta it is also necessary to select and enhance rare events via specialized triggers, e.g. on highly energetic photons.

The trigger decisions within the PHENIX experiment are implemented in two levels: Level-1 triggers (LVL1) and Level-2 triggers (LVL2). The fully pipelined LVL1 triggers

---

[1] The capabilities of the TOF and EMCal detectors in π/K separation are illustrated in Fig. 3.13 and 3.14 in the next chapter.

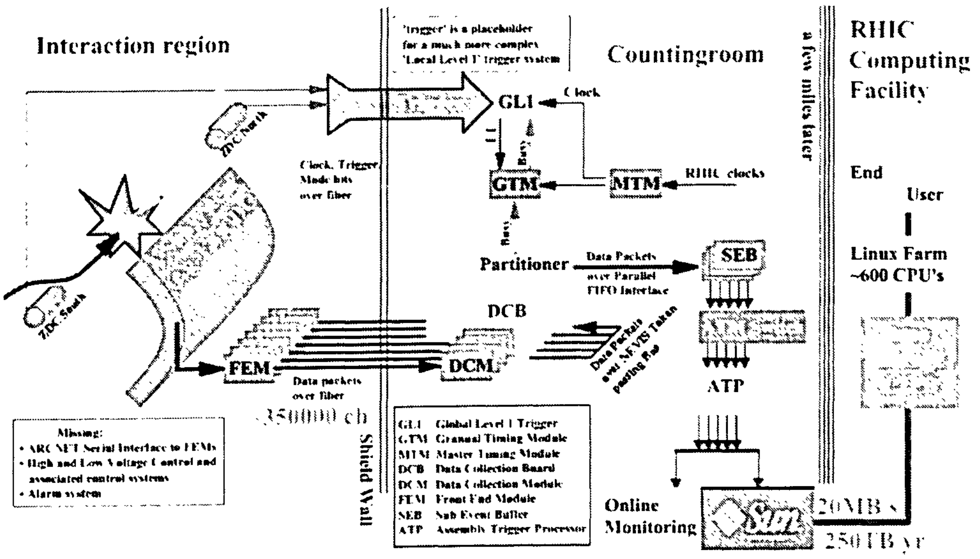

Figure 2.7: The block diagram of the PHENIX Data Acquisition system.

and the lower levels of the parallel readout are driven by the 9.43 MHz RHIC beam clock[1], while the higher levels of the readout and the LVL2 triggers are data-driven, which means that the results are propagated to the next level only after the processing of a given event is completed. The PHENIX DAQ is shown schematically in Fig. 2.7.

Signals from the various PHENIX subsystems are processed by the Front End Electronics (FEE) which digitizes the analog signals from the detector elements and buffers the data until the Level-1 (LVL1) trigger decision is made. The LVL1 trigger provides a fast filter for discarding empty beam crossings and uninteresting events before the data is fully digitized. It receives parallel input via optical fibers from different detector subsystems such as the BBC, ZDC, MuID, RICH, and EMCal. This information is converted into a bit pattern for each RHIC beam crossing and is summarized by the Global Level-1 System (GL1) which generates a raw trigger from the input trigger vectors and checks whether a trigger system or the DAQ is busy. If the raw trigger passes this test it is called a live trigger. This bit pattern is compared to a scaledown counter and only if this scaled trigger generates an accept, the GL1 initiates the readout of the Front End Modules (FEM). FEMs are located in the interaction region, near the detector. They are used to digitize the analog signal from the detectors and buffer the data waiting for the trigger

---

[1] The beam clocks provide a central time signal synchronized with the ion bunches in each of the RHIC rings (Yellow Clock and Blue Clock) and are delivered to each experiment.

decision. The trigger for an inelastic collision, the minimum bias condition, is usually given by the BBC.

Once an event is accepted the data fragments from the FEMs and primitives from the LVL1 trigger are transferred via optical fibers from the interaction region to the Data Collection Modules (DCM). The DCMs perform zero suppression, error checking and data reformatting. Many parallel data streams from the DCMs are sent to the Event Builder (EvB). The EvB performs the final stage of event assembly and provides an environment for the LVL2 trigger to operate.

The PHENIX DAQ is capable of handling the maximum $Au+Au$ collision rate of approximately 14 kHz (design capability is 25 kHz). The archiving data rate improves almost every year and is presently 400 Mbyte/s. With an average size of the minimum bias events of $\sim$ 200 kbyte it is therefore possible to archive data at a rate of about 2kHz. In order to study the rare events for which PHENIX was designed, it is necessary to further reduce the number of accepted events. This selection is carried out by the LVL2 triggers while the events are being assembled in the Assembly and Trigger Processors (ATP) in the EvB. The EvB then sends the accepted events to the PHENIX On-line Control System (ONCS) for logging and monitoring. The data is first stored in local hard disk, later on it is transferred to tapes.

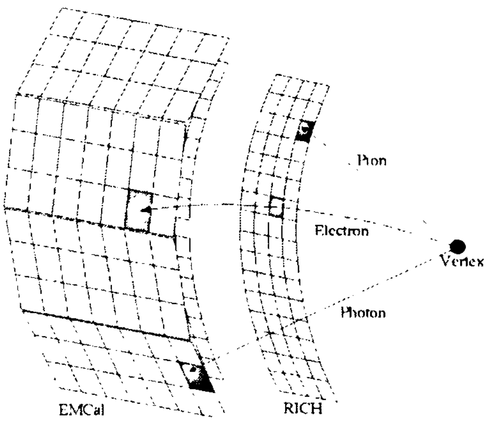

Figure 2.8: The principal scheme of the electron trigger.

LVL2 electron trigger The detectors used for electron identification, *i.e.* RICH and EMCal, can provide an electron trigger decision that allows us to increase significantly the electron detection efficiency and collect rare electron and dielectron events. The EMCal-RICH electron trigger (ERT) has been successfully implemented in PHENIX and the results obtained in $d+Au$ collisions are based on the analysis of ERT triggered events. The ERT trigger relies on the information from the EMCal and the RICH detectors. The trigger is initiated by a track with an energy above a certain threshold, E^{th}_{ERT}, in the EMCal over a 2×2 tower region called a tile. The ERT also requires a geometrical coincidence of this particular EMCal tile with the corresponding RICH tile (4×5 PMT's) determined from a look-up table which is defined on the basis of single-electron Monte Carlo simulation. The scheme of the electron trigger is illustrated in Fig. 2.8.

2.3.2 Data reconstruction

One major task of the data reconstruction is to reduce the data volume. The data is first stored in PHENIX Raw Data Format (PRDF). Basically, PRDF files contain the raw detector output such as the ADC or TDC values. In the PHENIX offline there are three general reconstruction steps. First, the raw outputs from the detector are calibrated and translated into physics quantities such as time of flight, energy deposit, etc. In general, this step is performed only once. Then one has to run reconstruction softwares to look for tracks or particles in the data. After step one and two, a new set of files is generated called *Data Summary Tapes*, "DST". The DST file is still fairly big and the data size needs to be further reduced. Hence in the third step, the DST file is filtered by trigger information for different physics topics. The filtered file contains only the track level information and only for a specific physics topics. This file is called "nanoDST". The size of the nanoDST is very small, so that it can be analyzed on a daily basis.

Chapter 3

Data analysis

3.1 Overview

The main focus of this thesis is the analysis of the ϕ meson production in $Au+Au$ and $d+Au$ collisions at center of mass energy of $\sqrt{s_{NN}}$ = 200 GeV . The analysis of the PHENIX data is performed in several stages and includes the following steps:

1. Event selection.
    - Vertex determination.
    - Event centrality.
2. Track selection and particle identification.
    - Track quality assurance.
    - Particle identification.
3. Pair analysis.
    - Invariant mass spectra and combinatorial background.
    - Signal extraction.
4. Monte Carlo simulation to correct the data for acceptance effects, reconstruction efficiency and multiplicity effects.

The data sets corresponding to the two different field polarities in Run 4, $++$ and $--$ (see Section 2.2.1), and to the two different ERT thresholds in Run 3, E^{th}_{ERT} = 600 and 800 MeV (see Section 2.3.1), were analyzed separately. The final results were obtained by combining the two contributions using a weighted average procedure.

3.2 Event selection and Centrality

3.2.1 Vertex determination

The collision vertex is determined by the BBC's on an event-by-event basis using the expression Eq. 2.1. The BBC vertex distribution in $d+Au$ and $Au+Au$ collisions are shown in the left and right panels of Fig. 3.1, respectively. For the $Au+Au$ case the vertex distribution has an offline vertex cut of ± 30 cm applied at the data production level, see Section 2.3.2

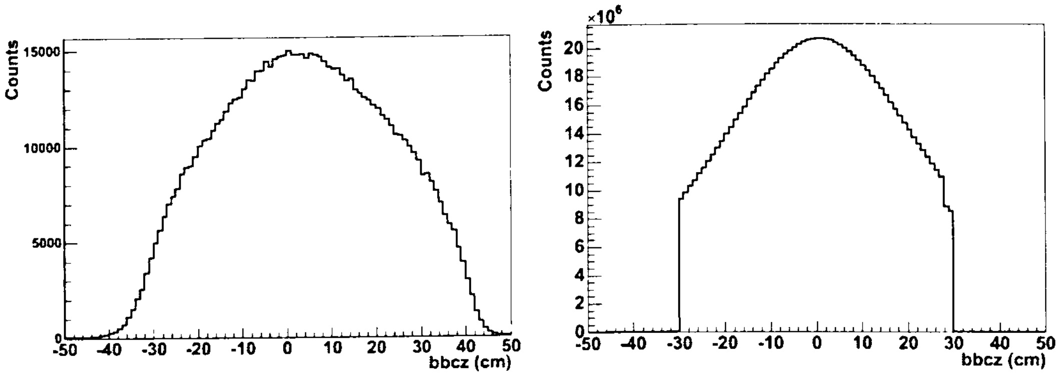

Figure 3.1: The z_{vtx} distribution in $d+Au$ (left panel) and $Au+Au$ (right panel) collisions.

In the PHENIX geometry particles originating from collisions which are far from the center of the detector ($z_{vtx} = 0$ cm) have a higher probability to interact with the material of the central magnet and create an additional conversion electron background. The average number of electrons per event as a function of the vertex position in $d+Au$ and $Au+Au$ collisions are shown on the left and right panels of Fig. 3.2, respectively. In both cases one can clearly see the electron background from conversions in the magnet poles. In order to minimize this background, the $Au+Au$ analysis of $\phi \to e^+e^-$ is restricted to events that have the collision vertex in the range -28 cm $< z_{vtx} <$ 26 cm. The asymmetry seen in the right panel of Fig. 3.2 is due to the different electron identification criteria used for the different RICH sectors as discussed in Section 3.4.2. The $\phi \to K^+K^-$ analysis does not suffer from conversions and was performed with a looser cut $|z_{vtx}| < 30$ cm. In the $d+Au$ analysis a loose vertex cut $|z_{vtx}| < 30$ cm was used to preserve the maximum available statistics.

The total number of analyzed events after applying the vertex cuts are quoted in the Table 3.1.

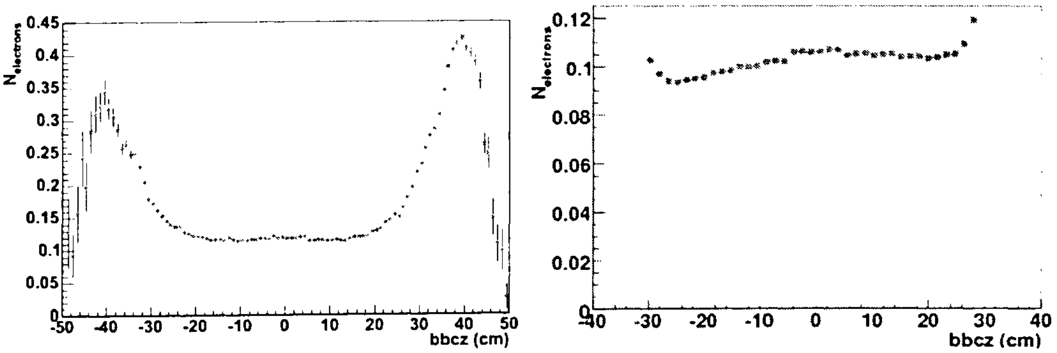

Figure 3.2: Number of electrons per event *vs.* z_{vtx} in the $d+Au$ (left panel) and $Au+Au$ (right panel) collisions.

Table 3.1: Sample sizes used in the $\phi \rightarrow e^+e^-$ and $\phi \rightarrow K^+K^-$ analyses. * and † denote the samples which are analyzed using TOF only and both TOF and EMCal, respectively.

	$d+Au$, Run 3.		$Au+Au$, Run 4.			
analysis	$\phi \rightarrow e^+e^-$		$\phi \rightarrow e^+e^-$		$\phi \rightarrow K^+K^-$	
vertex cut (cm)	$\lvert z_{vtx}\rvert < 30$		$-28 < \lvert z_{vtx}\rvert < 26$		$\lvert z_{vtx}\rvert < 30$	
trigger	ERT		MB		MB	
	600 MeV	800 MeV	++ field	−− field	++ field	−− field
N_{events} (10^6)	34	14	395	631	$183^\star$ ($84^\dagger$)	$226^\star$ ($86^\dagger$)

3.2.2 Minimum Bias trigger

The $Au+Au$ data are recorded with a Minimum Bias (MB) trigger. The MB trigger aims at maximizing the range of impact parameters collected in inelastic interactions. It utilizes the information from the BBC and ZDC with the following requirements:

- At least two PMT are fired in both BBC_{North} and BBC_{South} simultaneously with the collision vertex restricted to the on-line cut of $|z_{vert}| < 38$ cm.
- ZDC_{North} and ZDC_{South} measure at least one neutron, each.

The efficiency of the MB trigger for the above conditions has been determined in a detailed simulation of the BBC and ZDC response in $Au+Au$ collisions simulated with the HIJING event generator [66] and found to be $\varepsilon_{MB} = 92.2^{+2.5}_{-3.0}\%$ [67] of the total inelastic cross section of 7.2 *barn*. The study indicates that the trigger inefficiency is localized in the most peripheral events.

The $d+Au$ analysis data were recorded with an electron trigger (see Section 2.3.1) and its efficiency will be discussed in Section 3.3.

3.2.3 Event centrality

The event centrality is related to the collision geometry and reflects the impact parameter or the amount of overlap between the two colliding nuclei. The number of charged particles measured by the BBC and the number of spectator neutrons measured by the ZDC can provide an independent centrality definition since both are sensitive to the impact parameter of the collision. In PHENIX, the centrality is determined by the correlation between the charge fraction measured by the BBC and the energy fraction deposited in the ZDC using the so-called *clock*-method as shown in Fig. 3.3. In this method the angular position of an event, φ_{cent}, in the BBC charge *vs.* ZDC energy space is calculated as:

$$\varphi_{cent} = \arctan\left(\frac{(Q_{tot} - Q_0)/Q_{max}}{E_{tot}/E_{max}}\right) \tag{3.1}$$

where Q_{tot} and E_{tot} are the total charge measured by both (North and South) BBC's and the total energy deposited in both (North and South) ZDC's, respectively, Q_{max} and E_{max} are the maximum charge and energy, respectively. Q_0 defines the BBC charge value from which the angle φ_{cent} is determined. The choice of Q_0 is a parameter and PHENIX adopted the value of Q_0 = 0.2 × Q_{max}, corresponding to the maximum of the E_{tot} distribution. The choice of the parameter has little effect on the centrality definition. For example taking Q_0 = 0.5 Q_{max} as another clock origin, the number of participants, N_{part}, varies by less than 1% in central collisions and by approximately 10% in very peripheral collisions. It should be noted that the choice of Q_0 is not the dominant source of uncertainty in the determination of N_{part} (seeTable 3.2). The full φ_{cent} range corresponds to the full centrality range covered by the minimum bias trigger. Dividing φ_{cent} into a certain number of bins, each one with the same number of entries, and the centrality range into the same number of bins one obtains a mapping between φ_{cent} and the centrality range in percentage.

The $\phi \rightarrow K^+K^-$ analysis in $Au+Au$ collisions was performed for the entire MB sample and seven centrality bins: 0-10%, 10-20%, 20-30%, 30-40%, 40-50%, 50-60% and 60-90%. In the $\phi \rightarrow e^+e^-$ analysis we used MB for $d+Au$ collisions and MB, 0-20%, 20-40% and 40-92% centrality bins for the $Au+Au$ collisions.

3.2.4 Number of participants and number of collisions

As another measure of the multiplicity PHENIX uses the number of nucleon-nucleon collisions, N_{coll}, and the number of nucleons participating in the collision, N_{part}. In high energy nuclear physics N_{part} and N_{coll} are considered to be relevant physical quantities

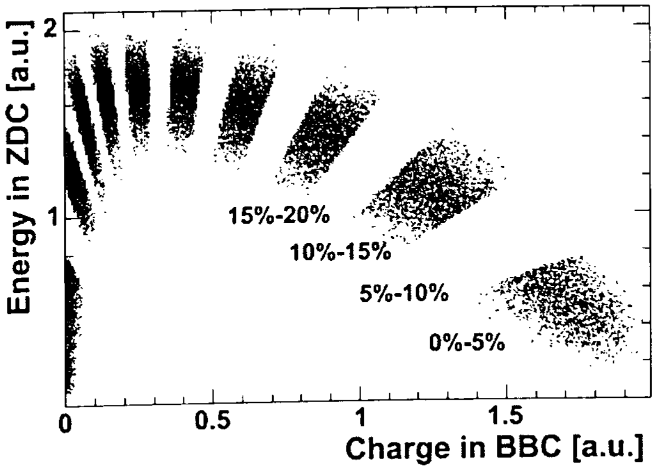

Figure 3.3: Event centrality selections using the ZDC energy and BBC charge.

rather than of impact parameter. The event multiplicity scales with the number of participants, N_{part}, which reflects the particle production behavior for the low momentum transfer (*soft*) processes. At higher energies one expects an increase of the particle production from *hard* processes which will result in the fact, that the multiplicity of produced particles is proportional to the number of elementary nucleon-nucleon collisions, N_{coll}. The N_{part} and N_{coll} distributions in $Au+Au$ collisions are determined using a Monte Carlo simulation based on the Glauber model [68] with a Woods-Saxon nuclear density profile:

$$\rho(r) = \frac{1}{1+e^{\frac{r-r_n}{d}}}, \tag{3.2}$$

where r_n is the nuclear radius and d is the diffuseness parameter. For the gold nucleus r_n and d are taken to be 6.38 fm and 0.54 fm, respectively [69].

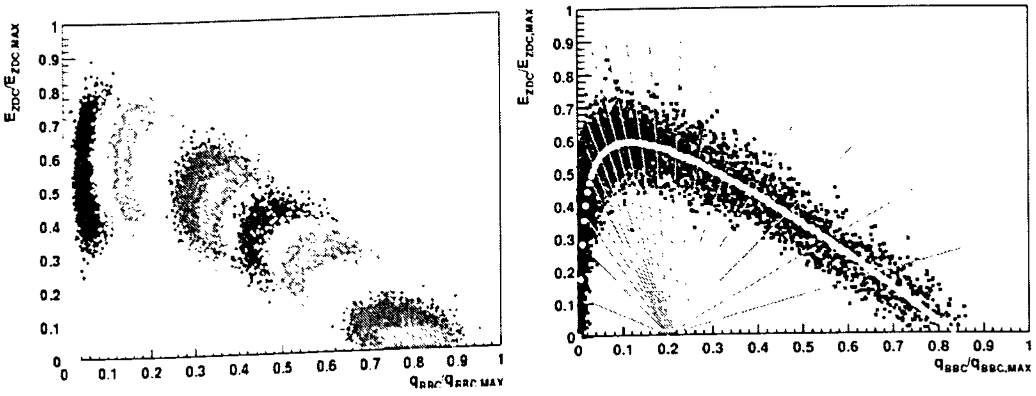

Figure 3.4: The ZDC *vs.* BBC for different number of participants (left panel). The *clock*-method to define centrality classes in the simulation (right panel).

The Glauber model assumes that nucleon trajectories stay constant during the collision, independently of how many other nucleons it interacts with and a collision occurs if the relative distance between two nucleons is less than $\sqrt{\sigma_{nn}/\pi}$, where σ_{nn} =42 mb is the nucleon-nucleon cross-section at 200 GeV. With these parameters one can simulate the response of the BBC and ZDC in the collision of two *Au* nuclei at different impact parameters. The left panel of Fig. 3.4 shows the correlation between simulated signals in the BBC and ZDC detectors for different number of participants in steps of 25. The *i*-th blob corresponds to 25 (i - 1) $\leq N_{part} \leq$ 25 i. Then the centrality classes are determined using the same *clock*-method discussed above and for each centrality the corresponding value of N_{part} is determined. This is illustrated in the right panel of Fig. 3.4. N_{coll} is calculated using a similar procedure, but counting the number of collisions instead of the number of participants.

The dependence of N_{part} and N_{coll} on centrality is shown in Fig. 3.5 and the average values of N_{part} and N_{coll} corresponding to the centralities used in the $Au+Au$ analysis are quoted in Table 3.2.

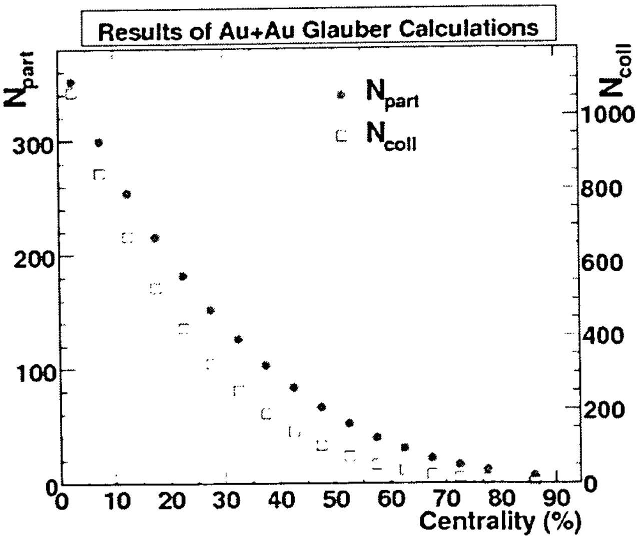

Figure 3.5: N_{part} and N_{coll} *vs.* centrality calculated for $Au+Au$ collisions.

In $d+Au$ collisions, a minimum bias event corresponds to 9.1 ± 0.4 participating nucleons and to 8.3 ± 0.5 nucleon-nucleon collisions.

3.3 Single electron ERT efficiency

The ERT trigger efficiency as a function of momentum is calculated for each EMCal sector from the full trigger emulator developed in the framework of the PHENIX software.

Table 3.2: The centrality classes and the corresponding average numbers of nucleon-nucleon collisions and participants as used in the $Au + Au$ analysis.

Centrality %	N_{part}	N_{coll}
MB	109.1 ± 4.1	257.8 ± 25.4
0-10	325.2 ± 3.3	955.4 ± 93.6
10-20	234.6 ± 4.7	602.6 ± 59.3
20-30	166.6 ± 5.4	373.8 ± 39.6
30-40	114.2 ± 4.4	219.8 ± 22.6
40-50	74.4 ± 3.8	120.3 ± 13.7
50-60	45.5 ± 3.3	61.0 ± 9.9
60-90	14.5 ± 2.5	14.5 ± 4.0
0-20	279.9 ± 4.0	779.0 ± 76.5
20-40	140.4 ± 4.9	296.8 ± 31.1
40-92	31.9 ± 3.0	45.0 ± 7.1

The trigger efficiency can be also determined from the ratio of the measured single electron p_T spectrum from ERT events to the measured p_T spectrum of single electrons from MB events. MB and ERT p_T spectra of electrons for the W0 EMCal sector are shown on the left panel of Fig. 3.6. The absolute yields of the ERT spectrum is shown by red points and the MB spectrum scaled by the scale-down factor of the MB trigger is shown by blue points. The single electron efficiency for the W0 EMCal sector extracted from the data is shown on the right panel of Fig. 3.6 (blue points) along with the ERT efficiency derived from the emulator (red points). For all EMCal sectors the two methods are in agreement for $p_T \lesssim 2$ GeV/c. However, since the statistics in the MB data sample is limited for $p_T > 2$ GeV/c the electron trigger efficiencies extracted from the emulator are used.

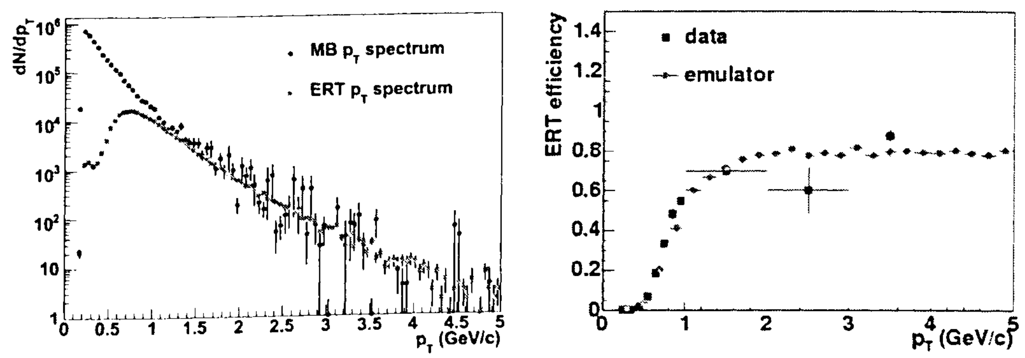

Figure 3.6: MB (blue) and ERT (red) single electron p_T spectra (left panel) and ERT efficiencies extracted from the data (blue) and trigger emulator (red) (right panel).

3.4 Track selection and particle identification

3.4.1 Track quality

The track reconstruction algorithm associates hits collected in the DC (X1 or X2, or both) to the hit information from PC1 and the collision vertex, z_{vtx}, determined by BBC. The reconstruction accuracy depends on the number of hits measured in the DC, whether the PC1 hit associated to the track is unique or ambiguous and whether the additional information from the UV plane was or not used for the reconstruction. Therefore, to each reconstructed track a specific value Q_{track} is assigned that indicates the quality of the track.

The quality of the reconstructed track is recorded using the following binary pattern:

$$Q_{track} = A \times 2^0 + B \times 2^1 + C \times 2^2 + D \times 2^3 + E \times 2^4 + F \times 2^5 \tag{3.3}$$

where A, B, C, D, E and F are quality bits defined as follows:

- $A = 1$ if X1 plane is used.
- $B = 1$ if X2 plane is used.
- $C = 1$ if there are hits in UV plane.
- $D = 1$ if there are hits in UV plane and their choice is unique.
- $E = 1$ if there are hits in PC1.
- $F = 1$ if there are hits in PC1 and their choice is unique

otherwise the bits are set to 0. As mentioned above the track can be reconstructed only if at least one DC plane (X1 or X2) is used which means that bits A and B can not have a zero value simultaneously. The track quality values derived from the bit pattern are summarized in Table 3.3.

The quality distributions of the reconstructed tracks measured in Run 3 and Run 4 are shown in the left and right panels of Fig. 3.7, respectively. In both cases one can clearly distinguish four classes of tracks. The tracks that produce hits both in X1 and X2, have unique UV hits and unique (Q_{track} = 63) or ambiguous (Q_{track} = 31) hit in PC1 are considered to be the best.

In the $Au+Au$ analyses both in $\phi \rightarrow e^+e^-$ and $\phi \rightarrow K^+K^-$ we used tracks with the best qualities, 31 and 63, while in the $d+Au$ analysis we used tracks with all quality classes to preserve the maximum available statistics.

Table 3.3: Summary of the DC track quality.

Comment	A	B	C	D	E	F	Quality, Q_{track}
$\mathrm{PC1}^{found}_{unique}$ & $\mathrm{UV}^{found}_{unique}$	1	0	1	1	1	1	61
	0	1	1	1	1	1	62
	1	1	1	1	1	1	63
$\mathrm{PC1}^{found}_{unique}$ & no UV	1	0	0	0	1	1	49
	0	1	0	0	1	1	50
	0	1	0	0	1	1	51
$\mathrm{PC1}^{found}_{ambiguous}$ & $\mathrm{UV}^{found}_{unique}$	1	0	1	1	1	0	29
	0	1	1	1	1	0	30
	0	1	1	1	1	0	31
$\mathrm{PC1}^{found}_{ambiguous}$ & UV^{found}	1	0	1	0	1	0	21
	0	1	1	0	1	0	22
	0	1	1	0	1	0	23
$\mathrm{PC1}^{found}_{ambiguous}$ & no UV	1	0	0	0	1	0	17
	0	1	0	0	1	0	18
	0	1	0	0	1	0	19

3.4.2 Particle identification

Electron identification cuts PHENIX identifies electrons using the information from the RICH and EMCal, see Section 2.2.1.

The primarily electron identification is provided by the RICH detector. Each reconstructed ring is characterized by the number of PMT hits within a ring ($n0$) or inside a disc ($n1$), by the deviation of the reconstructed ring center from the projection of the associated track ($disp$) and by difference of the reconstructed ring shape from the expected one (Q_{ring}) (see Section 2.2.3).

For the Run 3 $d+Au$ analysis we used $n0 \geq 1$. In Run 4 a misalignment in the east-south (ES) RICH sector resulted in a distortion of the ring shape and, consequently, in a lower distribution of the $n0$ variable in this sector. The distributions of the $n0$ variable in the different RICH sectors are shown on the left panel of Fig. 3.8. One can clearly see the distortion of the $n0$ distribution in the ES RICH sector.

Since $n1$ represents the number of fired PMTs inside the disc and not the ring as $n0$ it is less sensitive to a distortion of the ring shape. Indeed, the $n1$ distributions in the different RICH sectors shown on the right panel of Fig. 3.8 are very similar. The identification of the electrons in the $Au+Au$ analysis are therefore done requiring $n1$ >2 for the ES RICH sector and $n0$ >2 for all the other sectors. This choice of the identification cuts is

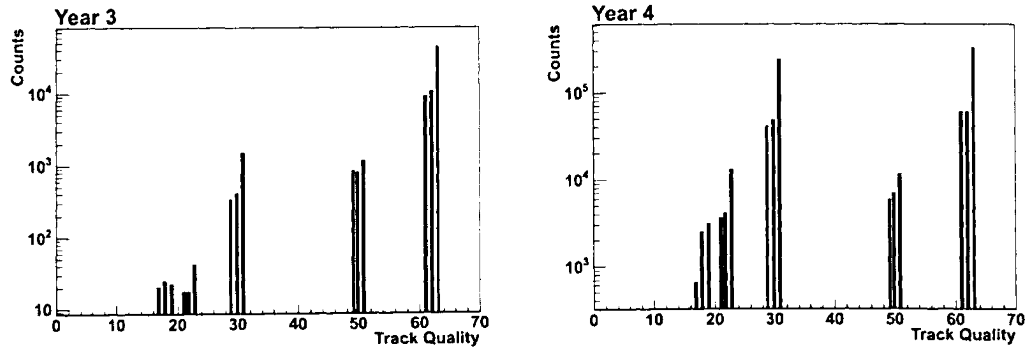

Figure 3.7: Track quality distributions in Run 3 (left panel) and Run 4 (right panel).

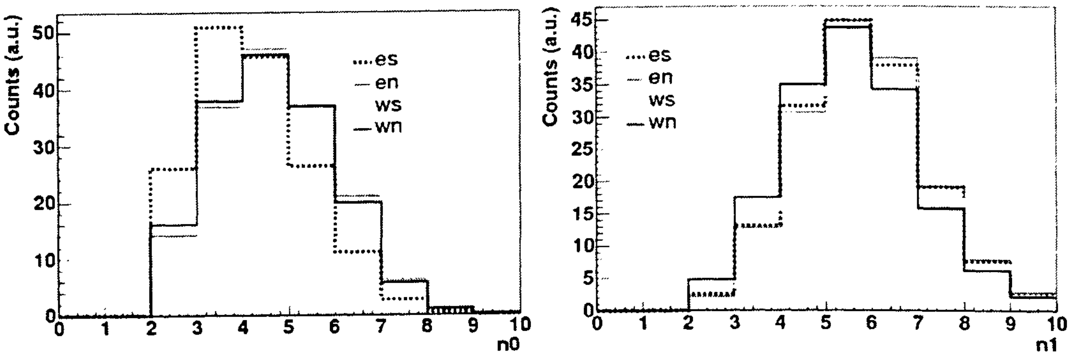

Figure 3.8: The distributions of the $n0$ (left panel) and $n1$ (right panel) variables in the different RICH sectors shown by different colors. The distributions have been normalized to represent the same total area.

responsible for the asymmetry seen in the Fig. 3.1.

In addition to that, the distance between the projection of the associated track onto the array of PMT's and the center of the reconstructed ring is required to be less than 5 cm in both analyses, $disp < 5$ cm. Also the quality of the ring shape, Q_{ring}, must be less than 10 and 15 cm in $Au+Au$ and $d+Au$ analyses, respectively. The requirement on Q_{ring} in $d+Au$ analysis is looser to preserve maximum statistics. The distributions of the $disp$ and Q_{ring} variables in the $Au+Au$ data are shown in Fig. 3.9.

Further electron identification utilizes the information provided by the EMCal. It requires the energy, E, measured by the EMCal cluster matched to the electron track to be equal to the track momentum, p: $E/p \approx 1$. Both, the spatial track matching to the EMCal and the E/p ratio depend on the momentum, EMCal sector and particle charge. Examples of the track matching distributions to the EMCal along the z-, and φ-coordinates and of the E/p distribution for one EMCal sector in the momentum bin 0.6-0.8 GeV/c are shown

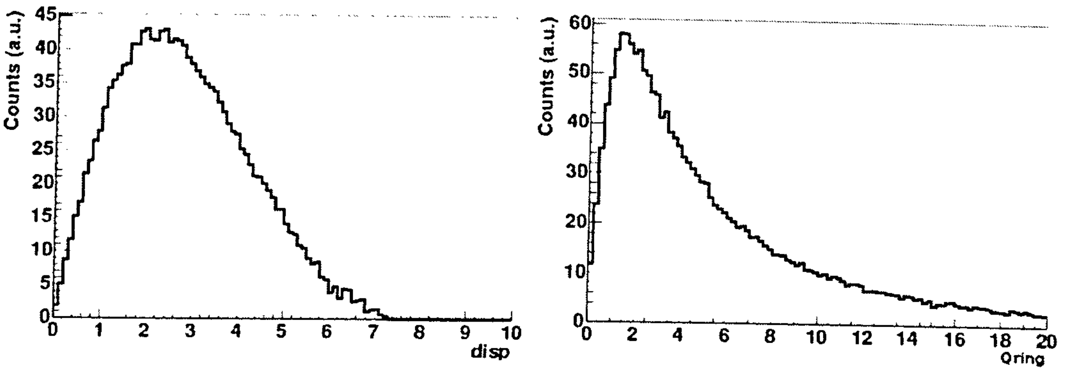

Figure 3.9: The distributions of the *disp* (left panel) and Q_{ring} (right panel) variables.

in Fig. 3.10. The φ distribution has two peaks corresponding to electrons and positrons which are separated by the magnetic field. The pion contamination of the electron sample causes an asymmetry on the left shoulder of the E/p distribution.

PHENIX uses an algorithm that translates E/p and the spatial matching in the z and φ directions into reduced variables dep and $\sigma^{z,\varphi}_{EMC}$ which are centered at zero and have a sigma equal to one. The reduced variables provide a convenient way to apply cuts in units of sigmas. To derive them the raw distributions of the track matching and the $E/p-1$ distributions are fitted with a Gaussian function for each EMCal sector and momentum bin. The procedure is done separately for electrons and positrons selected with strong eID cuts ($n0$ >3, dep <4 and $Q_{ring} < 7$) to get a clean sample. The results of the fits are shown by the color lines in Fig. 3.10. The $E/p-1$ distribution is fitted with a Gaussian function (red solid line) and an exponential function (black dashed line) to account for the residual pion background.

The reduced variables are calculated using the centroid and sigma derived form the fit as:

$$\sigma^{z}_{EMC} = \frac{\Delta z_{measured} - \Delta z_{gauss}}{\sigma^{z}_{gauss}}, \quad \sigma^{\varphi}_{EMC} = \frac{\Delta\varphi_{measured} - \Delta\varphi_{gauss}}{\sigma^{\varphi}_{gauss}},$$
$$dep = \frac{(E/p-1)_{measured} - (E/p-1)_{gauss}}{\sigma^{E/p-1}_{gauss}} \quad (3.4)$$

where Δz_{gauss}, $\Delta\varphi_{gauss}$ and $(E/p-1)_{gauss}$ are the centroids of the fit and σ^{z}_{gauss}, σ^{φ}_{gauss} and $\sigma^{E/p-1}_{gauss}$ are the corresponding widths.

An example of reduced mean values and sigmas for the track matching to the EMCal along the z-, φ-coordinates and for the dep variable as a function of p_T are shown

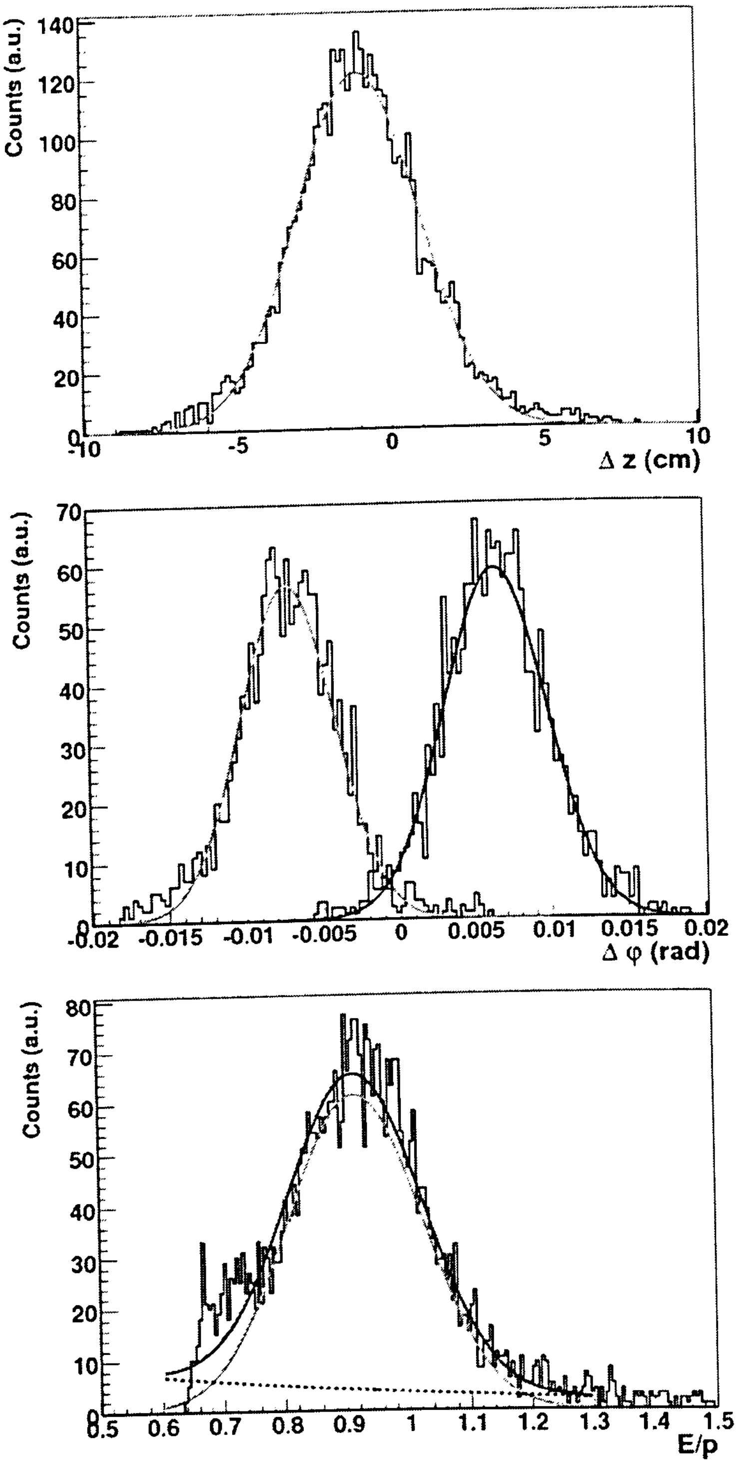

Figure 3.10: Track matching along the z- (top panel), φ- (middle panel) coordinates and E/p distribution (bottom panel) in one EMCal sector of the East arm in the momentum bin 0.6-0.8 GeV/c . Color lines represent the fit with a Gaussian function used to calculate reduced variables.

in Fig. 3.11 and Fig. 3.12 for the $d+Au$ and $Au+Au$ collisions, respectively.

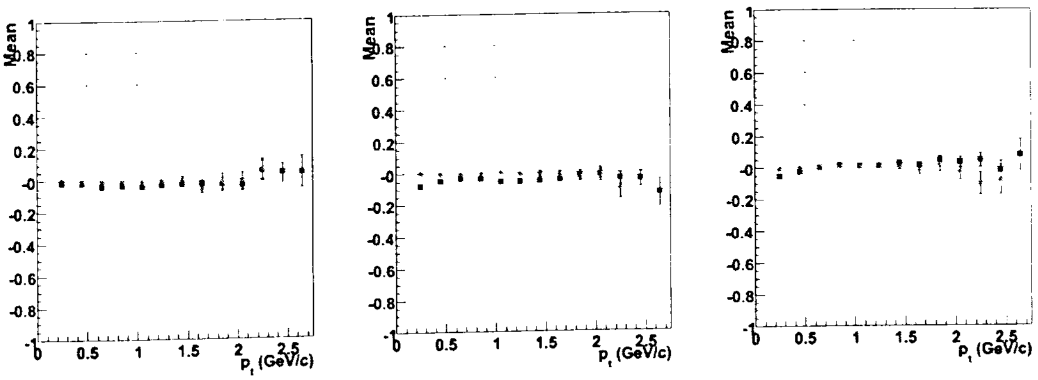

(a) σ^{z}_{EMC}-mean (b) σ^{φ}_{EMC}-mean (c) dep-mean

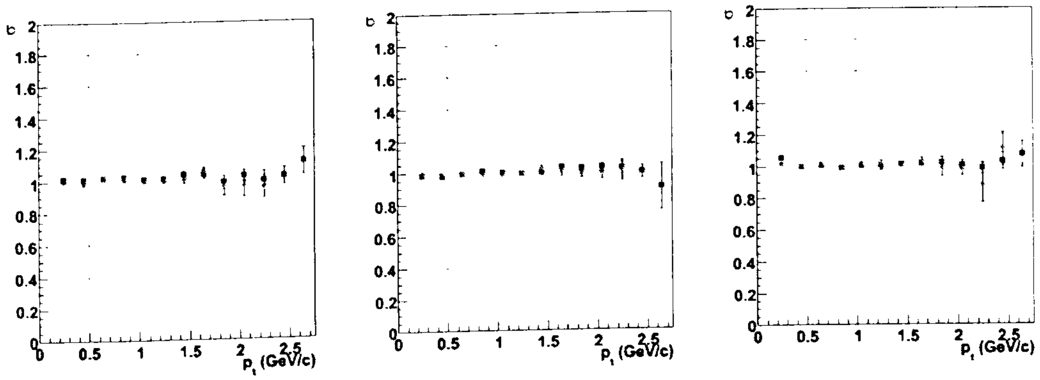

(d) σ^{z}_{EMC}-sigma (e) σ^{φ}_{EMC}-sigma (f) dep-sigma

Figure 3.11: Mean and sigma values of the track matching along the z- and φ-coordinates and for the dep variable in one EMcal sector of the East arm as a function of p_T in $d+Au$ collisions. Blue and red points represent electrons and positrons, respectively.

In both the $Au+Au$ and $d+Au$ analyses reconstructed tracks are required to have 3σ matching to the associated EMCal cluster. The combined energy-momentum cut was set to $dep >$ -2 and $|dep| < 3$ in $Au+Au$ and $d+Au$ runs, respectively.

Kaon identification cuts As mentioned above, the PHENIX central arm spectrometer utilizes the TOF wall and PbSc modules for kaon identification. The kaons are identified from the mass-squared distribution of all tracks passing through the detector using the momentum, p, and time-of-flight measurements:

$$m^2 = p \cdot \left(\frac{t_{TOF} \cdot c}{L} - 1\right) \tag{3.5}$$

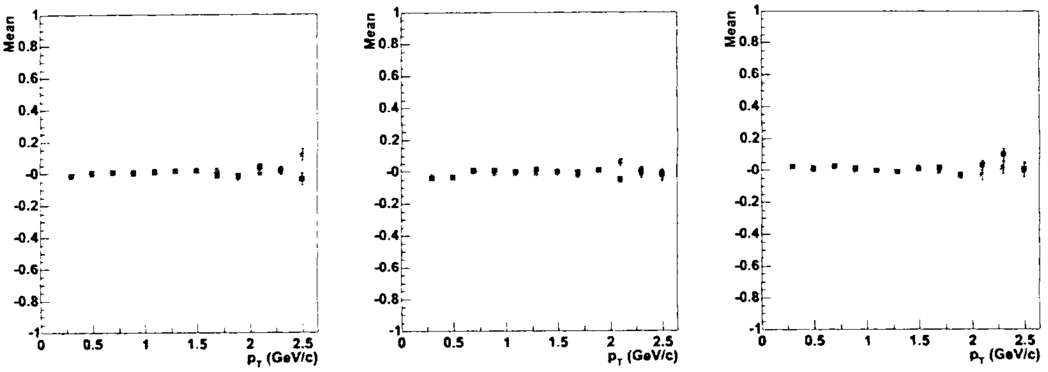

(a) σ^{z}_{EMC}-mean (b) σ^{φ}_{EMC}-mean (c) *dep*-mean

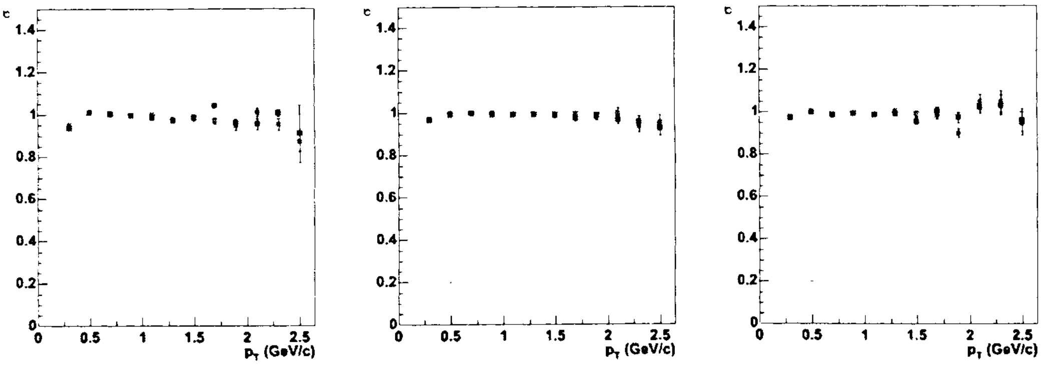

(d) σ^{z}_{EMC}-sigma (e) σ^{φ}_{EMC}-sigma (f) *dep*-sigma

Figure 3.12: Mean and sigma values of the track matching along the z- and φ-coordinates and for the dep variable in one EMcal sector of the East arm as a function of p_T in $Au+Au$ collisions. Blue and red points represent electrons and positrons, respectively.

where the t_{TOF} is the time of flight measured by the detector, c is the speed of light and L is the path-length to the detector.

The pid capability of the TOF and EMCal and the corresponding m^2 distributions are shown in Fig. 3.13 and Fig. 3.14, respectively.

The m^2 and track matching distributions are also translated into momentum dependent reduced variables isK, σ_{TOF} and σ_{EMC}. isK is a variable which defines the number of sigmas by which the m^2 of the reconstructed track deviates from the value given by a real kaon.

The final analysis is performed with $|isK| < 2$ and 3σ track matching for both TOF and EMCal detectors.

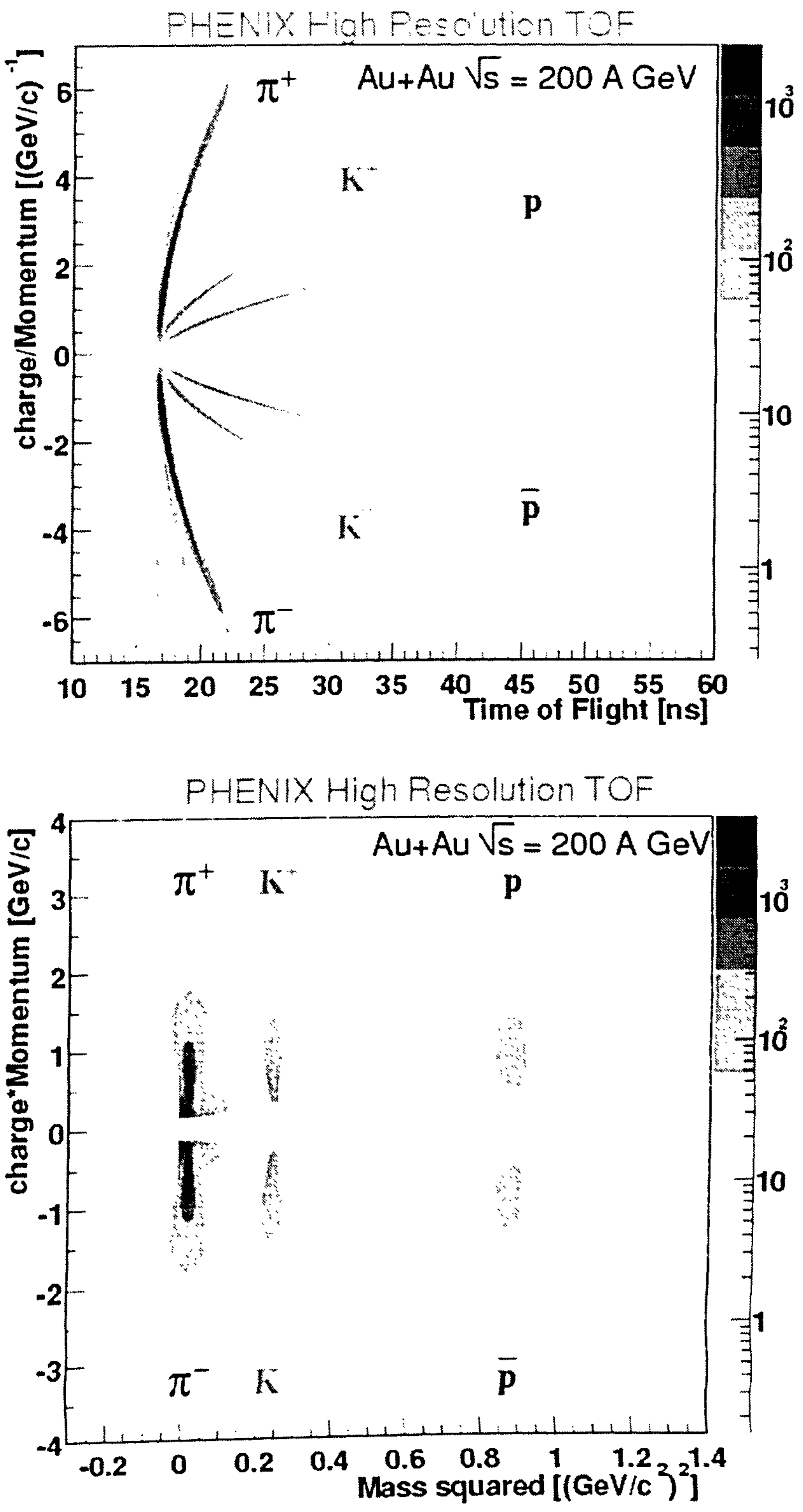

Figure 3.13: Charge/momentum *vs.* t_{TOF} (top panel) and *vs.* m^2 (bottom panel) measured by the TOF.

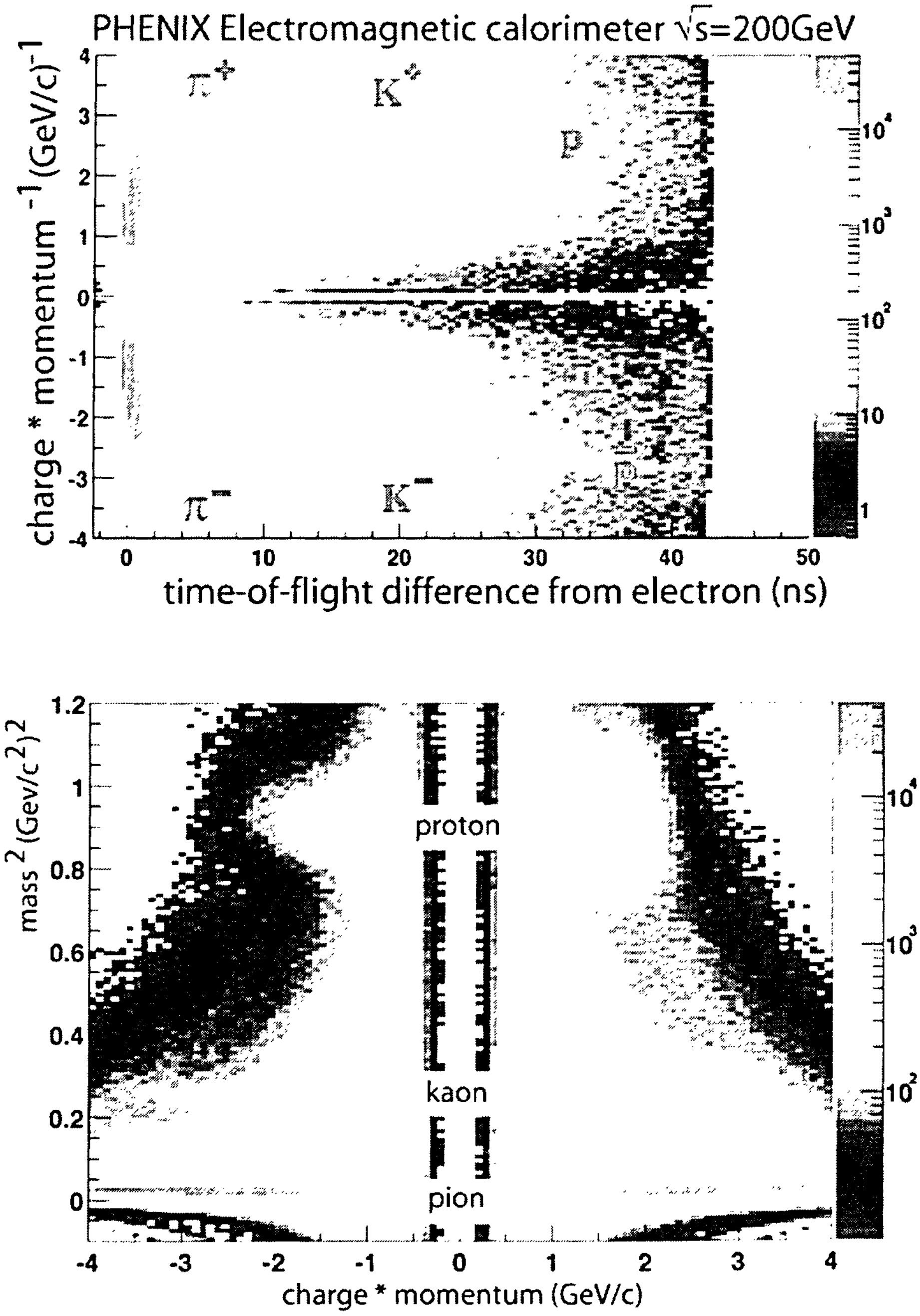

Figure 3.14: Charge/momentum *vs.* t_{EMCal} (top panel) and *vs.* m^2 (bottom panel) measured by the EMCal.

3.4.3 Summary of selection cuts

Table 3.4 summarizes the selection cuts used to extract clean samples of electrons and kaons.

Table 3.4: Summary of selection cut used in the $\phi \rightarrow e^+e^-$ and $\phi \rightarrow K^+K^-$ analyses. For the definition of the variables see text above.

	$d+Au$, Run 3	$Au+Au$, Run 4	
analysis	$\phi \rightarrow e^+e^-$	$\phi \rightarrow e^+e^-$	$\phi \rightarrow K^+K^-$
vertex cut (cm)	$\lvert z_{vtx}\rvert < 30$	-28 < $\lvert z_{vtx}\rvert < 26$	$\lvert z_{vtx}\rvert < 30$
track quality, Q_{track}	all	best (63 or 31)	best (63 or 31)
matching to	RICH: $disp < 5$ cm EMCal: $\sigma_{EMC} < 3$	RICH: $disp < 5$ cm EMCal: $\sigma_{EMC} < 3$	TOF: $\sigma_{TOF} < 3$ EMCal: $\sigma_{EMC} < 3$
particle ID	$n0 > 1$ $Q_{ring} < 15$ $\lvert dep\rvert < 3$	$n0_{EN,WS,WN} > 2$, $n1_{ES} > 2$ $Q_{ring} < 10$ $dep >$ -2	$\lvert isK\rvert_{TOF} < 2$ $\lvert isK\rvert_{EMC} < 2$

3.4.4 Rejection of artificial tracks

If two or more tracks hit the same wire plane in the Drift Chamber one of the tracks can get reconstructed multiple times. This phenomenon is called "DC ghosts" and can be handled since these tracks have nearly every parameter in common.

The RICH optics has an almost spherical geometry and parallel tracks produce Čerenkov light which gets reflected onto the same photo-multipliers. The RICH information, *i.e* $n0$, $disp$ and Q_{ring}, of a real electron could be assigned to a random hadron which is parallel to the electron and the hadron will be miss-identified as electron.

The "DC ghosts" and RICH ring sharing phenomena produce artificial pairs which must be rejected. Fig. 3.15 shows an example of the Δz vs. $\Delta\varphi$ distributions for electron pairs in the DC and in the RICH detectors in the $Au+Au$ data. The DC ghosts and RICH ring sharing are clearly seen. They are treated as follows:

- if for any two tracks 1 and 2, $|DC_z^1 - DC_z^2| < R_{DC}$ and $|DC_\varphi^1 - DC_\varphi^2| < \varphi_{DC}$ the one having worst eID is rejected. In the $\phi \rightarrow K^+K^-$ analysis one of the two tracks is removed randomly and the other one is kept.
- if for any two tracks 1 and 2, $|RICH_z^1 - RICH_z^2| < R_{RICH}$ and $|RICH_\varphi^1 - RICH_\varphi^2| < \varphi_{RICH}$ the one having worst eID is rejected.

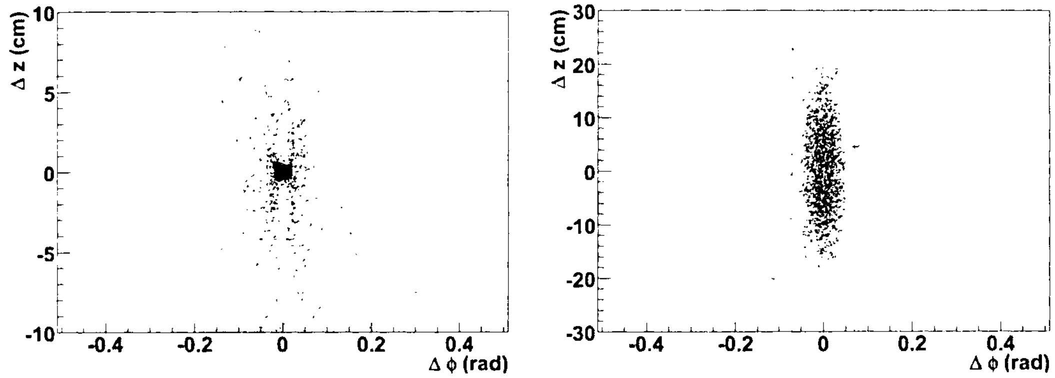

(a) DC ghosts (b) RICH ring sharing

Figure 3.15: Δz *vs.* $\Delta\varphi$ for pairs of tracks in the DC and RICH detectors. The red lines represent the cuts applied to identify ghost tracks in the DC and ring sharing in the RICH detector.

The values of R_{DC}, φ_{DC}, R_{RICH} and φ_{RICH} are listed in Table 3.5.

Table 3.5: The cut values used to reject DC ghosts and RICH ring sharing.

Project	$\phi \rightarrow e^+e^-$		$\phi \rightarrow K^+K^-$
	$d+Au$	$Au+Au$	$Au+Au$
R_{DC} (cm)	1	1	0.2
φ_{DC} (rad)	0.05	0.05	0.03
R_{RICH} (cm)	20	30	-
φ_{RICH} (rad)	0.07	0.07	-

The fraction of events which contain all artificial tracks (DC ghosts and RICH ring sharing) in $Au+Au$ minimum bias events and three centrality bins used in $\phi \rightarrow e^+e^-$ analysis are listed in Table 3.6. As expected the fraction increases with centrality and reaches a non negligible amount for central collisions. Although the artificial pairs contribute mainly to the mass region below 600 MeV/c^2 their affect on the ϕ analysis is taken into account in the evaluation of the correction function, see Section 3.8.

Table 3.6: Fraction of events containing artificial tracks (DC ghosts and RICH ring sharing) in $Au+Au$ $\phi \rightarrow e^+e^-$ analysis.

Centrality %	MB (0-92.2)	0 - 20	20 - 40	40 - 92
Fraction (%)	10	29	13	3

In the low multiplicity environment of the $d+Au$ events artificial tracks occur in less than 1% of events.

If there is more than one track sharing the same hit in a TOF slat or a EMCal tower the time and energy information of these tracks get corrupted. This results in a spurious, so-called "intruder" mass peak at $\sim$ 1.06 GeV/c^2 in the invariant mass spectrum measured in the TOF-TOF or EMCal-EMCal detector combinations. The "intruder" mass peak can be explained assuming that one of these tracks is a kaon. The second track has the same timing information. If the momentum of the second track is similar to the momentum of the first one it will have similar mass and therefore will be assigned as a kaon. In this case the invariant mass of the "intruder" peak calculated in the rest frame of the pair is $m_{int}^2 = 4 * ((m_{kaon})^2 + (p_{CM})^2)$, where m_k = 493.7 MeV/c^2 is the kaon mass and p_{CM} is the momentum kick of kaons in the central magnet. The kick value is $\approx$ 300 MeV/c for the $++$ magnetic field configuration and gives us the intruder peak at $m_{int} = 1.15$ GeV/c^2 . In the $\phi \rightarrow K^+K^-$ analysis the tracks remaining after the DC ghost rejection are tested to check whether they belong to the same TOF slat or EMCal tower. If such tracks are found both of them are rejected. The majority of the artificial tracks are DC ghosts and the fraction of the polluted by DC ghosts events is close to values quoted in the Table 3.6. The amount of intruder pairs which are localized near m_{int} is negligibly small, of about 0.3% of the total number of pairs, and is not taken into account in the evaluation of the correction function.

3.5 Pair analysis

The aim of the pair analysis is to extract the ϕ-meson signal from the sample of identified particles obtained at the previous stage. It is achieved by using a statistical procedure in which all particles in a given event are combined into pairs to generate unlike- and like-sign invariant mass spectra. By construction the unlike-sign spectrum contains both the signal and an inherent combinatorial background of uncorrelated pairs. The size and shape of the combinatorial background are determined using the event mixing technique which is described below. Finally, we derive the signal mass distribution by subtracting the normalized mixed event unlike-sign spectrum from the measured one.

In the $\phi \rightarrow K^+K^-$ analysis, kaons identified by the TOF and EMCal detectors are combined into pairs using four different detector combinations:

- Both K^+ and K^- identified by TOF detector (TOF-TOF combination).
- K^+ identified by TOF and K^- by PbSc detector (TOF-EMC$_{EAST}$ combination).

- Both K^+ and K^- identified by PbSc in east arm (EMC_{EAST}-EMC_{EAST} combination).
- Both K^+ and K^- identified by PbSc in west arm (EMC_{WEST}-EMC_{WEST} combination).

In the present analysis we do not use K^+ from PbSc and K^- from TOF because of the very low acceptance for such pairs in the ϕ mass region.

3.5.1 Invariant mass spectra and combinatorial background

Mixing of minimum bias events The event mixing procedure, originally proposed by Kopylov [70] and later by Drijard, Fischer, and Nakada [71] and L'Hote [72] provides a powerful method for estimating the combinatorial background distribution. In this technique an artificial mixed event is formed by combining all tracks from one event, A, to all tracks from another event, B, provided that events A and B belong to the same centrality and vertex classes. The procedure generates unlike- and like-sign mixed event invariant mass spectra. The mixed event invariant mass distributions by construction do not contain any particle correlations. The main advantage of the event mixing technique is that one can generate as many mixed events as needed to get a precise determination of the shape of the combinatorial background spectrum, thereby practically eliminating the point-to-point statistical fluctuations in the combinatorial mass spectrum.

In the present analysis the event mixing technique is performed by keeping a buffer of events for each centrality and vertex class. The tracks from the analyzed event are combined to the tracks from N_{buff} *buffered events of the same centrality and vertex class*, where N_{buff} is chosen to provide enough statistics in the background spectra. In the Run 4 $Au+Au$ analysis we use a buffer depth of 20, with 40 centrality and 20 vertex classes.

Mixing of triggered events The procedure described above is valid for minimum bias events only. In the case of triggered events there is a strong bias and triggered events cannot be mixed with other triggered events. The event mixing procedure used in the $\phi \rightarrow e^+e^-$ analysis from Run 3 $d+Au$ run is illustrated in Fig. 3.16. All electrons (positrons) from an event where the ERT trigger was fired by an electron (positron) are combined with the electrons and positrons from a buffer of minimum bias events ($N_{buff} = 500$ events) provided that all events belong to the same centrality and vertex classes. In this analysis we use $N_{cent} = 5$ and $N_{vtx} = 30$. All mixed events generated by this procedure will automatically fulfill the ERT condition.

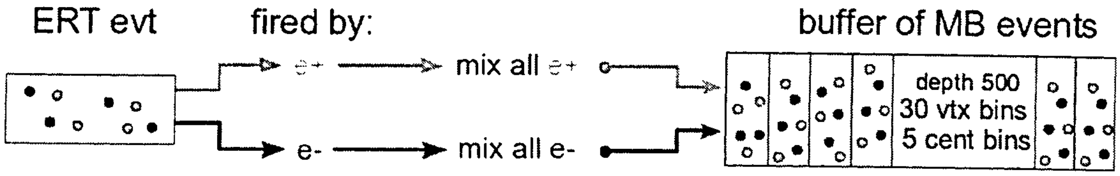

Figure 3.16: The event mixing procedure in ERT data.

Normalization of the combinatorial background The mixed event invariant mass distribution constructed in the way described above properly reproduces the shape of the real combinatorial background, but needs to be normalized before it is subtracted from the measured unlike-sign spectrum. Under the assumption that the number of tracks per event follows a Poisson distribution one can prove that the size of the real combinatorial background is exactly given by $2\sqrt{N^{++}N^{--}}$ yield, where N^{++} and N^{--} represent the measured like-sign pair yields.

Crosscheck of the normalization

- $\phi \rightarrow e^+e^-$ analysis in $Au+Au$ run. The quality of the combinatorial background reproduction is assessed by comparing the like-sign spectra ($++$ and $--$ pairs) of the real and mixed events. Fig. 3.17 shows an example of the real and mixed e^+e^+ like-sign spectra (left panel) and their ratios (right panel) for the $++$ magnetic field configuration. The like-sign mixed event spectrum reproduces very well the shape of the measured distributions except for the low-mass region for $m_{inv} \lesssim 200$ MeV/c^2 where correlated e^+e^+ and e^-e^- pairs from π^0 Dalitz decays (where the photon undergoes conversion) contribute to the measured like-sign invariant mass spectrum. These correlations are taken out by replacing the N^{++} and N^{--} yields with $\mathrm{R}^{++}_{m>200}\mathrm{N}^{++}_{mixed}$ and $\mathrm{R}^{--}_{m>200}\mathrm{N}^{--}_{mixed}$, respectively. $\mathrm{R}^{++}_{m>200}$ and $\mathrm{R}^{--}_{m>200}$ are the ratios of the like-sign measured over mixed integral yields calculated for the masses $m_{inv} > 200$ MeV/c^2 . The normalization factor is therefore given by:

$$\alpha = \frac{2\cdot\sqrt{R^{++}_{m>200}N^{++}_{mixed} \times R^{--}_{m>200}N^{--}_{mixed}}}{N^{+-}_{mixed}/(2N_{buff})}, \qquad (3.6)$$

Although the ratios of the measured like-sign spectra to the mixed ones are found to be flat above $m_0 > 200$ MeV/c^2 for e^+e^+ and e^-e^- pairs and for the $++$ and $--$ magnetic fields configurations the normalization factors are slightly, by $\lesssim$1%

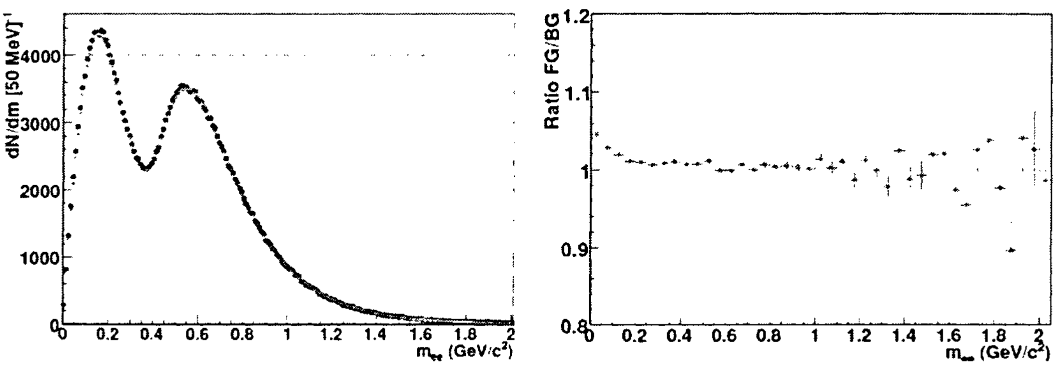

Figure 3.17: Measured (blue) and mixed-event (red) e^+e^+ like-sign spectra (left) and their ratios (right) for the $++$ magnetic field configuration in $Au+Au$ collisions. The mixed like-sign spectra is normalized using Eq. 3.6.

for the minimum bias events and by ~2-4% for peripheral ones, different from the expected value of 1. The values of α calculated for the MB, 0-20%, 20-40% and 40-92% are 1.006 ± 0.001, 1.004 ± 0.001, 1.015 ± 0.001 and 1.045 ± 0.004, respectively. This discrepancy is attributed to the fact that the number of electrons per event is distributed according to a Negative Binomial Distribution (NBD) rather than by a Poisson distribution.

- $\phi \rightarrow e^+e^-$ analysis in $d+Au$ run. A comparison of the real and mixed event like-sign spectra and their ratio for events with a trigger threshold of 600 MeV are shown in Fig. 3.18. In this case the like-sign mixed event spectrum also reproduces quite well the shape of the real distribution. The peak in the low-mass region of the measured like-sign spectrum is more pronounced compared to the $Au+Au$ analysis due to the significantly smaller combinatorial background. The mixed event spectrum is normalized using Eq. 3.6 for $m_0 > 1$ GeV/c^2 where the reproducibility of the real spectrum is very good.
- $\phi \rightarrow K^+K^-$ analysis in $Au+Au$ run. The good reproducibility of the measured spectra and the validity of the mixing event technique in the case of the $\phi \rightarrow K^+K^-$ TOF-TOF analysis is demonstrated in Fig. 3.19.

3.5.2 ϕ-meson signal extraction

The mixed event spectra are normalized separately for the different magnetic fields in the Run 4 $\phi \rightarrow e^+e^-$ and $\phi \rightarrow K^+K^-$ analyses and for the different trigger thresholds in the Run 3 $\phi \rightarrow e^+e^-$ analysis. Then the signal yield is extracted by subtracting the

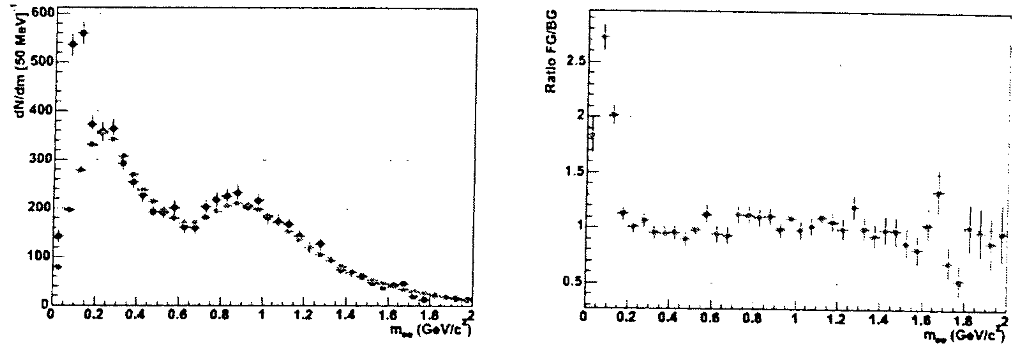

Figure 3.18: Measured (blue) and mixed-event (red) e^+e^+ like-sign spectra (left) and their ratios (right) for the 600 MeV ERT threshold in $d+Au$ collisions.

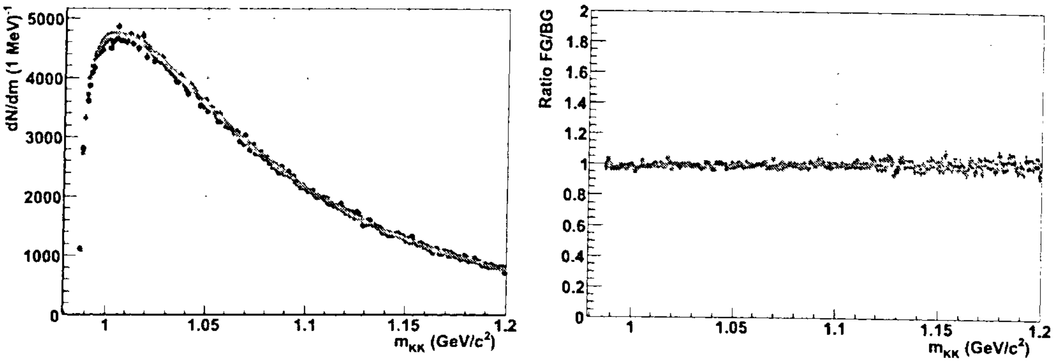

Figure 3.19: Measured and mixed-event K^+K^+ like-sign spectra (left) and their ratios (right) for the $++$ magnetic field configuration in $Au+Au$ collisions.

normalized unlike-sign mixed event invariant mass spectra from the measured one. After subtraction the spectra can be summed to form the total signal spectrum. The total e^+e^- signal spectra derived from $d+Au$ events and from the $Au+Au$ minimum bias events are shown in Fig. 3.20 in the top and bottom panels, respectively.

The ϕ meson yield is derived using two methods: (i) by summing the content of the bins over a mass interval of $\pm 3\sigma_{tot}$, $S_\phi(\Sigma)$, and (ii) integrating the fitting function over the $\pm 3\sigma_{tot}$ interval around the ϕ meson peak, $S_\phi(\int)$. σ_{tot} is the total width calculated from the quadrature sum of the experimental mass resolution, σ_{exp}, and the natural width of the ϕ meson, $\sigma_\phi = \Gamma_\phi/2.35$. The values of σ_{exp} are extracted from simulations by fitting the reconstructed ϕ peak with a relativistic Breit-Wigner function convoluted with a Gaussian distribution with a free σ parameter reflecting the experimental mass resolution. The

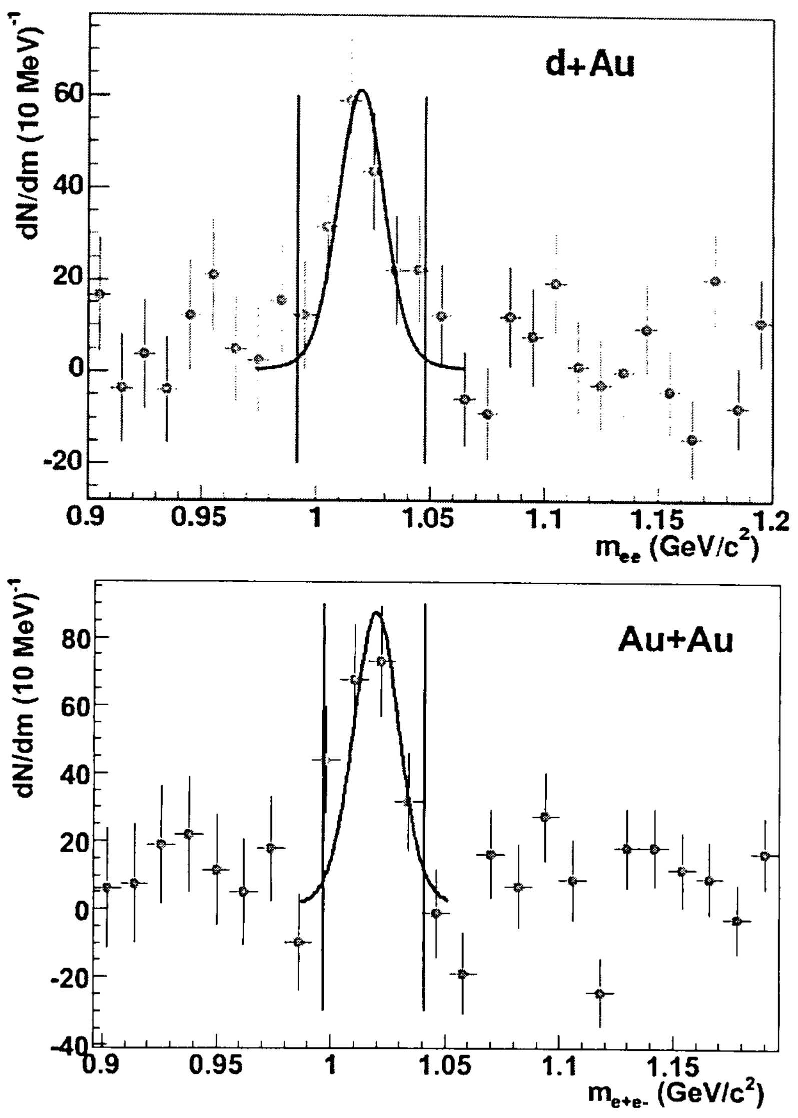

Figure 3.20: The subtracted $\phi \longrightarrow e^+e^-$ invariant mass spectra for the ERT events in the $d+Au$ (top) and for the peripheral (50-92.2%) events in the $Au+Au$ (bottom) analyses. The ϕ yield is extracted using a histogram with a fine bin of 1 MeV/c^2 in the mass interval shown by the vertical bars.

relativistic Breit-Wigner parametrization is given by:

$$Y(m) \sim \frac{m \cdot m_\phi \cdot \Gamma_\phi}{(m^2 - m_\phi^2)^2 + (m_\phi \cdot \Gamma_\phi)^2} \tag{3.7}$$

where the centroid m_ϕ and full width Γ_ϕ are fixed to the PDG values, see Section 1.3.1.

The extracted values of σ_{exp} are 9.1 and 6.5 MeV/c^2 for the Run 3 and Run 4 $\phi \rightarrow e^+e^-$ data, respectively. The improvement of the experimental mass resolution in Run 4 is due to the increased strength of the magnetic field. The blue lines in Fig. 3.20 represent the result of fitting the signal distributions with the convoluted function having the centroid, full width and mass resolution fixed, so that the only free parameter is the peak amplitude.

Signal to background ratios and yields derived from these two methods for Run 3 (for a mass window of $0.991 < m < 1.048$ GeV/c^2) and Run 4 (for a mass window of $0.997 < m < 1.041$ GeV/c^2) $\phi \rightarrow e^+e^-$ analyses are listed in Table 3.7. The quality of the measured signal is determined by the S/B ratio and it is convenient to calculate an effective signal, S_{eff} which represents the signal of the same statistical significance in the absence of background, *i.e.* a background-free signal, $S_{eff} = S/(1+2B/S)$. The value of S_{eff} is quoted in Table 3.7 as well. As one can see the significance of the signal in the central $Au+Au$ collisions is rather low due to small S/B ratio and improves as one goes to peripheral or $d+Au$ collisions where the S/B ratio is much better. The yields derived by the two methods are consistent with each other within the statistical errors. For the analysis of the final results, the ϕ meson yield obtained by summing the data points is used.

Table 3.7: Yields, signal to background ratio and effective signal S_{eff} of the ϕ meson via the e^+e^- decay channel. $S_\phi(\Sigma)$ and $S_\phi(\int)$ are the yields extracted by the channel count and function integration methods as explained in the text.

	Event class	S/B	$S_\phi(\Sigma)$	$S_\phi(\int)$	S_{eff}
Run 3 $d+Au$ σ_{exp} = 9.1 MeV/c^2 σ_{tot} = 9.3 MeV/c^2 $0.991 < m(\text{GeV}/c^2) < 1.048$	ERT	1/4	184.2 ± 31.2	162.0 ± 25.6	21.4
Run 4 $Au+Au$	MB	1/76	1773 ± 372	1607 ± 309	11.3
σ_{exp} = 6.5 MeV/c^2	0 - 20%	1/157	710 ± 340	634 ± 244	2.3
σ_{tot} = 6.8 MeV/c^2	20 - 40%	1/30	602 ± 140	626 ± 142	9.8
$0.997 < m(\text{GeV}/c^2) < 1.041$	40 - 92%	1/6	415 ± 54	302 ± 39	33.0

The $\phi \rightarrow K^+K^-$ invariant mass spectrum derived from the TOF-TOF analysis for minimum bias events is shown in Fig. 3.21. The ϕ meson peak is fitted with a relativistic Breit-Wigner function convoluted with a Gaussian distribution. The only free parameter of the fit is the peak integral while the centroid, m_ϕ, and the full width, Γ_ϕ, are fixed to the PDG values. The experimental mass resolution is extracted from simulation, σ_{exp} = 1.2

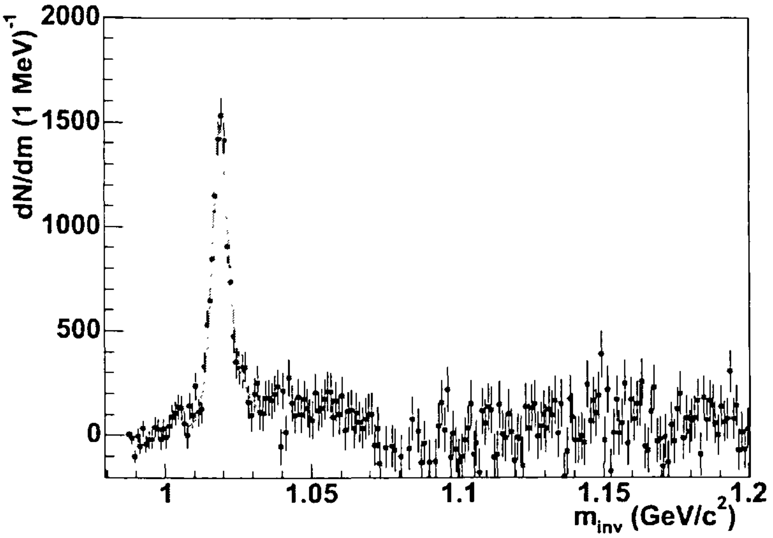

Figure 3.21: The $\phi \rightarrow K^+K^-$ MB invariant mass spectra for the TOF-TOF combination.

Table 3.8: Yields, signal to background ratio and effective signal S_{eff} of the ϕ meson via the K^+K^- decay channel for the TOF-TOF combination.

	MB	0-10%	10-20%	20-30%
N_ϕ	9996 ± 251	2670 ± 163	2540 ± 134	1924 ± 99
S/B	1/5	1/6	1/4	1/2.8
S_{eff}	909	205	508	506
	30-40%	40-50%	50-60%	60-90%
N_ϕ	1267 ± 69	787 ± 46	484 ± 31	328 ± 22
S/B	1/2.8	1/1.7	1/0.9	1/0.5
S_{eff}	333	292	255	219

MeV/c^2. The signal to background ratios and the yields derived by summing the content of the bins over the mass interval 1.014 GeV/c^2 $< m <$ 1.024 GeV/c^2 and corresponding effective signal, S_{eff}, are listed in Table 3.8. The total yield and S/B ratio derived from the analysis of all possible detector combinations are equal to $\sim$ 44000 ± 770 and $\sim$ 1/10, respectively.

3.6 Absolute normalization

The rapidity density (dN/dy) and inverse slope (T) are determined using the absolutely normalized transverse mass (m_T) distribution. The raw m_T spectra are obtained by dividing the yield of the measured and mixed-event unlike-sign invariant mass spectra extracted within a defined mass window (see Section 3.5.2) into bins in m_T and then subtracting them, bin by bin. This determines the number of reconstructed ϕ mesons in each m_T bin.

This approach relies on the assumption that the normalization of the mixed event spectrum does not depend on m_T. The validity of this assumption is demonstrated by the ratio of the measured to the mixed like-sign m_T spectra. An example of such m_T spectra ratio for e^+e^+ in the $Au+Au$ analysis for the $++$ field configuration is shown in Fig. 3.22 along with the fit with a polynomial of zero degree. One can see that the ratio is reasonably flat.

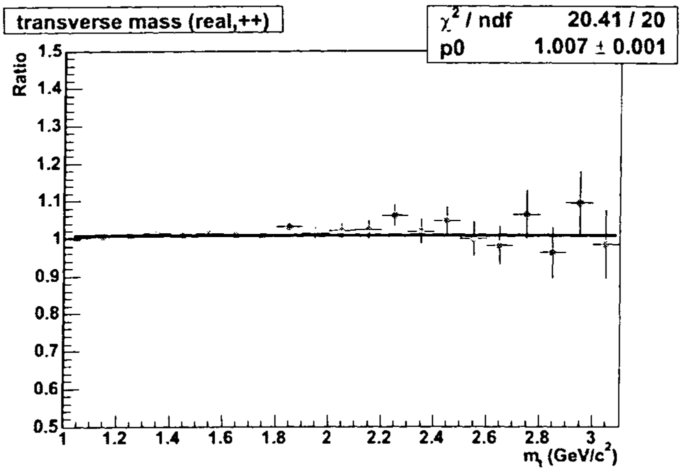

Figure 3.22: Ratios of the m_T measured and mixed spectra for the $++$ field configuration.

The absolutely normalized m_T distributions of the ϕ mesons are obtained by applying various corrections to the raw spectra to account for the features of the apparatus and analysis procedure. PHENIX measures particles in a limited acceptance which is determined by the detector geometry and the magnetic field. Furthermore, only a fraction of the particles falling inside the acceptance get reconstructed by the analysis software. Therefore the measured raw yields need to be corrected for acceptance and reconstruction effects. In addition to that, the track reconstruction efficiency depends on the detector occupancy. In the high multiplicity environment of central $Au+Au$ collisions the high detector occupancy results in a lower track reconstruction efficiency compared to peripheral events.

Finally, we have to take into account that the detector performance is not uniform over time.

The corrected and absolutely normalized invariant transverse mass spectrum of the ϕ mesons is given by:

$$\frac{1}{2\pi m_T}\frac{d^2N}{dm_T dy} = \frac{N^{\phi}_{raw}(m_T)\cdot CF(m_T)\cdot \varepsilon_{trigger}(m_T)}{2\pi m_T\cdot N_{events}\cdot \varepsilon_{run-by-run}\cdot \varepsilon_{pair-embedding}\cdot BR\cdot \Delta m_T}, \tag{3.8}$$

where:

- $N^{\phi}_{raw}(m_T)$ is the raw ϕ yield in a given m_T bin.
- $CF(m_T)$ is the correction factor to account for acceptance and pair reconstruction efficiency, derived from single particle Monte Carlo simulations (see Section 3.7).
- $\varepsilon_{trigger}(m_T)$ is the electron trigger efficiency. For the analysis of minimum bias events $\varepsilon_{trigger}(m_T)$ is equal to one.
- N_{events} is the number of analyzed events.
- $\varepsilon_{pair-embedding}$ is the pair embedding efficiency to account for the reconstruction efficiency losses due to detector occupancy (see Section 3.8).
- $\varepsilon_{run-by-run}$ accounts for run-by-run variations of the detector performance(see Section 3.9).
- BR is the branching ratio for the corresponding decay channel.
- and Δm_T is the bin size.

The $\phi \rightarrow e^+e^-$ m_T spectra are corrected separately, for the 600 and 800 MeV thresholds in the $d+Au$ analysis, and for the $++$ and $--$ magnetic fields configurations in the $Au+Au$ analysis. In the $\phi \rightarrow K^+K^-$ analysis the m_T spectra are generated and then corrected separately for each detector combination and for the $++$ and $--$ magnetic fields configurations.

The combined transverse mass spectrum was obtained as a weighted average of the corresponding contributions.

The ϕ meson transverse mass spectra are obtained for:

- minimum bias events in the $\phi \rightarrow e^+e^-$ analysis of $d+Au$ collisions.
- minimum bias events, 20-40% and 40-92% centrality bins in the $\phi \rightarrow e^+e^-$ analysis of $Au+Au$ collisions.
- minimum bias events, 0-10%, 10-20%, 20-30%, 30-40%, 40-50%, 50-60% and 60-90% centrality bins in the $\phi \rightarrow K^+K^-$ analysis of $Au+Au$ collisions.

3.7 Monte Carlo Simulation

The primary tool to correct for the acceptance and reconstruction efficiency is the single-particle Monte Carlo and GEANT-based "PHENIX Integrated Simulation Application" (PISA) which allows to reconstruct simulated particles using the same analysis software as for the real data. PISA uses a set of characteristics (detector materials and geometry, dead and hot channel maps, gains, noise levels *etc.*) which describe the performance of each subsystem during a selected reference period of time for each run. The general strategy to derive the correction is described below:

- use the single-particle generator *EXODUS* that was developed within PHENIX [73] to generate a sample of ϕ-mesons with the following parameters:
  - flat vertex distribution within $|z_{vtx}| < 30$ cm.
  - flat rapidity distribution within $|y| \leq 0.6$ and uniform in φ: $0 \leq \varphi \leq 2\pi$.
  - exponential transverse momentum distribution,

    $$dN/dp_T = p_T exp(-\frac{m_T}{T}),$$

    where T is the inverse slope. The inverse slope values used in the $\phi \rightarrow e^+e^-$ and $\phi \rightarrow K^+K^-$ simulation projects are listed in Table 3.9.

Table 3.9: Number of generated events and inverse slope parameters used in the $\phi \rightarrow e^+e^-$ and $\phi \rightarrow K^+K^-$ simulation projects.

Project	$\phi \rightarrow e^+e^-$, $d+Au$	$\phi \rightarrow e^+e^-$, $Au+Au$	$\phi \rightarrow K^+K^-$, $Au+Au$
$N_{generated}$, $\times 10^6$	5	5 for each field	25 for each field
T (MeV)	320	366	440

- decay the generated ϕ-mesons into e^+e^- or K^+K^- pairs within *EXODUS*
- pass the resulting output through the full emulator of the PHENIX detector, PISA.
- tune the PISA output variables to those in the data.
- tune the track matching to the EMCal and the energy-momentum matching, *dep*.
- process the reconstructed output through the trigger emulator to correct for the trigger efficiency, if needed.
- generate the m_T spectrum of the reconstructed ϕ-mesons using the same analysis chain as used for the real data.

The ratio of the number of generated ϕ mesons to the number of reconstructed ϕ mesons in each m_T bin gives the correction function $CF(m_T) = N^{gen}(m_T)/N^{rec}(m_T)$. The measured raw spectrum is multiplied by $CF(m_T)$ to correct the m_T spectra for acceptance and reconstruction efficiencies.

Due to the limited statistics the bins have a rather large width of the order of several hundreds MeV. This introduces several effects that have to be taken into account. First, for a rapidly varying function, as in the case of m_T distributions, the true position of a point is shifted with respect to the center of the bin and lies at the center of gravity (c.o.g) of the bin. In the present analysis the points are plotted at the c.o.g of the measured exponential spectrum. Second, in the case of wide bins the correction factor is sensitive to the slope of the generated spectrum. This effect is included into the systematic uncertainty.

When the statistics is too low to determine the m_T distribution, the total signal yield can be corrected for acceptance and efficiency using an integral correction factor. Assuming a given temperature, T, the correction factor is given as the ratio of the total number of generated ϕ mesons to the total number of reconstructed ϕ mesons: $CF = N^{gen}/N^{rec}$, where N^{gen} and N^{rec} are derived by integrating $N^{gen}(m_T)$ and $N^{rec}(m_T)$ over the full m_T range.

3.7.1 The RICH variables in simulation and data

The Monte Carlo RICH variables $n0$, $n1$, Q_{ring} and $disp$ used for the electron identification are tuned to reproduce the data. Comparisons of the RICH variables in the data to the tuned ones in the simulation are shown in Fig. 3.23 by the blue and red histograms, respectively. All distributions are shown after background subtraction and are normalized to have the same total area.

3.7.2 Matching to EMCal and *dep* in the simulation

The matching of the reconstructed tracks to the EMCal along the z and φ directions and the energy-momentum matching, E/p- 1, in the simulation are translated into the reduced variables $\sigma_{EMC}^{MC,z}$, $\sigma_{EMC}^{MC,\varphi}$ and dep^{MC}, like it is done in the data (see Section 3.4.2). The mean and sigma values of the EMCal variables are tuned to be centered, respectively, around 0 and 1. The distributions of the EMCal reduced variables in the simulation as function of p_T are shown in Fig. 3.24 for one EMCal sector.

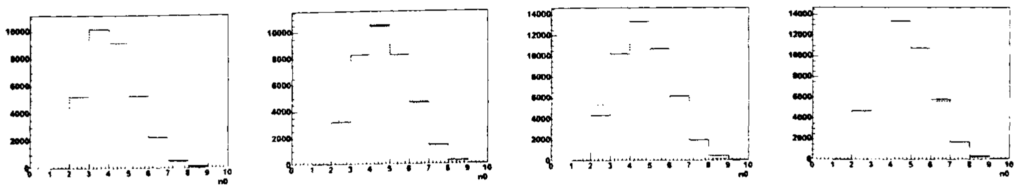

(a) $ES\ n0$ (b) $EN\ n0$ (c) $WS\ n0$ (d) $WN\ n0$

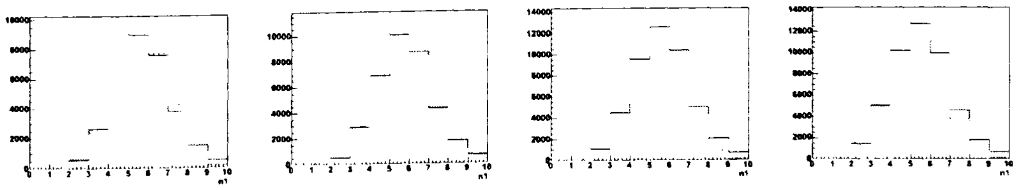

(e) $ES\ n1$ (f) $EN\ n1$ (g) $WS\ n1$ (h) $WN\ n1$

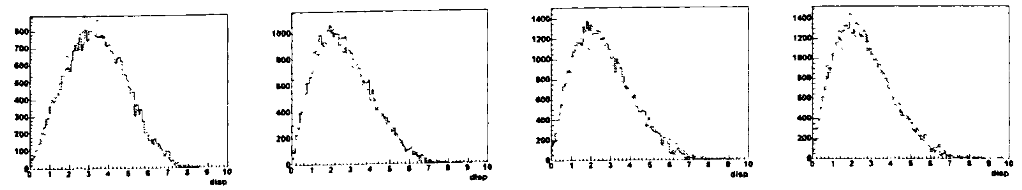

(i) $ES\ disp$ (j) $EN\ disp$ (k) $WS\ disp$ (l) $WN\ disp$

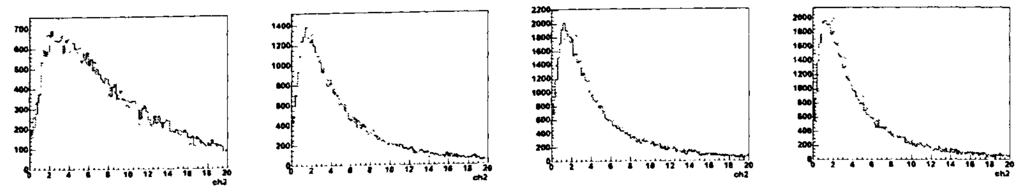

(m) $ES\ Q_{ring}$ (n) $EN\ Q_{ring}$ (o) $WS\ Q_{ring}$ (p) $WN\ Q_{ring}$

Figure 3.23: RICH eID variables $n0$, $n1$, $disp$ and Q_{ring} in the data (blue) and in the simulation (red) for each RICH sector.

3.7.3 Correction function for the $\phi \to e^+e^-$ analysis in $Au+Au$ collisions

The generated, accepted[1] and reconstructed m_T spectra for the $++$ and $--$ field configurations are overlaid in the left panel of Fig. 3.25.

The distributions are almost identical for both fields. The ratio of the generated spectrum to the reconstructed one, right panel of Fig. 3.25 gives the correction function. The solid symbols correspond to the $++$ field and open ones to the $--$ field.

---

[1] The accepted m_T spectrum is the spectrum of the ϕ mesons which pass the acceptance filter determined by the DC-PC1-EMCal.

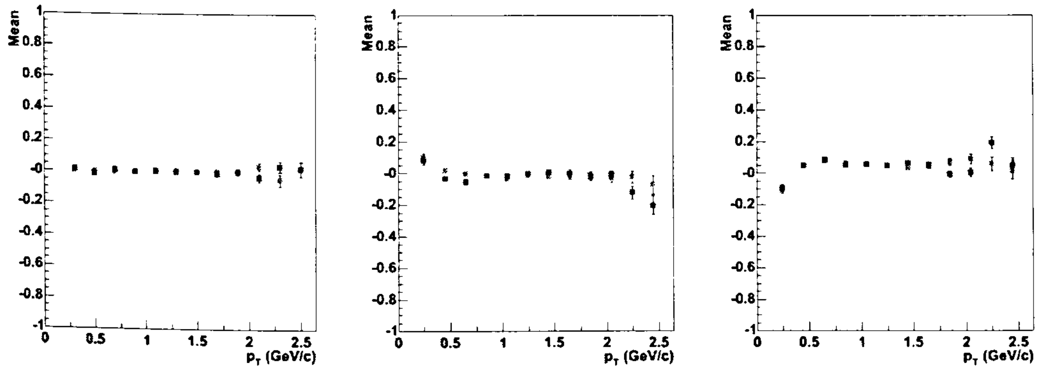

(a) $\sigma_{EMC}^{MC,z}$-mean (b) $\sigma_{EMC}^{MC,\varphi}$-mean (c) dep^{MC}-mean

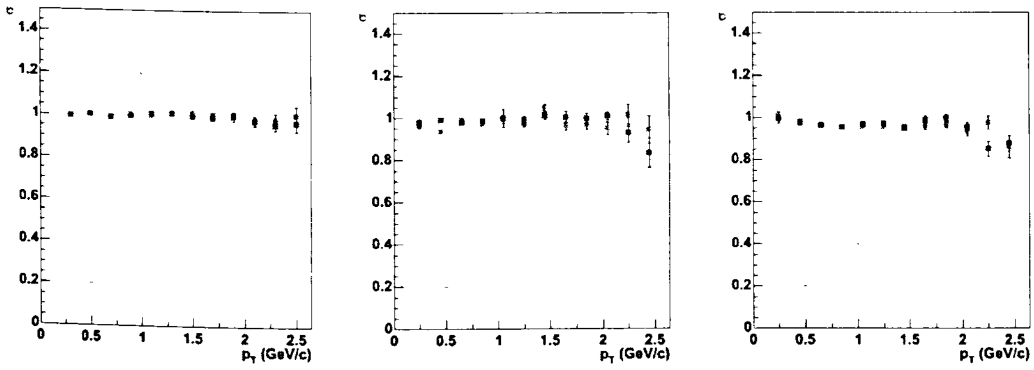

(d) $\sigma_{EMC}^{MC,z}$-sigma (e) $\sigma_{EMC}^{MC,\varphi}$-sigma (f) dep^{MC}-sigma

Figure 3.24: Mean and sigma values of the track matching along the $\sigma_{EMC}^{MC,z}$- and $\sigma_{EMC}^{MC,\varphi}$-coordinates and for the dep^{MC} variable in one EMcal sector of the East arm as a function of p_T in the MC simulation. Blue and red points represent electrons and positrons, respectively.

3.7.4 Correction function for the $\phi \rightarrow K^+K^-$ analysis in $Au+Au$ collisions

The generated and reconstructed m_T spectra using the TOF detector for the $++$ and $--$ field configurations are overlaid in Fig. 3.26 (left panel). The distributions are identical for both fields within the statistical errors of the simulation. The ratio of the generated spectrum to the reconstructed one (Fig. 3.26 right panel) gives the correction function. The solid symbols correspond to the $++$ field and open ones to $--$ field, respectively.

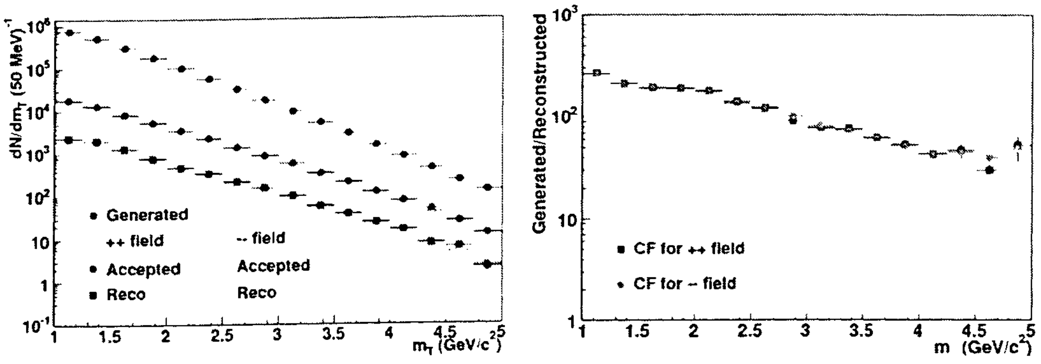

Figure 3.25: Generated, accepted and reconstructed m_T spectra for the $++$ and $--$ field configurations (left panel) and corresponding correction function (right panel) for the $Au+Au$ $\phi \rightarrow e^+e^-$ analysis.

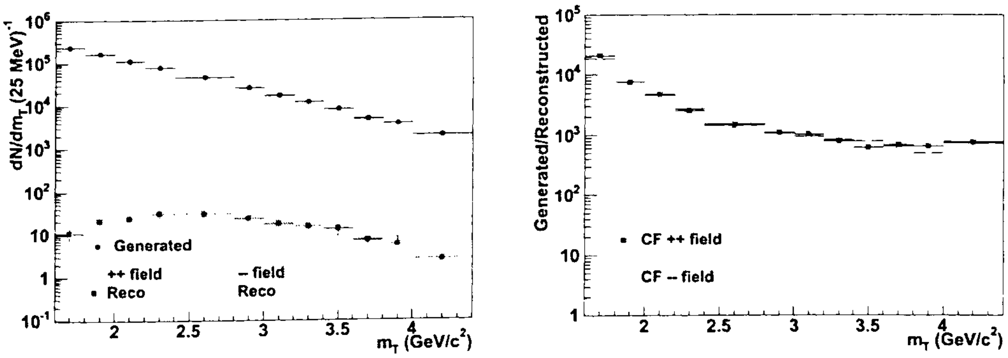

Figure 3.26: Generated, accepted and reconstructed m_T spectra using the TOF detector for the $++$ and $--$ field configurations (left panel) and corresponding correction functions (right panel) for the $Au+Au$ $\phi \rightarrow K^+K^-$ analysis.

3.7.5 Correction function for the $\phi \rightarrow e^+e^-$ analysis of the $d+Au$ data

The analysis of the triggered events in $d+Au$ was performed independently for the 600 and 800 MeV thresholds. To correct the measured m_T spectrum for the trigger efficiency (see Section 3.3) the reconstructed e^+e^- pairs are processed through an emulator of the ERT trigger. The emulator relies on the single-electron ERT efficiency determined as described in Section 3.3. Both electron and positron of each reconstructed ϕ meson are examined for the trigger condition:

- the electron and the positron are assigned a weight , w, randomly generated with flat distribution between 0 and 1.

- The ϕ meson satisfies the ERT trigger if either the electron or the positron satisfies the trigger condition $w > \varepsilon_{ERT}$ where ε_{ERT} is the ERT efficiency determined for the momentum of the electron or positron.

The generated, accepted and reconstructed m_T spectra for the MB, 600 and 800 MeV thresholds are shown in the left panel of Fig. 3.27. The corresponding correction functions are shown in the right panel of Fig. 3.27.

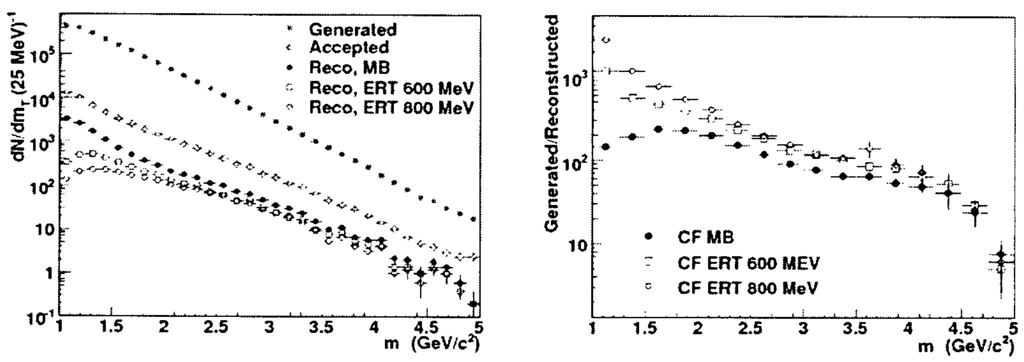

Figure 3.27: Generated, accepted and reconstructed m_T spectra for MB, 600 and 800 MeV thresholds (left panel) and corresponding correction functions (right panel) for the $d+Au$ $\phi \rightarrow e^+e^-$ analysis.

3.8 Embedding corrections

Hit merging effects may lead to wrong hit associations and to track mis-reconstruction. This effect is important in a high multiplicity environment, such as heavy-ion collisions, and reveals itself as a decrease of the track reconstruction efficiency with increasing track density or centrality.

In order to determine the fraction of tracks which are lost and correct for these inefficiencies, an embedding technique is used. In this technique the hits produced by single particles from the Monte Carlo simulation are merged with the raw detector hits of events of different centrality classes. Comparing the number of particles reconstructed with and without embedding one can extract the reconstruction efficiency as a function of event multiplicity. The embedding efficiencies for ϕ are calculated as the product of the embedding efficiencies of the single particles, $\varepsilon^{emb}_{e^+/K^+}$ and $\varepsilon^{emb}_{e^-/K^-}$:

$$\varepsilon^{emb}_{\phi} = \varepsilon^{emb}_{e^+/K^+} \times \varepsilon^{emb}_{e^-/K^-} \tag{3.9}$$

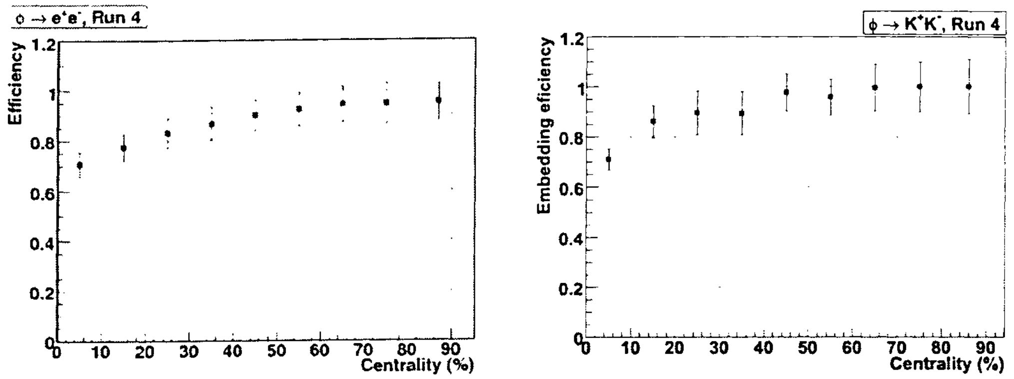

Figure 3.28: Embedding pair efficiency for $\phi \longrightarrow e^+e^-$ (left) and $\phi \longrightarrow K^+K^-$ for the TOF-TOF combination (right) in Run 4, $Au+Au$ collisions.

The pair embedding efficiencies in the $\phi \longrightarrow e^+e^-$ and $\phi \longrightarrow K^+K^-$ analyses are shown in the left and right panels of Fig. 3.28, respectively.

The existing embedding software operates with single tracks and therefore the pair cuts (*e.g.* ghost rejection, see Section 3.4.4), which reduce the number of reconstructed ϕ-mesons, are not taken into account in the embedding efficiency calculation. The effect of the pair cuts was estimated by counting the number of measured unlike-sign pairs in the mass window $0.997 < m(\mathrm{GeV}/c^2) < 1.041$ with and without pair cuts. Table 3.10 shows the corresponding numbers for the different centrality bins.

Table 3.10: Efficiency of the pair cuts for the ϕ-meson electron pairs.

Centrality %	**Number of pairs, $0.997 < m(\mathrm{GeV}/c^2) < 1.041$**		**Fraction**
	No pair cuts	**With pair cuts**	
MB (0-92)	43576	40480	0.929
0 - 20	36926	34080	0.923
20 - 40	5883	5643	0.959
40 - 92	767	757	0.987

The final embedding efficiency which takes into account the efficiencies of the pair cuts for MB and the three centrality bins used in this analysis are quoted in the Table 3.11.

The multiplicity effects in $d+Au$ collisions are negligibly small and do not need to be corrected.

Table 3.11: Total, embedding and pair cuts, efficiencies for the ϕ-meson electron pairs.

Centrality %	MB (0-92)	0 - 20	20 - 40	40 - 92
Embedding efficiency	0.885	0.756	0.865	0.946
Pair cuts efficiency	0.929	0.923	0.959	0.987
Total	0.822	0.698	0.830	0.934

3.9 Run-by-run corrections

The pair analysis described above is based on the information provided by all subsystems used for the tracking and particle identification. Time variations in the performance of the subsystems result in variations of the ϕ yield. In the $\phi \rightarrow e^+e^-$ analysis in $Au+Au$ collisions these run-by-run yield variations are corrected by monitoring the number of unlike-sign pairs in the vicinity of the ϕ meson peak with respect to the reference run used in the simulation project. In each run i we calculate the average number of unlike-sign pairs from the ϕ meson peak region with respect to the reference run:

$$\varepsilon^i_{e^+e^-} = \frac{< N_{e^+e^-} >_i}{< N_{e^+e^-} >_{ref.run}} \tag{3.10}$$

The weighted average of the efficiencies in each run i, calculated separately for the $++$ and $--$ field configurations, gives the run-by-run pair efficiency:

$$\varepsilon^{run-by-run}_{pair} = \frac{\sum \varepsilon^i_{e^+e^-} \times N^i_{evt}}{\sum N^i_{evt}} \tag{3.11}$$

Due to the limited statistics this method is not applicable to the analysis of the $d+Au$ data. Instead, the run-by-run efficiency correction is derived by monitoring the average number of single particles per event in each run i normalized to the average number of single particles per event in the reference run:

$$\varepsilon^i_{e^+} = \frac{< N_{e^+} >_i}{< N_{e^+} >_{ref.run}}, \qquad \varepsilon^i_{e^-} = \frac{< N_{e^-} >_i}{< N_{e^-} >_{ref.run}} \tag{3.12}$$

The global run-by-run efficiency correction, $\varepsilon_{run-by-run}$, is calculated separately for each data set: for the 600 and 800 MeV thresholds as the weighted average of the efficiencies in each run i:

$$\varepsilon^{run-by-run}_{inclusive} = \frac{\sum \varepsilon^i_{inclusive} \times N^i_{evt}}{\sum N^i_{evt}} \tag{3.13}$$

where $\varepsilon^i_{inclusive} = \varepsilon^i_{e^+} \times \varepsilon^i_{e^-}$ is the relative pair efficiency in run i.

The pair efficiencies in the $d+Au$ and $Au+Au$ $\phi \rightarrow e^+e^-$ analyses are shown in the left and right panels of Fig. 3.29, respectively.

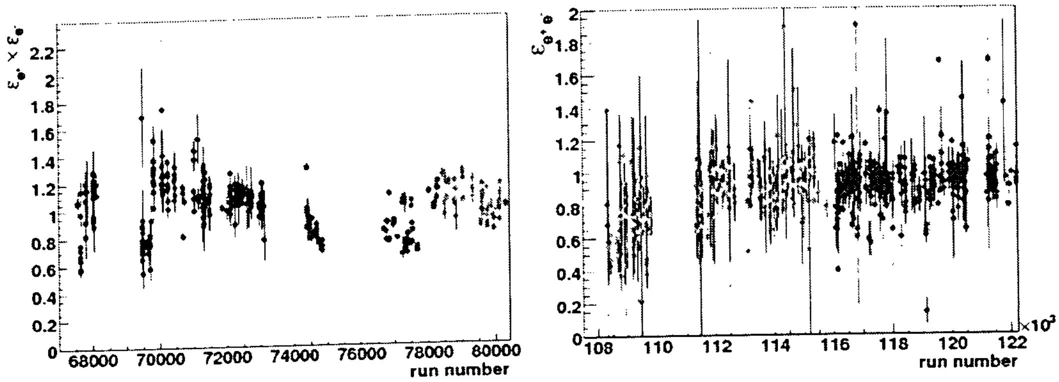

Figure 3.29: Run-by-run pair efficiencies for the $\phi \rightarrow e^+e^-$ analyses in $d+Au$ (left panel) and in $Au+Au$ (right panel) collisions. The blue and red points correspond to the data samples with 600 and 800 MeV thresholds, respectively, on the left panel and with $++$ and $--$ field configurations on the right panel.

The relative pair efficiency in the $\phi \rightarrow K^+K^-$ analysis is calculated using both methods: (i) by monitoring the average number of single kaons per events and (ii) by monitoring the K^+K^- pairs from the ϕ meson peak region. In the final analysis the run-by-run yield variations are corrected using method (i) and the difference between two methods is assigned as systematic uncertainty of the run-by-run correction.

Example of the relative pair efficiency in the $\phi \rightarrow K^+K^-$ analysis for the TOF-TOF combination is shown in Fig. 3.30.

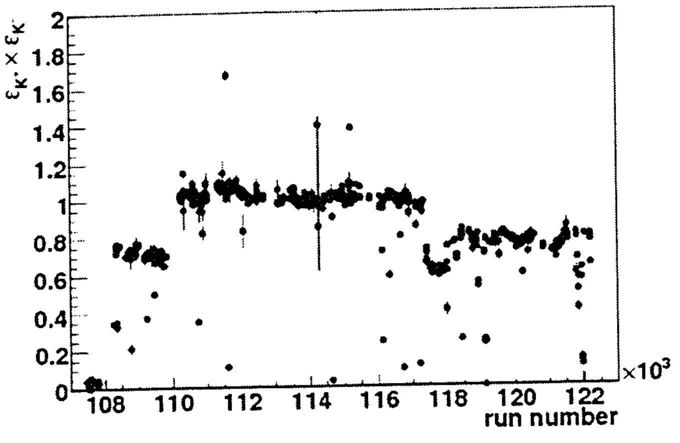

Figure 3.30: The K^+K^- relative pair efficiency *vs.* run number for the TOF-TOF combination.

Chapter 4

Results and discussion

The main goal of the present work is the measurement of the ϕ meson production through the dielectron and K^+K^- decay channels. It includes the study of the ϕ line-shape, its transverse mass distribution and extraction of the ϕ rapidity density invariant yield and inverse slope prameters. The centrality dependence of the line-shape parameters, ϕ meson yields and temperatures are investigated as well.

The rapidity density (dN/dy) and inverse slope or temperature (T) of the ϕ mesons are derived by fitting the fully corrected invariant m_T distribution of the ϕ mesons with an exponential function having two fitting parameters: the rapidity density dN/dy and the inverse slope or temperature T:

$$\frac{1}{2\pi m_T}\frac{d^2N}{dm_T dy} = \frac{dN/dy}{2\pi T(T+m_\phi)} exp(-(m_T - m_\phi)/T). \tag{4.1}$$

In the $Au+Au$ data the dielectron yield in the highest centrality bin, 0-20%, has limited statistics and a very poor S/B ratio and it is not possible to determine an m_T distribution. The dN/dy value for this centrality class is derived from the integral yield using the global correction factor obtained from the single particle MC simulation under the assumption that the inverse slope parameter T = 366 MeV [74] (see Section 3.7):

$$CF = \frac{N^{gen}}{N^{rec}} \tag{4.2}$$

where N^{gen} and N^{rec} are the integrated over m_T yield of the generated and reconstructed ϕ mesons, respectively.

4.1 Systematic uncertainties

Various sources contribute to the systematic errors in the yield and temperature determination. In most cases, the systematic errors are estimated by varying parameters, as described below, recalculating dN/dy and/or T and monitoring their deviations from the measured values. The *RMS* of the variation is assigned as systematic error. When an *RMS* cannot be determined, e.g. when the number of variations is small, the systematic error is derived using the maximum deviation from the measured value divided by $\sqrt{12}$. The factor of $\sqrt{12}$ derives from the standard deviation of a uniform density.

The main sources of systematic uncertainties are:

Normalization of the combinatorial background This is the dominant source of systematic uncertainty. Indeed, the uncertainty in the normalization of the combinatorial background translates into an uncertainty in the signal. This uncertainty is inversely proportional to the signal to background ratio, $(S/B)^{-1}$, and if the S/B ratio is small, as in the case of the $\phi \rightarrow e^+e^-$ analysis, even a small variation of the normalization factor can introduce dramatic changes in the signal. For example if the $S/B = 1/100$ then 1% error in the normalization factor changes the signal by a factor of two.

In the $\phi \rightarrow e^+e^-$ analyses this systematic error is estimated for each centrality bin from the maximum variation of the normalization factor α, see Eq. 3.6, calculated for different values of the mass cut-off m_0.

In the $\phi \rightarrow K^+K^-$ analysis this uncertainty was estimated from the maximum variation of the normalization factors derived using several methods:

- from the $2\sqrt{N^{++}N^{--}}$ method described in Section 3.5.
- normalizing the unlike sign mixed event spectrum to the measured one in the mass range $m > m_\phi$.
- using the absolute normalization provided by the event mixing method.

Particle identification The systematic error in electron identification was calculated by varying the eID parameters, $n0$, $disp$, Q_{ring}, dep, and the EMC track matching window both in the data and the MC. For each set of parameters the whole procedure was repeated (determination of ϕ yield, correction function, fitting of the m_T distribution). The *RMS* of the set of new values with respect to the measured values of dN/dy and T is used as systematic uncertainty. The systematic error in the kaon identification is very small and was neglected.

Monte Carlo simulation The main source of systematic uncertainties in the single particle MC simulation is the fiducial mismatch between data and Monte Carlo. It is evaluated by comparing the number of reconstructed tracks in the data and MC. Examples of the fiducial acceptance in the $d+Au$ data and MC determined by the Drift Chamber are shown in Fig. 4.1. In these figures, the MC was normalized to the data in a small two-dimensional DC_φ-DC_z window where there are no dead areas. The variation of the square of the data to MC ratios determined outside of the normalization window for different normalization windows gives an estimation of the systematic error. A similar procedure was used to estimate the systematic error in the $\phi \rightarrow e^+e^-$ and $\phi \rightarrow K^+K^-$ analyses of the $Au+Au$ data.

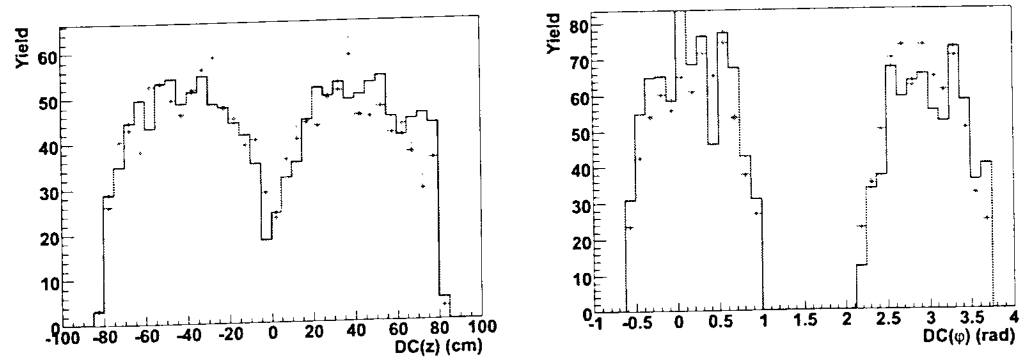

Figure 4.1: Fiducial comparison between MC and data for DC(z) (left) and DC(φ) distributions for the $\phi \rightarrow e^+e^-$ analysis in $d+Au$ run. Data are shown as blue lines and MC are shown as red points.

Sensitivity to the generated m_T spectrum The correction function CF(m_T) is a steeply falling function of m_T. In the case of large m_T bins the correction function depends on the generated m_T spectrum introducing systematic uncertainties in the yield and temperature. These uncertainties were estimated by varying the inverse slope parameter of the generated spectrum by ± 30 MeV which corresponds to ± 1 σ as determined from the exponential fit and repeating the whole analysis (new CF(m_T), new m_T spectra and new fits). The variation from the measured values of dN/dy is assigned as systematic error. The systematic uncertainty for the inverse slope value is found to be relatively small (of the order of 1%) and is neglected.

Embedding correction The systematic error due to the embedding procedure was estimated as a function of centrality by calculating the embedding correction with different track selection criteria and eID cuts.

Fitting procedure This uncertainty was estimated by fitting the m_T spectra within different m_T ranges, using two different fitting functions, exponential Eq. 4.1 and Boltzmann:

$$\frac{1}{2\pi m_T}\frac{d^2N}{dm_T dy} = \frac{(dN/dy)m_T}{2\pi T(2T^2+2m_\varphi T+m_\varphi^2)}exp(-(m_T-m_\varphi)/T). \tag{4.3}$$

Run-by-run efficiency uncertainty The systematic error of the run-by-run correction is derived from the two different methods of monitoring the variation of the number of inclusive electrons/kaons per event as explained in Section 3.9.

Mass window for the ϕ meson yield extraction This systematic error is estimated by varying the mass window over which the ϕ meson yield is determined.

ERT efficiency for the $d+Au$ analysis The systematic uncertainties in the ERT efficiency are evaluated by varying the single electron efficiency. For that the ERT efficiency distribution in each EMCal sector is parametrized with a function having a Wood-Saxon form, $f(p_T) = A/(1+exp(-B\cdot p_T+C))$, where A, B and C are the fit parameters. Examples of this parametrization for the WO EMCal sector is shown by black lines in Fig. 4.2. New values of dN/dy and T are recalculated using the parametrization of the electron efficiency in which each parameter A, B and C is varied by $\pm$ 1 $\sigma_{A,B,C}$, where $\sigma_{A,B,C}$ are the largest uncertainties on the fit parameters among the different EMCal sectors. Examples of the parametrization obtained by varying parameters A and C are shown by the color lines in the top and bottom panels of Fig. 4.2, respectively.

The systematic error in the ERT efficiency is calculated using the RMS of the variations of recalculated values of dN/dy and T from the measured ones.

Summary The individual systematic errors discussed above are totally independent and uncorrelated and therefore the total systematic error was derived by the quadratic sum of the individual contributions. Tables 4.1 and 4.2 summarize the various systematic errors for the two electron analyses described in this thesis. Table 4.3 summarizes the systematic errors in the $\phi \rightarrow K^+K^-$ analysis in MB $Au+Au$ collisions.

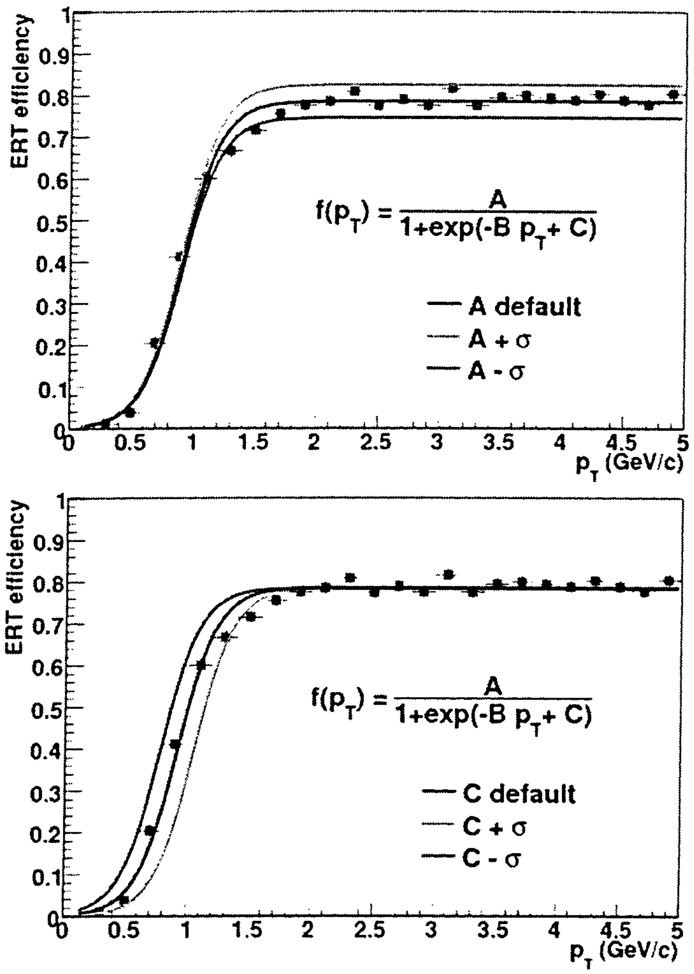

Figure 4.2: Parametrization of the single electron efficiency for the W0 EMCal sector (black lines). The color lines, red and blue, show the efficiency variation under ± 1 σ variations of the parameters A (top panel) and C (bottom panel).

In the $\phi \rightarrow K^+K^-$ analysis the systematic errors on dN/dy is estimated to be ~20% and ~17% for centralities $< 30\%$ and $> 30\%$, respectively. The centrality dependence of the systematic errors in the $\phi \rightarrow K^+K^-$ analysis is much weaker because the S/B ratio is much smaller. The systematic error in T is found to be 8% for all centrality bins.

Table 4.1: Systematic errors for the $\phi \rightarrow e^+e^-$ analysis in minimum bias $d+Au$ collisions.

	Normalization factor	ERT	eID	Fitting	Fiducial	Run-by-run	Total
dN/dy	11.7%	3.4%	8.6%	10.0%	9.9%	5.0%	21.1%
T	2.6%	0.8%	4.0%	-	-	-	4.8%

Table 4.2: Systematic errors in the $\phi \rightarrow e^+e^-$ analysis in $Au+Au$ collisions.

	dN/dy				T		
	MB	0-20%	20-40%	40-92.2%	MB	20-40%	40-92.2%
Normalization factor	27%	40%	8%	2%	8%	2%	1%
Electron ID	19.7%	24.7%	20.1%	13.5%	-	-	-
Mass window	12.1%	18.2%	3.2%	6.5%	1%	4.1%	0%
Fiducial	8%				-	-	-
Embedding	10%				-	-	-
Run - by - Run	3%				-	-	-
Total	37.9%	52.1%	25.5%	15.1%	8.1%	4.6%	1%

Table 4.3: Systematic errors for all detector combinations in the $\phi \rightarrow K^+K^-$ analysis in minimum bias $Au+Au$ collisions.

	Normalization factor	Fitting	Fiducial	Embedding	Mass window	Total
dN/dy	3.9%	8.8%	13.0%	10.0%	2.7%	22.5%
T	-	4.6%	-	-	4.9%	6.6%

4.2 Invariant transverse mass spectra, yields and temperatures

4.2.1 $\phi \rightarrow e^+e^-$ in $d+Au$ collisions

The invariant m_T spectrum of the ϕ mesons measured through the e^+e^- decay channel in minimum bias $d+Au$ collisions is shown in Fig. 4.3. The spectrum is fitted with the exponential function of Eq. 4.1 and the extracted values of dN/dy and T are quoted in Table 4.4.

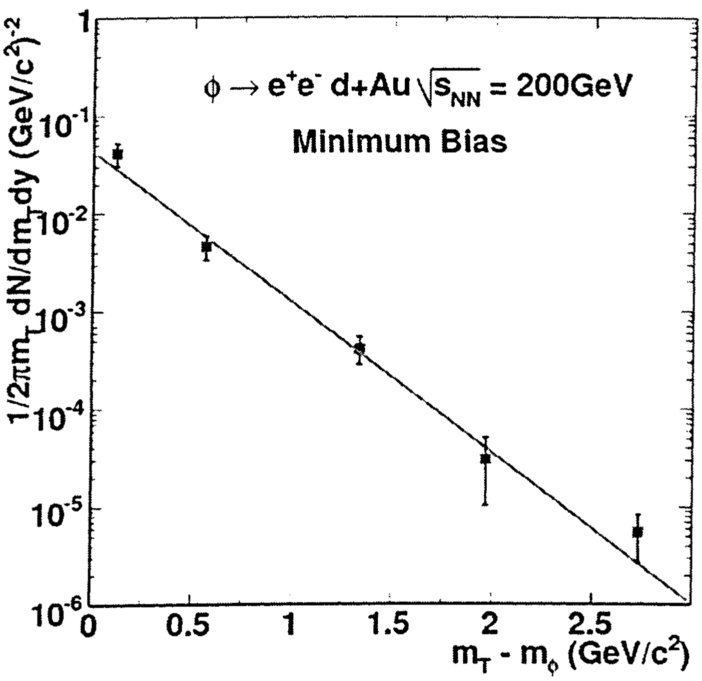

Figure 4.3: m_T spectrum of $\phi \to e^+e^-$ in $d+Au$ collisions. The line represents the fit to the exponential function, Eq. 4.1. Statistical and systematic errors are shown by vertical bars and shaded bands, respectively.

Table 4.4: dN/dy and T from the $\phi \to e^+e^-$ analysis in $d+Au$ collisions.

	Event class	dN/dy	T (MeV)
$\phi \to e^+e^-$ $d+Au$, Run 3	MB	0.099 ± 0.021(stat) ± 0.023(syst)	283 ± 21(stat) ± 16(syst)

4.2.2 $\phi \to e^+e^-$ in $Au+Au$ collisions

The $Au+Au$ data of Run 4 allowed to perform the $\phi \to e^+e^-$ analysis for minimum bias events and two centrality bins 20-40% and 40-92.2%. The m_T spectra are shown in Fig. 4.4. Each spectrum is fitted with the exponential function of Eq. 4.1 and the yields and temperatures extracted from the fit are summarized in Table 4.5. Table 4.5 also includes the value of dN/dy and T for the most central bin 0-20% obtained using the integral yield method as explained in Section 3.7.

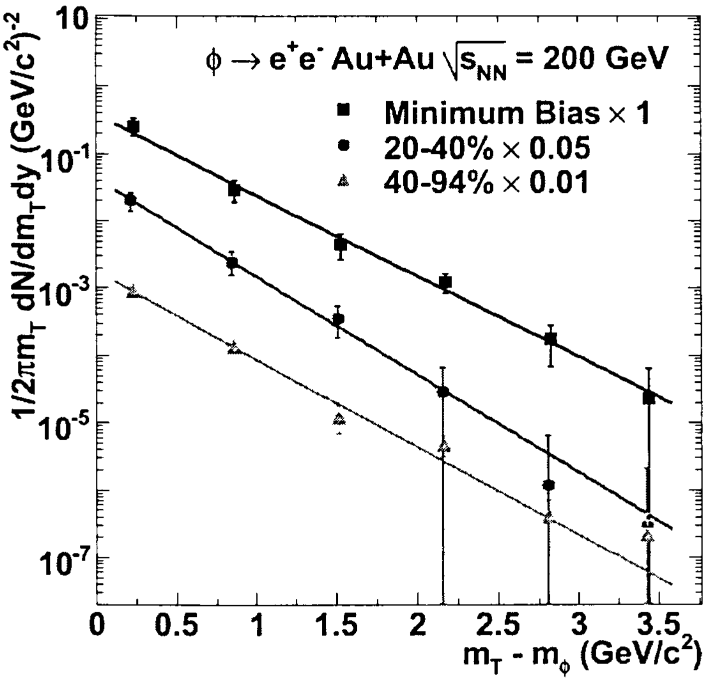

Figure 4.4: m_T spectra of $\phi \rightarrow e^+e^-$ for minimum bias events and two centrality classes in $Au+Au$ collisions. The lines represent the fit to the exponential function, Eq. 4.1. The spectra are scaled by the indicated factors for clarity. Statistical and systematic errors are shown by vertical bars and shaded bands, respectively.

Table 4.5: Summary of dN/dy and T from the $\phi \rightarrow e^+e^-$ analysis in $Au+Au$ collisions.

	Event class	dN/dy	T (MeV)
$\phi \rightarrow e^+e^-$ $Au+Au$, Run 4	MB	1.21 ± 0.319stat) ± 0.46(syst)	361 ± 30(stat) ± 29(syst)
	0-20%	3.97 ± 1.70(stat) ± 1.71(syst)	fixed at 366 (see text)
	20-40%	2.16 ± 0.51(stat) ± 0.55(syst)	298 ± 29(stat) ± 14(syst)
	40-92.2%	0.51 ± 0.07(stat) ± 0.08(syst)	323 ± 22(stat) ± 3(syst)

4.2.3 $\phi \rightarrow K^+K^-$ in $Au+Au$ collisions

The $\phi \rightarrow K^+K^-$ analysis is performed using kaons identified in the TOF, EMC_{EAST} and EMC_{WEST} detectors. These detectors have different acceptances and identification capabilities (see Section 2.2.3). Therefore the analyses for the different detector combinations are performed separately and combined at the final stage to derive physical results.

4.2.3.1 $\phi \rightarrow K^+K^-$ using TOF-TOF detector combination

Using the TOF-TOF data of Run 4, the rapidity densities, dN/dy, and inverse slopes, T, are derived for minimum bias events and five centrality classes. The m_T spectra for these classes fitted with the exponential function of Eq. 4.1 and scaled for clarity are shown in Fig. 4.5. The extracted values of dN/dy and T are summarized in Table 4.6.

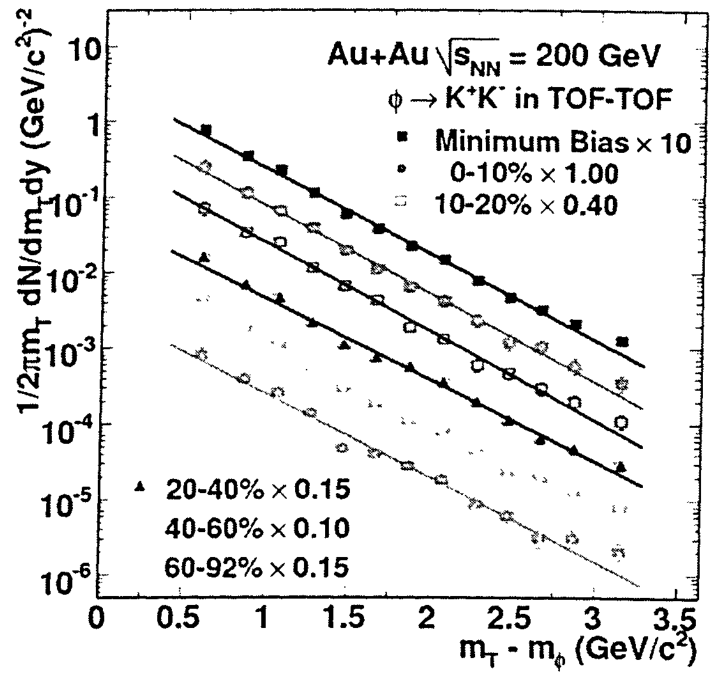

Figure 4.5: $\phi \rightarrow K^+K^-$ m_T spectra measured with the TOF-TOF detector combination. The spectra are scaled for clarity by the scale factors as indicated. The lines represent the fit to the exponential function, Eq. 4.1. Statistical and systematic errors are shown by vertical bars and shaded bands, respectively.

4.2.3.2 Consistency check between the $\phi \rightarrow K^+K^-$ analyses for different subsystem combinations

As mentioned above the final $\phi \rightarrow K^+K^-$ analysis is performed using kaons identified in the TOF, EMC$_{EAST}$ and EMC$_{WEST}$ detectors. The consistency of the measurements for the different subsystem combinations is demonstrated by comparing the m_T spectra derived separately for each detector combination.

Fig. 4.6 shows the minimum bias transverse mass spectra for the four detector combinations: TOF-TOF, TOF-EMC$_{EAST}$, EMC$_{EAST}$-EMC$_{EAST}$ and EMC$_{WEST}$-EMC$_{WEST}$.

Table 4.6: dN/dy and T from the $\phi \rightarrow K^+K^-$ analysis in $Au+Au$ collisions using the TOF detector.

	Event class	dN/dy	T (MeV)
$\phi \rightarrow K^+K^-$ TOF-TOF $Au+Au$, Run 4	MB	1.06 ± 0.06(stat) ± 0.17(syst)	382 ± 7(stat) ± 23(syst)
	0-10%	3.55 ± 0.38(stat) ± 0.67(syst)	373 ± 11(stat) ± 34(syst)
	10-20%	2.94 ± 0.25(stat) ± 0.47(syst)	369 ± 8(stat) ± 26(syst)
	20-40%	1.23 ± 0.10(stat) ± 0.18(syst)	403 ± 9(stat) ± 16(syst)
	40-60%	0.51 ± 0.05(stat) ± 0.08(syst)	391 ± 11(stat) ± 12(syst)
	60-92%	0.07 ± 0.01(stat) ± 0.01(syst)	392 ± 15(stat) ± 8(syst)

The m_T spectra are scaled for clarity. The lines represent the fit to the exponential function, Eq. 4.1 with a slope parameter fixed to T = 388 MeV as given by the fit of the combined minimum bias spectrum (see Table 4.8). Fig. 4.6 illustrates the difference in the momentum covered by each subsystem combinations. All combinations that includes EMCal allow us to access the low-m_T bin while the TOF-TOF combination has the largest reach in m_T up to ≈ 3.5 GeV/c^2 .

The dN/dy and T values extracted from the fit of the individual spectra to the exponential function, Eq. 4.1, are listed in Table 4.7. Fig. 4.6 and Table 4.7 demonstrate very good consistency among the different subsystem measurements.

Table 4.7: dN/dy and T from the $\phi \rightarrow K^+K^-$ analysis in $Au+Au$ collisions for minimum bias events measured by the different subsystem combinations.

Subsystem	TOF-TOF	TOF-EMC$_{EAST}$	EMC$_{EAST}$-EMC$_{EAST}$	EMC$_{WEST}$-EMC$_{WEST}$
dN/dy	1.06 ± 0.06	1.02 ± 0.08	0.97 ± 0.10	1.17 ± 0.13
T, (MeV)	382 ± 7	363 ± 19	325 ± 26	324 ± 27

4.2.3.3 $\phi \rightarrow K^+K^-$ using all detector combinations

Fig. 4.7 shows the m_T spectra of ϕ mesons for minimum bias events and seven centrality classes in the $\phi \rightarrow K^+K^-$ analysis in $Au+Au$ collisions using all detector combinations. Each spectrum is fitted with an m_T-exponential function Eq. 4.1 and the yields and temperatures extracted as fit parameters are summarized in Table 4.8. The combined results are consistent with the results obtained with TOF-TOF detector combination (see Table 4.6).

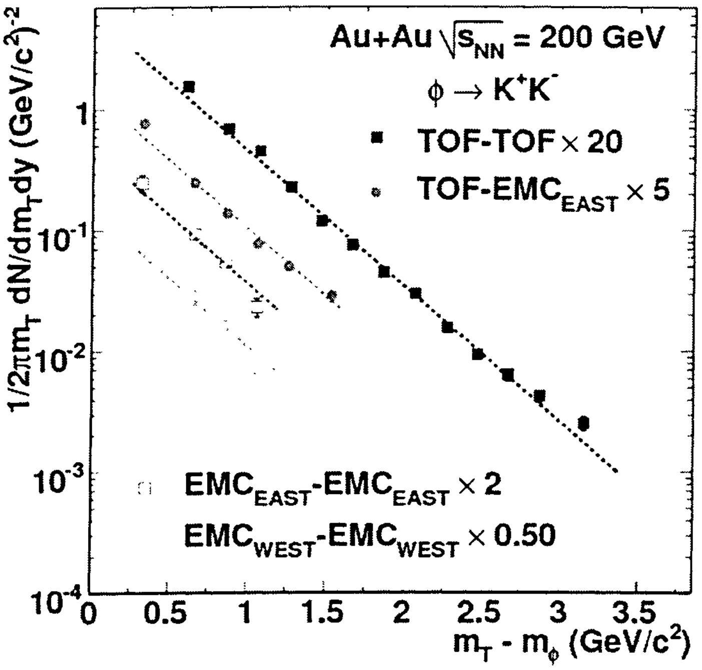

Figure 4.6: $\phi \to K^+K^-$ m_T minimum bias spectra measured by the different PHENIX subsystem combinations. The spectra are scaled for the better visibility with scale factors as indicated. The lines represent the fit to the exponential function, Eq. 4.1 with a slope parameter fixed to T = 388 MeV as given by the fit of the combined minimum bias spectrum.

Table 4.8: Summary of dN/dy and T for the $\phi \to K^+K^-$ analysis in $Au+Au$ collisions.

	Event class	dN/dy	T (MeV)
$\phi \to K^+K^-$ $Au+Au$, Run 4	MB	1.08 ± 0.04(stat) ± 0.20(syst)	388 ± 5(stat) ± 27(syst)
	0-10%	3.80 ± 0.30(stat) ± 0.72(syst)	372 ± 11(stat) ± 26(syst)
	10-20%	2.32 ± 0.16(stat) ± 0.44(syst)	394 ± 10(stat) ± 27(syst)
	20-30%	1.62 ± 0.11(stat) ± 0.31(syst)	397 ± 10(stat) ± 28(syst)
	30-40%	0.95 ± 0.07(stat) ± 0.18(syst)	401 ± 10(stat) ± 28(syst)
	40-50%	0.75 ± 0.04(stat) ± 0.13(syst)	377 ± 8(stat) ± 26(syst)
	50-60%	0.35 ± 0.03(stat) ± 0.06(syst)	392 ± 12(stat) ± 27(syst)
	60-92%	0.11 ± 0.01(stat) ± 0.02(syst)	348 ± 11(stat) ± 24(syst)

4.2.4 Summary: ϕ yield and inverse slope parameter.

The ϕ-meson rapidity density dN/dy, and temperature, T, obtained in the $\phi \to e^+e^-$ and $\phi \to K^+K^-$ analyses in the $Au+Au$ and $d+Au$ collisions at $\sqrt{s_{NN}}$ = 200 GeV are

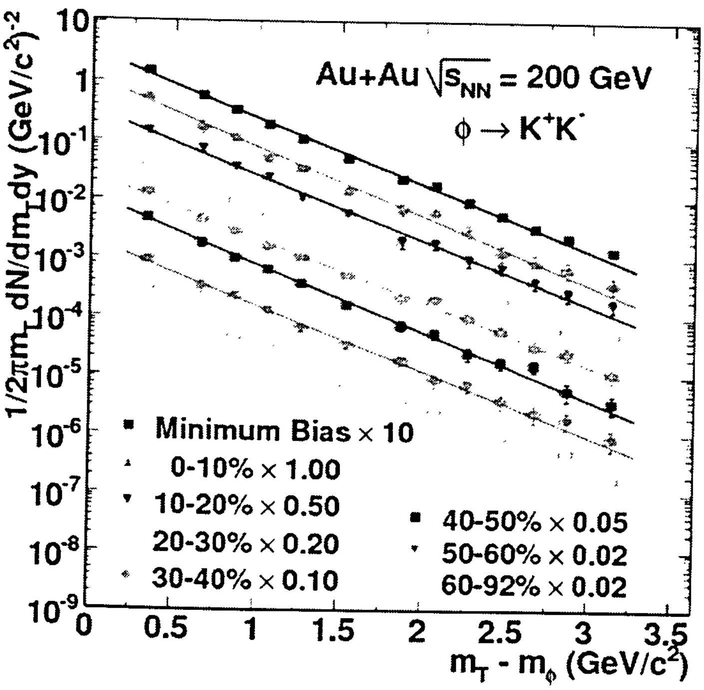

Figure 4.7: m_T spectra of the $\phi \rightarrow K^+K^-$ mesons for minimum bias events and seven centrality classes in $Au+Au$ collisions. Each line represents the fit to the exponential function, Eq. 4.1. The spectra are scaled by the indicated factors for clarity. Statistical and systematic errors are shown by vertical bars and shaded bands, respectively.

summarized in the top and bottom panels of Fig. 4.8, respectively.

The temperatures measured in $Au+Au$ collisions trough e^+e^- and K^+K^- decay channels (see bottom panel of Fig. 4.8) are centrality independent and in agreement within statistical and systematic uncertainties. In $d+Au$ collisions the temperature measurements via the e^+e^- decay channel are in agreement within error bars with the temperatures measured in peripheral $Au+Au$ collisions via the e^+e^- and K^+K^- decay channels.

The yields obtained in the two decay channels, their centrality dependence and comparison to the results obtained at lower energies at the AGS and SPS will be discussed below. Also we will discuss the ϕ-meson line shape properties and ϕ/π and ϕ/K ratios compared to those at the AGS and SPS energies.

4.3 Line-shape analysis

The large statistics of ϕ mesons measured through the K^+K^- decay channel in the Run 4 $Au+Au$ collisions and the good S/B ratio allow us to perform study of the ϕ-meson

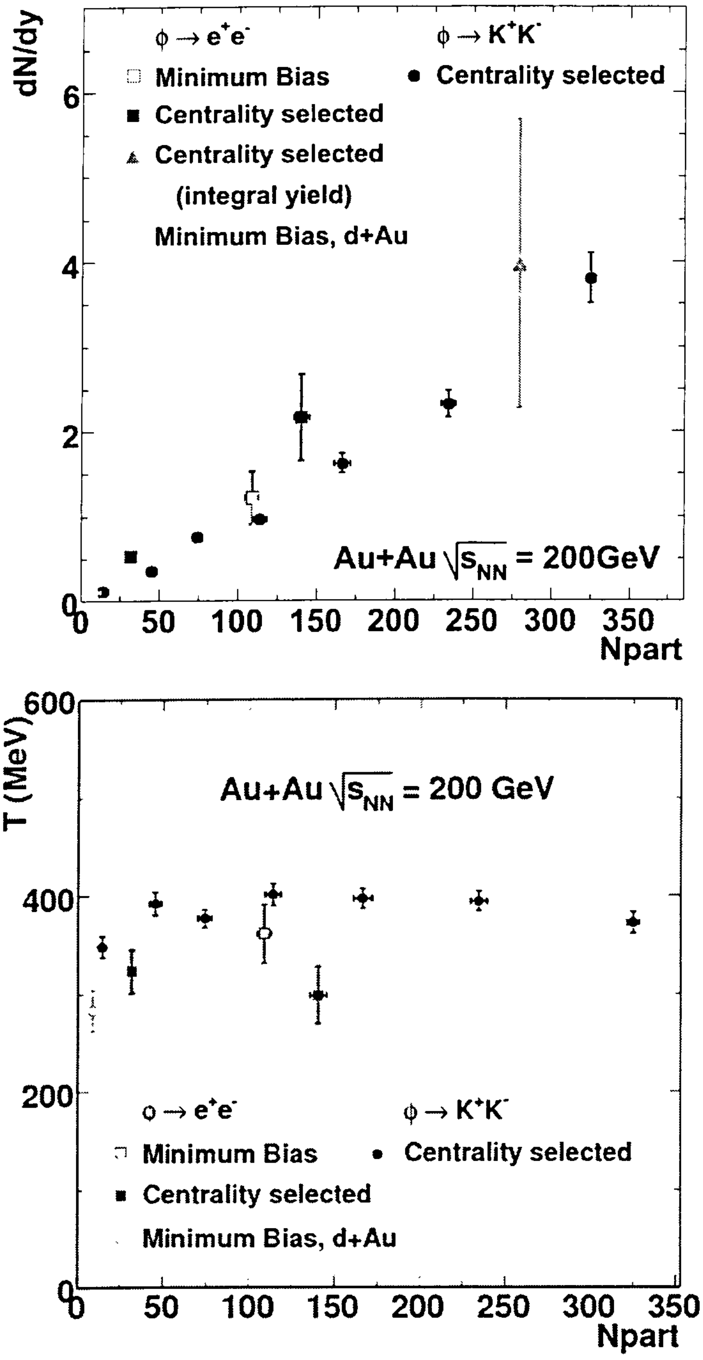

Figure 4.8: Multiplicity dependence of the ϕ meson rapidity density, dN/dy, (top panel) and temperature, T, (bottom panel) for e^+e^- and K^+K^- decay channels. Open and filled symbols represent MB and centrality selected events, respectively. The triangle shows the ϕ yield derived from the integral yield using the global correction factor, see Section 3.6. Statistical and systematic errors are shown by vertical bars and shaded bands, respectively.

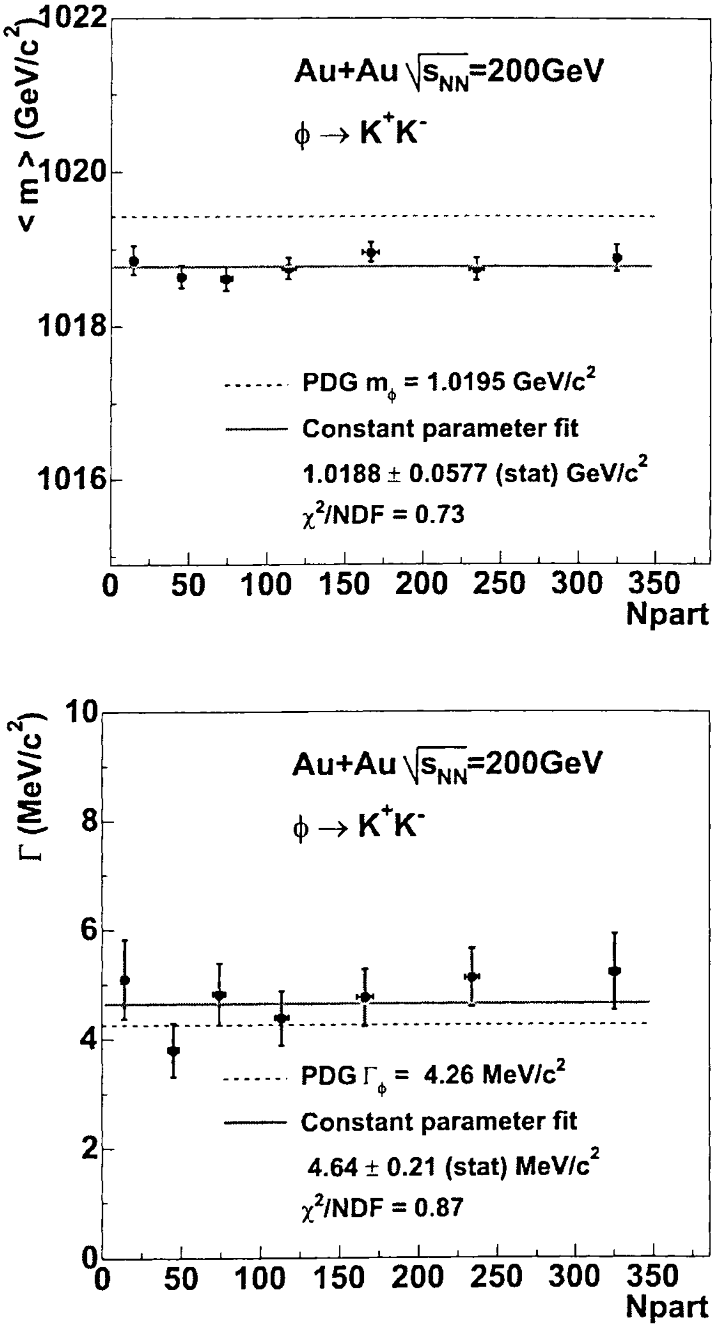

Figure 4.9: Centrality dependence of the ϕ meson line-shape - centroid of the mass peak (top panel) and natural width (bottom panel) - measured in the $\phi \to K^+K^-$ decay channel for TOF-TOF combination.

line-shape properties for minimum bias and several centrality classes. A similar analysis through the dielectron decay channel in $Au+Au$ collisions is not possible in the present PHENIX configuration due to the large combinatorial background and the subsequent large statistical uncertainties. Therefore the line-shape analysis presented in this thesis is restricted to the K^+K^- decay channel only. For each centrality bin the signal mass spectrum is fitted with the relativistic Breit-Wigner function Eq. 3.7 convoluted with a Gaussian function to account for the experimental mass resolution of 1.2 MeV/c^2 (see an example on top panel of Fig. 4.10).

The centrality dependence of the fitted centroids and natural widths, Γ, measured using the TOF-TOF detector combination are shown on the top and bottom panels of Fig. 4.9, respectively. The main source of systematic errors, shown by the two continuous lines on the top panel and by the shaded boxes on the bottom panel (indicating the $\pm$ 1σ boundaries of systematic errors), are the uncertainties in the momentum scale and the combinatorial-background normalization procedure. The present measurements show that with an accuracy better than 1 MeV/c^2, the ϕ meson centroid and width are independent of centrality and consistent with the PDG values.

The excellent accuracy of the measurements rules out possible modifications of the ϕ-meson line shape in the K^+K^- decay channel similar to what was observed by the E325 experiment [43] in the e^+e^- decay channel (see Section 1.4). The top panel of Fig. 4.10 shows the $\phi \rightarrow K^+K^-$ invariant mass spectrum for low-momentum K^+K^- pairs ($m_T < 2$ GeV/c^2) and the bottom panel shows the $\phi \rightarrow e^+e^-$ spectrum measured by the E325 experiment. The tail is clearly observed at KEK while it is not present in the measurements performed by PHENIX. It should be emphasized that although in the K^+K^- decay channel there is no acceptance at invariant mass below 0.98 GeV/c^2 the modifications of the line-shape similar to those observed at KEK should be seen by PHENIX with its excellent mass resolution.

The simultaneous measurement of the ϕ meson production via the e^+e^- and K^+K^- decay channels may perhaps indicate an intriguing increase of the yield in the dielectron channel with respect to the kaon one which could be related to the restoration of chiral symmetry. Since hadrons are affected by strong interactions the rescattering of the daughter kaons in the nuclear medium may effectively decrease the ϕ meson yield measured via the K^+K^- decay channel [75]. However this phenomenon should also affect the reconstructed invariant mass distribution and reveal itself in changes of the ϕ meson line-shape [75] which are not observed in the data.

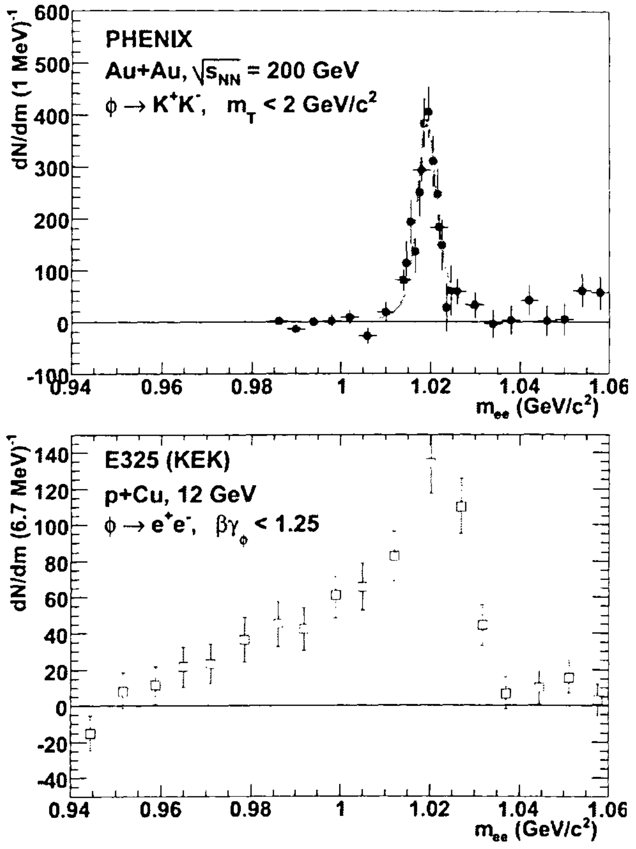

Figure 4.10: The subtracted invariant mass spectra of low momentum K^+K^- pairs measured by the PHENIX experiment (top panel) and of low momentum e^+e^- pairs measured by the E325 experiment at KEK PS [43] (bottom panel). The line represent the fit with the relativistic Breit-Wigner function convoluted with experimental mass resolution (see Section 3.5.2).

The present line-shape analysis rules out any deviations of the extracted ϕ meson mass centroid and width from the PDG values with a precision of 1 MeV/c^2. This result presumably excludes hadronic rescattering as a possible mechanism of the ϕ meson yield difference in the K^+K^- decay channel compared to the e^+e^- channel, observed in the present work (albeit with very large error bars).

4.4 Discussion

4.4.1 Centrality dependence, hadronic *vs.* leptonic decay channels

The rapidity density and temperature of the ϕ meson measured for different centralities is an important tool to study the system properties as function of its size.

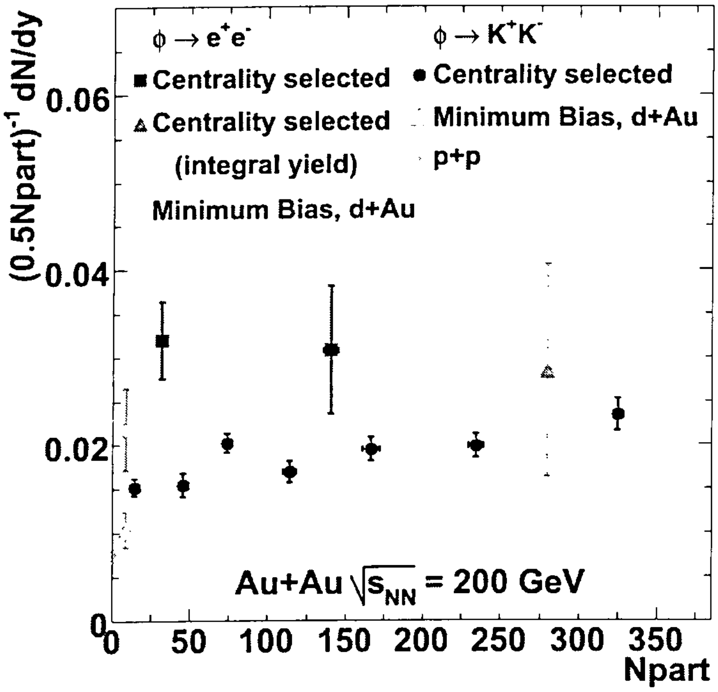

Figure 4.11: Multiplicity dependence of the ϕ meson rapidity density normalized to number of participant pairs, $(0.5 \cdot N_{part})^{-1}\ dN/dy$ for e^+e^- and K^+K^- decay channels. Open and filled symbols represent MB and centrality selected events, respectively. The triangle shows the ϕ yield derived from the integral yield using the global correction factor, see Section 3.6. Statistical and systematic errors are shown by vertical bars and shaded bands, respectively.

The rapidity densities, dN/dy, measured in the e^+e^- and K^+K^- decay channels (top panel of Fig. 4.8) are increasing functions of the number of participants N_{part}. To take into account the system size it is convenient to normalize the yield to the number of participant pairs, $dN/dy_{norm} = (0.5 \cdot N_{part})^{-1}\ dN/dy$. Fig. 4.11 shows the centrality dependence of the normalized ϕ yield, dN/dy_{norm}, for the e^+e^- and K^+K^- decay channels. The figure shows also the normalized yield from the $\phi \rightarrow K^+K^-$ analyses in $d+Au$ [76] are $p+p$ [77] collisions. In the K^+K^- decay channel the ϕ yield per participant pair shows a sharp increase with N_{part} for the light systems and a slow increase of $\sim$ 30% as one goes from peripheral to central $Au+Au$ collisions. A similar increase with N_{part} from peripheral to central $Au+Au$ collisions was also observed for $\pi^{\pm}$ and $K^{\pm}$ [78] as reflected by the flatness of the ϕ/π and ϕ/K ratios *vs.* centrality shown by solid circles in Fig. 4.12. Similarly to the K^+K^- decay channel, the measurements in the e^+e^- channel show an increase of the normalized yield from $d+Au$ collisions to peripheral $Au+Au$ collisions. The shape of the centrality dependence seems also to be consistent in the two channels within their statistical and systematic uncertainties.

The ϕ production in $Au+Au$ collisions at $\sqrt{s_{NN}}$ = 200 GeV was also studied by the STAR collaboration [80]. The centrality dependence of the ϕ meson rapidity density and inverse slope are consistent with PHENIX results. However the absolute yields extracted by STAR is systematically larger than those measured by PHENIX in the same decay channel.

As discussed in Section 1.3.3 various models predict sizable changes in the ϕ meson mass and/or width which could manifest themselves in dramatic changes of the branching ratios of the ϕ meson decay via the leptonic and hadronic channels. The comparison shown in Fig. 4.11 hints at a difference in the ϕ meson yield derived from the K^+K^- and the e^+e^- decay channels that could signal such in-medium modifications of the two branching ratios. However, the experimental errors are too large and a more definite statement about this difference cannot be made with the present data set and with the present capabilities of the PHENIX detector. To quantify a possible difference between the two channels, a chi-square analysis was performed in the $Au+Au$ results that shows that there is a non-negligible probability of about 20% for the two data sets to be consistent with each other. The large error bars both statistical and systematic in the dielectron channel prevent us from making detailed comparisons with theoretical models. (A dramatic improvement in the performance of the PHENIX detector in the low-mass dielectron sector is expected with the Hadron Blind Detector upgrade which will be discussed in Chapter 5.) Also results from the reference measurement of the ϕ-meson production in $p+p$ collisions through the dielectron decay channel, crucial to establish a baseline for the nuclear case are not yet available. All these reasons prevent us from making detailed comparisons with theoretical models.

4.4.2 Comparison of the ϕ production to pions and kaons at different colliding energies and species

The ratios of the hadron yields having a different quark content carry an important information about the chemical properties of the system. In particular, the ratios of the ϕ

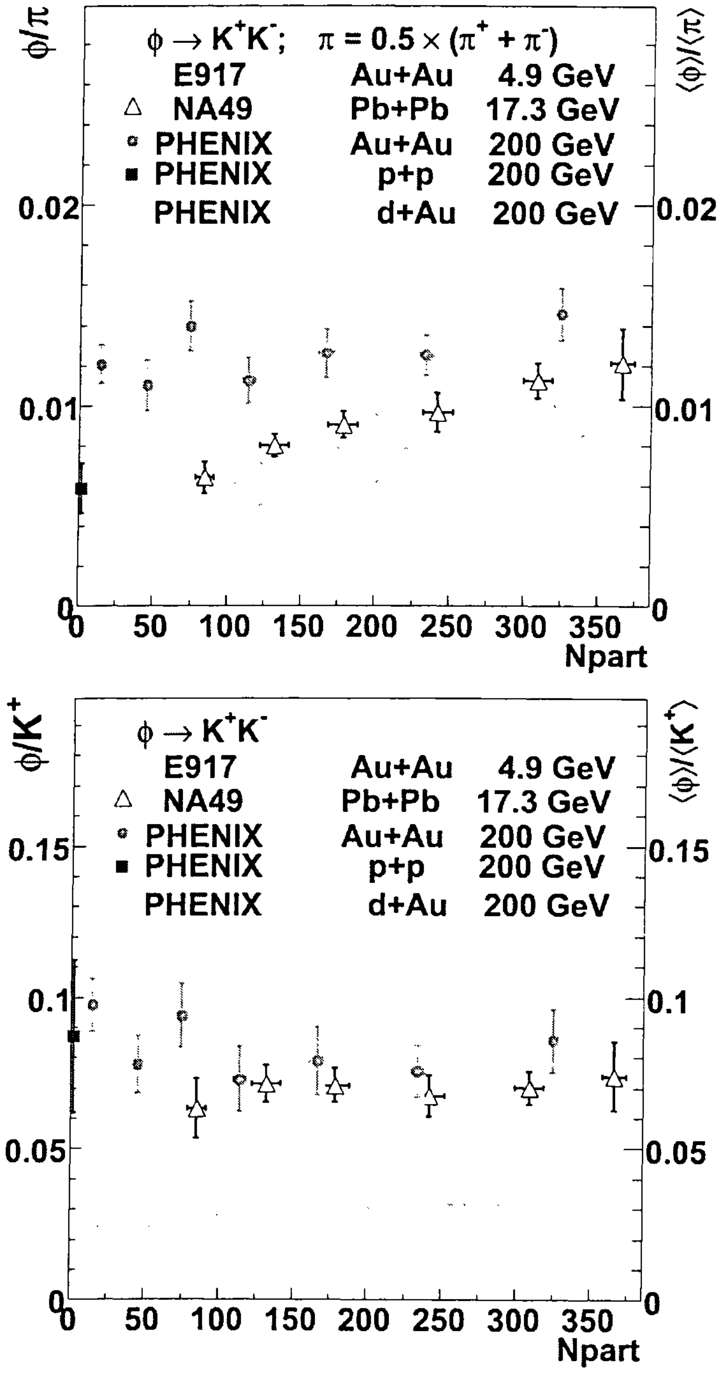

Figure 4.12: The centrality dependence of ϕ/π(top panel) and ϕ/K (bottom panel). The open squares and triangles represent the measurements by the E917 [37] and NA49 [79] experiments, respectively. The ratios obtained at $\sqrt{s_{NN}}$ = 200 GeV in $p+p$, $d+Au$ and $Au+Au$ collisions are shown by filled symbols. Statistical and systematic errors are shown by vertical bars and shaded bands, respectively.

meson to the pion and kaon and their dependence on the system size and collision energy can tell us about the strangeness production in heavy-ion collisions.

The multiplicity dependence of the ϕ-meson rapidity density, inverse slope (see top and bottom panels of Fig. 4.13, respectively) as well as ratios of the ϕ-meson integrated yield to the integrated yields of the pions and kaons (see top and bottom panels of Fig. 4.12, respectively) at lower colliding energies were studied at the AGS ($\sqrt{s_{NN}}$ = 4.9 GeV) [37] and the SPS ($\sqrt{s_{NN}}$ = 17.3 GeV) [41, 42, 79, 81]. Fig. 4.12 shows also the ratio of the ϕ yield to that of the pions and kaons in $p+p$, $d+Au$ collisions at $\sqrt{s_{NN}}$ = 200 GeV measured by the PHENIX experiment [76, 77, 82].

The several observations shall be emphasized:

- The centrality dependence of the normalized ϕ-meson rapidity density is in agreement with measurements performed at SPS (see top panel of Fig. 4.13). The ϕ-meson yield measured at RHIC energy is increased by more than one order of magnitude and by about a factor of two as compared to the AGS and the SPS energies, respectively.

- The inverse slope, T, measured at RHIC is larger by a factor 1.5-2 than the temperatures measured by at the AGS [37] and at the SPS [41, 42, 81] as shown on the bottom panel of Fig. 4.13.

- At RHIC energies the centrality dependence of hidden strangeness (ϕ) production in $Au+Au$ collisions is similar to the production of non-strange particles (π) and particles with open strangeness (kaons) which is reflected in the flat behavior of the ϕ/π and ϕ/K ratios as the function of N_{part} (see Fig. 4.12). The identity in the production of the ϕ and kaons rules out the kaon coalescence as main production channel for the ϕ production. The trend of the ϕ/π ratio measured in $Au+Au$ collisions at RHIC is quite different from lower energy results measured at the AGS and SPS (see top panel of Fig. 4.12).

- The ϕ/π ratio shows the threshold behavior as we go from the collisions of the light systems to the peripheral $Au+Au$ collisions which indicates that the sharp increase seen in the ϕ-meson production (see Fig. 4.11) is not present in the pion production. The strangeness production in the collisions of the light systems is similar to the that measured in $Au+Au$ collisions.

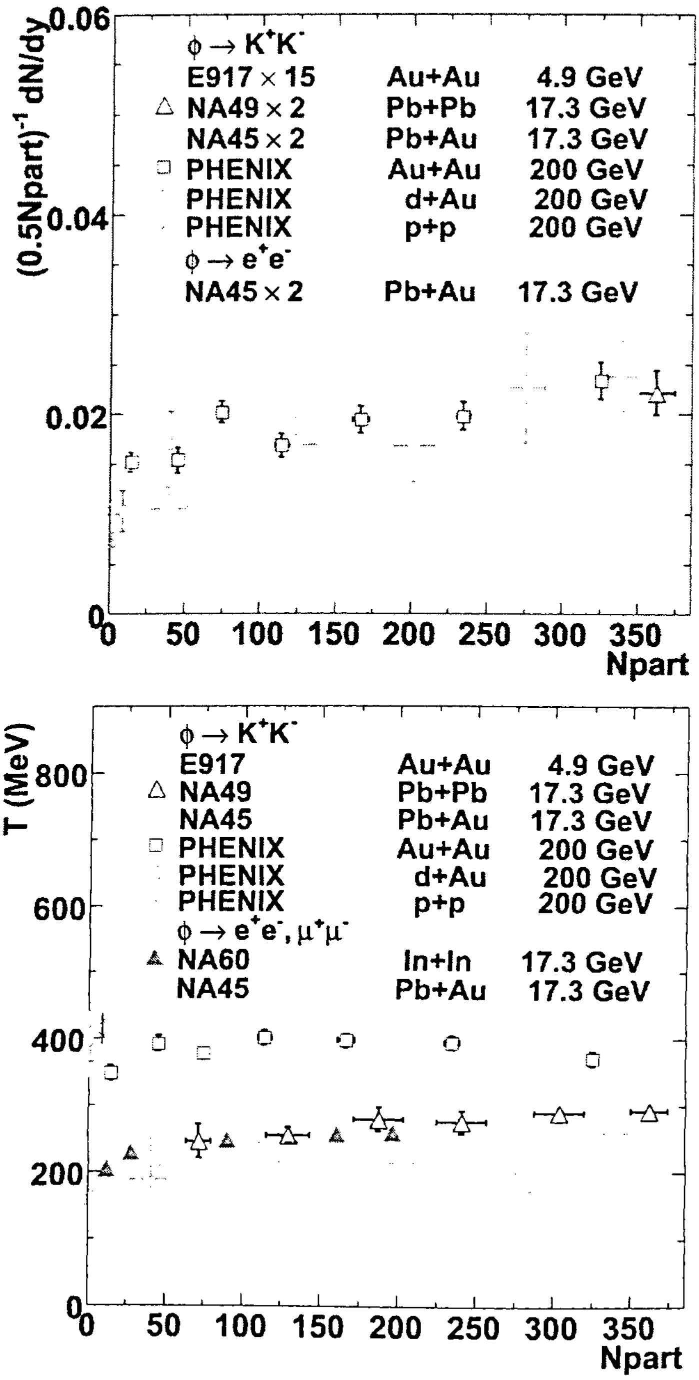

Figure 4.13: Multiplicity dependence of the ϕ meson rapidity density, normalized to number of participant pairs, $(0.5{\cdot}N_{part})^{-1}$ dN/dy (top panel) and the temperature, T, (bottom panel) for e^+e^- (open symbols) and K^+K^- (filled symbols) decay channels at different collision energies. E917 data are from [37], NA49 data are from [81], NA45 data are from [41] and NA60 data are from [42]. Statistical and systematic errors are shown by vertical bars and shaded bands, respectively.

Chapter 5

Hadron Blind Detector

5.1 Motivation for a Hadron Blind Detector

The measurement of electron pairs in heavy-ion collisions is a challenging task. The huge combinatorial background originating from unrecognized γ-conversions and π^0 Dalitz decays limits significantly the capability of the PHENIX detector to measure e^+e^- pairs in the low-mass region. Fig. 5.1 shows the foreground and background determined from the mixed events technique, and the subtracted dielectron invariant mass spectra measured in $Au+Au$ collisions at $\sqrt{s_{NN}} = 200$ GeV [83]. The signal to background ratio at ϕ mass is $\sim$ 1/80, becomes significantly worse in the continuum region, $S/B \sim$ 1/200 at m_{e^+e} ≈ 500 MeV/c^2. With such a small S/B ratio the statistical and systematic errors are dominated by the combinatorial background.

In the framework of my Ph.D. project I was involved in the upgrade of the PHENIX detector with a new device which aims at improving the capability of PHENIX to measure low-mass dielectron pairs. The proposal is a conceptually new Čerenkov detector which is almost blind to all particles except for electrons, *i.e.* a Hadron Blind Detector (HBD). The HBD was developed by our group at the Weizmann Institute. Its construction and installation have been completed detector is presently being commissioned.

The concept of HBD and the results of a comprehensive R&D program to demonstrate the feasibility of the proposed scheme are presented below [84, 85].

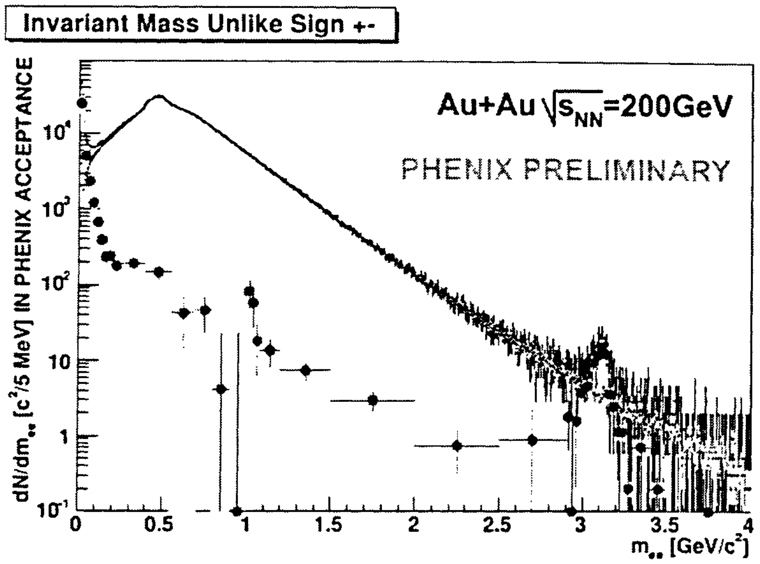

Figure 5.1: The foreground (black), background (red) and subtracted e^+e^- invariant mass spectra measured by PHENIX in $Au+Au$ collisions at $\sqrt{s_{NN}} = 200$ GeV [83]. Statistical and systematic errors are shown by vertical bars and shaded bands, respectively.

5.2 The HBD concept

The PHENIX detector was designed anticipating the feasibility of the measurement of low-mass pairs with an appropriate upgrade. In particular, provision was made for the installation of an inner coil which would create an almost field-free region close to the vertex, extending out to ~ 50-60 cm in the radial direction. In addition to this coil (which was installed in PHENIX for Run 4 in 2004), the major and challenging element of the upgrade is a Hadron Blind Detector located in this field free region. The main task of the HBD is to recognize and reject γ-conversions and π^0 Dalitz decays . The strategy is to exploit the fact that the opening angle of electron pairs from these sources is very small compared to the pairs from the decay of light vector mesons. In the field-free region, this angle is preserved and by applying an opening angle cut one can reject more than 90% of the γ-conversions and π^0 Dalitz decays , while preserving most of the signal [1]. The size of the HBD is constrained by the available field-free region starting outside the beam pipe (at r~5 cm) and ending at the inner coil (at r~60 cm). Fig. 5.2 shows the layout of the

---

[1] The cut is applied at the HBD between an electron track detected both in the central arm and the HBD and a nearby hit in the HBD. This cut therefore removes the single tracks from low-mass pairs which are at the origin of the huge combinatorial background.

inner part of the PHENIX detector together with the location of the coils and the proposed HBD.

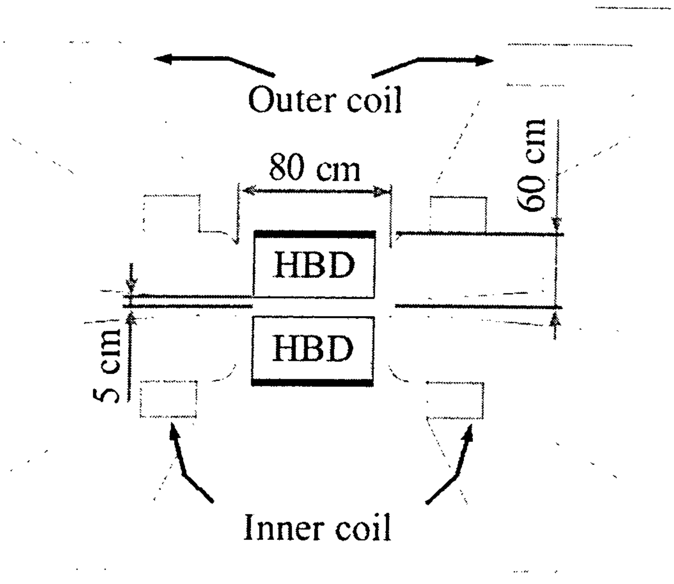

Figure 5.2: Layout of the inner part of the PHENIX detector showing the location of the HBD and the second coil.

The system specifications were determined from conceptual Monte Carlo simulations. In order to reduce the combinatorial background originating from γ-conversions and π^0 Dalitz decays of at least two orders of magnitude HBD should have electron identification with an efficiency $> 90\%$ including double hit recognition; a moderate π rejection factor as low as 100-200. This simulation shows also that is important to have a larger acceptance in the HBD compared to the fiducial central arm acceptance to provide a *veto area* for the rejection of pairs where only one partner is inside the fiducial acceptance [86].

After careful evaluation of the relevant options (the requirements of electron identification, geometrical constraints, radiator gas, window, detector gas, photocathode, amplifying element, readout scheme) the following HBD configuration was proposed: a windowless Čerenkov detector operated in pure CF_4 in a special proximity focus geometry, with a reflective CsI photocathode and a triple Gas Electron Multiplier (GEM) [87] detector element with pad readout.

In this configuration, Čerenkov photons from an electron passing through the radiator are directly collected on the CsI photocathode evaporated onto the first GEM forming a circular blob and not a ring as in a RICH detector.

This scheme exhibits a number of very attractive features:

- The choice of CF_4 both as radiator and detector gas in a windowless geometry results in a very large bandwidth (from $\sim 6\ eV$, given by the threshold of CsI, to $\sim 11.5\ eV$ given by the CF_4 cut-off) and consequently in a very large figure of merit, N_0 which is estimated in [86] to be close to 822 cm^{-1}. With these numbers, the number of photoelectrons, N_{pe}, is expected to be of the order of 36 for a 50 cm long radiator [86]. This large value of N_{pe} ensures a very high electron efficiency and makes it possible to achieve a double-hit recognition larger than 90%.

- Another important advantage of the detector scheme is that it allows the use a photocathode in a reflective mode: the CsI layer covers the top face of the first GEM and the photoelectrons are pulled into the holes of the GEM by their strong electric field. Consequently, the photocathode is totally screened from photons produced in the avalanche process.

- The readout scheme foresees the detection of the Čerenkov photoelectrons in a pad plane with hexagonal pads of size slightly smaller than the blob size ($\sim 10\ cm^2$) such that an electron entering the HBD will produce with very large probability a multiple pad hit, whereas a hadron will produce a single pad hit.

- Since the photoelectrons produced by a single electron will be distributed between at most three pads, one can expect a primary charge of at least 10 electrons/pad, allowing operation of the detector at a relatively moderate gain of a few times 10^3. This is a crucial advantage for the stable operation of a UV-photon detector.

5.3 HBD R&D project

The proposed HBD scheme is very attractive. However, it relies on a new concept and exploits new elements raising a number of questions which required a dedicated investigation in the laboratory. In the framework of the HBD R&D project the following questions have been addressed:

- *Feasibility of the proposed HBD configuration.* First, pure CF_4 has never been used as a detector gas. Therefore stable operation of a triple GEM detector with a CsI layer in pure CF_4 environment at the desired gain of 10^4 needed to be demonstrated. Second, the CsI quantum efficiency in the expected operational bandwidth had to be determined since no data existed beyond 8.5 eV. Finally, the "blindness" of the HBD to hadrons needed to be demonstrated.

- *Aging effects of the GEM foils and CsI photocathode and ion-back flow.* In view of the well known reactivity of CF_4 and its derivatives with water it was necessary to study aging effects of the GEM foils and the CsI photocathode for long term operation in the presence of a large flux of heavily ionizing particles. The flow of positive ions to the CsI layer is one of potential damaging factors that could cause aging of the photocathode and needed to be studied.

asdasfdasdfasfasfddsfgsdgfsdg

5.3.1 Setup and experimental conditions.

For all the measurements we used GEMs produced at CERN with 50 μm kapton thickness, 5 μm thick copper layers, 60-80 μm diameter holes and 140 μm pitch. The GEMs had 3×3 or 10×10 cm^2 sensitive areas. These two types of GEMs will be referred to in the text as "small" and "large", respectively. Three GEMs and one mesh were assembled on FR4 frames in one stack within general 1.5 mm distance between adjacent elements as shown in Fig. 5.3. The top side of some of the large GEMs was divided into four segments (100×25 mm^2 each) to reduce the capacitance and will be referred to in the text as "segmented".

Two gases were used for the measurements: a premixed Ar/CO_2 (70/30%) with Ar of 99.999% purity and CO_2 of 99.998% purity and CF_4 with the purity of 99.999%. In the following the gap between the mesh and top GEM is referred to as "drift"-gap, the gaps between GEMs are called "transfer" and the gap between GEM3 and the printed circuit board (PCB) is called "induction". The corresponding electric fields are E_D, E_T, and E_I.

The detector assembly (drift mesh, triple-GEM, and PCB) was mounted in a stainless steel box that could be pumped down to 10^{-6} Torr and was connected to inlet and outlet gas lines to allow gas flushing. All measurements were done at atmospheric pressure with an overpressure of 0.5 Torr in the detector vessel. The system contained also devices for the precise measurement of temperature, pressure, water and oxygen content down to the ppm level.

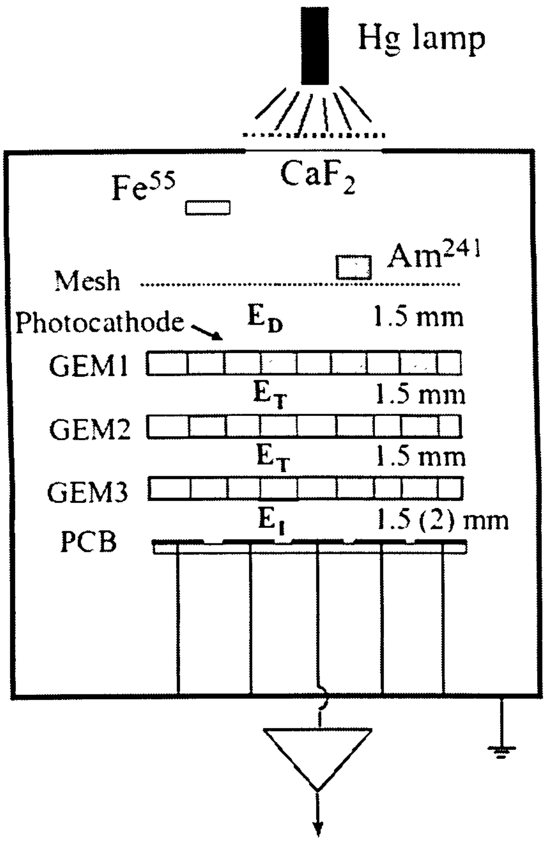

Figure 5.3: Setup of the triple GEM detector. The Hg lamp, ^{55}Fe and ^{241}Am sources were used for measurements with UV-photons, X-rays and α-particles , respectively. The two values for R1 and E_I are explained in the text.

In these studies a Hg UV-lamp, 5.9 keV X-rays from an ^{55}Fe source and 5.5 MeV α-particles from an ^{241}Am source were utilized. The ^{55}Fe source was positioned on a moving arm inside the box at a distance of $\sim$ 40 mm from the mesh and could be moved out of the sensitive volume. The total rate of X-rays was kept at the level of 1 kHz. The 5.9 keV photons from ^{55}Fe release on the average 210 electrons in Ar/CO_2 (26 *eV* per electron-ion pair) and 110 electrons in CF_4 (54 *eV* per electron-ion pair). The ^{241}Am source that emits 5.5 *MeV* α-particles was used to study the discharge limit in the presence of heavily ionizing particles. The source was attached to a moving arm that could be inserted at a distance of 1 mm from the drift mesh and was strongly collimated in order to provide high energy deposition and small energy dispersion in the drift gap. The rate of the α-particles varied between 100 - 300 Hz. Assuming perpendicular incidence of the α-particles to the drift gap, the energy deposition in a 3 mm gas layer is estimated to

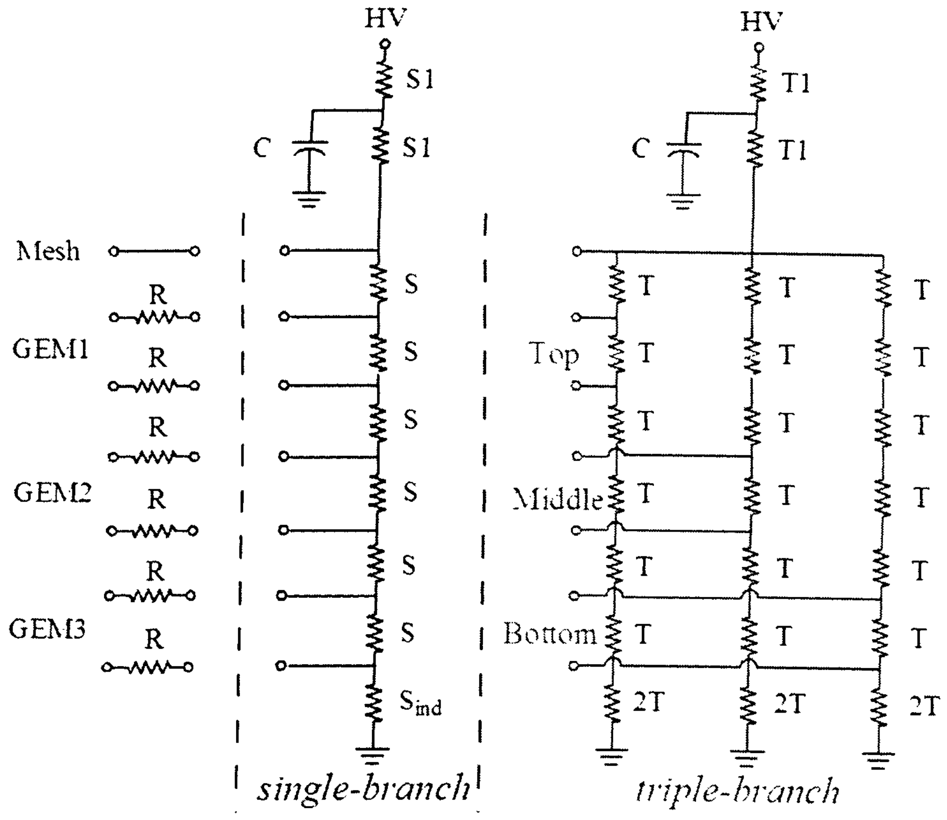

Figure 5.4: *Single-* and *triple-branch* resistor chains. The two values for R and, S, T and E_I are explained in the text.

be $\sim$ 1.1 MeV for CF_4 and $\sim$0.30 MeV for Ar/CO_2 , producing $\sim$2 0,000 and $\sim$ 12,000 primary charges, respectively.

Powering scheme The PCB consisted of 5 stripes of 100×20 mm^2 each or of 9 square pads of size 33×33 mm^2. The stripes or pads were connected either to a charge sensitive preamplifier and shaper or to a picoammeter, depending on the particular measurement. Initially, the high voltage was supplied to the GEM electrodes via a *single-branch* resistor chain as shown in Fig. 5.4. In this case a discharge in one of the GEMs leads to an increase of the voltages across the other two GEMs that can cause multiple discharges and damage to the GEMs. To avoid that we used a *triple-branch* resistor chain with three independent resistive dividers as shown in Fig. 5.4. The resistors T are 5.6 MΩ, T1 and T2 are 1.2 MΩ. For the segmented GEMs, the resistors R are connected directly to each segment and located inside the detector box. To ensure an almost 100% electron collection efficiency to the PCB, the induction field E_I is set to twice the transfer field E_T

by using a $2T$ resistor between the bottom GEM and the PCB [84]. For the measurements where the drift field was varied, two HV power supplies were used, one for the mesh and one for the three GEMs.

The photocathode was prepared by evaporating a $\sim$ 2000 Å thick layer of CsI on the first GEM, previously coated with thin layers of Ni and Au to avoid chemical reaction with the CsI film. The measurements with the CsI reflective photocathode were performed with a Hg lamp positioned outside the detector, close to and a UV-transparent window (CaF_2) with an absorber that reduced the UV-flux by a factor of 1000 times to avoid possible damage to the photocathode [88]. The illuminated area of the detector was about 100 mm^2. In this geometry, the measured photo-electron current was about 2×10^5 e/mm^2 $\times$s. The measured quantum efficiency of the CsI photocathode was $\sim$ 10% at 185 nm.

The study of the gain limits required a reliable way to monitor discharges in the triple GEM assembly via the resistive chain. The chain was biased by a CAEN-126 HV-power supply. This module includes protection against over-current with a precision of 0.1 μA. The current in the resistive chain was in the range between 250 and 300 μA. and the protection threshold was always kept at 1 μA above the normal value. This was enough to cause a trip when a discharge occurred in a GEM. The trip signal was reset after 1 second and was also counted by a scaler.

5.4 HBD R&D results

5.4.1 Gain in Ar/CO_2 and CF_4

The gain as a function of the voltage across the GEM (ΔV_{GEM}) was measured for both Ar/CO_2 and pure CF_4. The absolute gas gain was determined from the measurements of the signal from ^{55}Fe 5.9 keV X-ray photons. An example of the pulse height distributions for both gases measured at a gain 10^4 is shown in Fig. 5.5. The main peak in Ar/CO_2 is well separated from the escape peak of Ar. The energy resolution is $\sim$ 22% and 38 % for Ar/CO_2 and CF_4, respectively.

The gain was calculated, using the measured relationship between the output signal from the amplifier and the input charge to a calibration capacitor and taking into account the average charge produced by one 5.9 keV photon.

Fig. 5.6 shows the typical gain curves measured with 5.9 keV X-rays in Ar/CO_2 and CF_4 using small and large GEMs. Several detector sets were used and good reproducibility between the various sets was observed. Comparing the data for Ar/CO_2 and CF_4 in

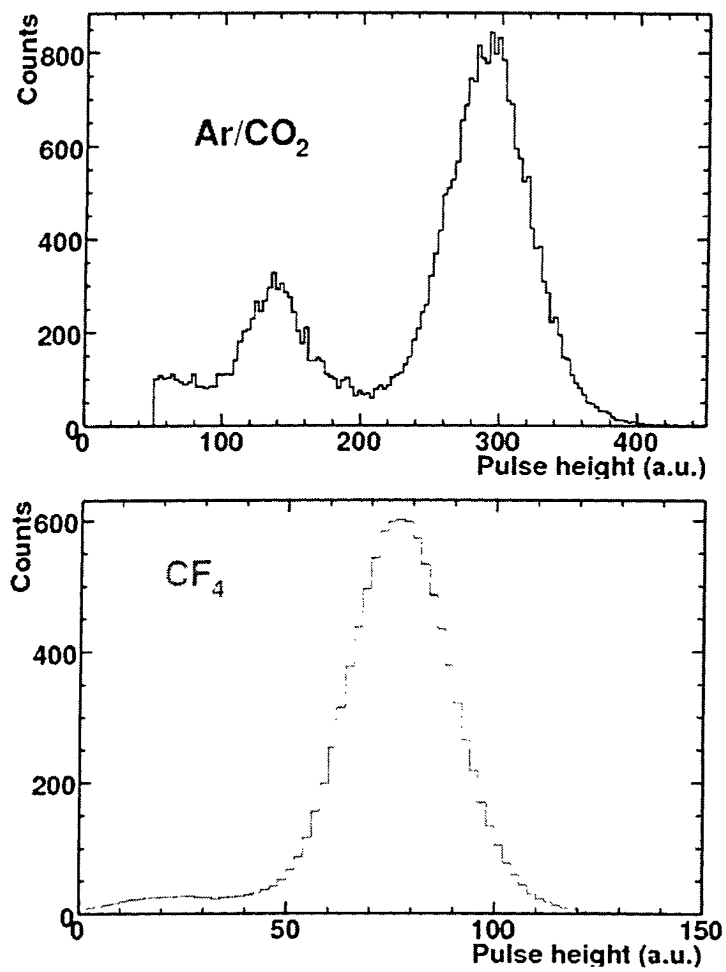

Figure 5.5: Pulse height spectrum of ^{55}Fe X-rays with Ar/CO$_2$ (top panel) and CF$_4$ (bottom panel)

Fig. 5.6 one can see that the operational voltage for CF$_4$ is $\sim$ 140 V higher but the slopes of the gain-voltage characteristics are similar for both gases, *i.e.* an increase of 20 V in ΔV_{GEM} causes an increase of the gain by a factor of $\sim$ 3. The gain in CF$_4$ can reach values above 10^5, in spite of the very high operational voltage.

5.4.2 Discharge probability and saturation effect

Stability of operation and absence of discharges in the presence of heavily ionizing particles is crucial for the operation of the HBD. Due to the large amount of energy stored in the large capacitance of the GEM the measurements of the discharge probability and the

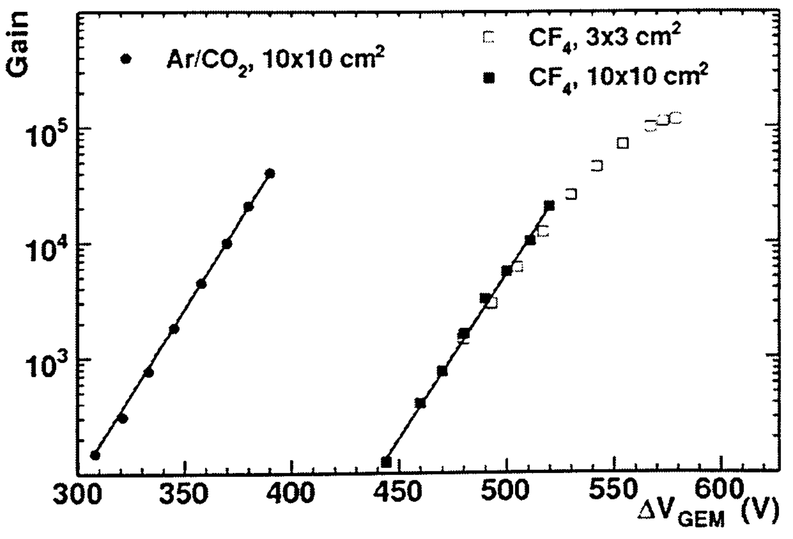

Figure 5.6: Gain as a function the voltage across the GEM measured with the ^{55}Fe X-ray source. The 3×3 cm^2 detector had a CsI layer deposited on the top face of GEM1. The lines represent exponential fits to the data with 10×10 cm^2 GEMs.

discharge limits could not be done with large GEMs since the first spark usually destroys one of the GEMs. Therefore these measurements were performed with small GEMs with a single branch resistor chain [84] and repeated with segmented GEMs with a triple branch resistor chain [85]. In both cases the ^{241}Am source was used to simulate heavily ionizing particles under laboratory conditions.

An interesting feature of CF$_4$ which can already be seen in Fig. 5.6 is the strong deviation from exponential growth at high gains. This "non-linearity" is much more pronounced when the detector is irradiated with ^{241}Am α-particles as shown in Fig. 5.7. The figure shows the total charge in the avalanche measured with a preamplifier (dots). Since at high values of the charge, when the preamplifier is close to saturation, the output signal is already reduced compared to its real value, the measurements were repeated without any pre-amplifier, with the central pad directly connected to the 1 MΩ input of an oscilloscope through a 1 m coaxial cable. In this case the pulse height observed at the scope is determined by the ratio of the charge induced in the pad and the total capacitance of the pad including the capacitance of the cable. The measurements without pre-amplifier are also shown in Fig. 5.7. Both measurements were performed under identical conditions and for this purpose the pre-amplifier was calibrated in units of input charge. In order to obtain the relation between the signal measured without pre-amplifier and the input charge the results were normalized in the range of ΔV_{GEM} = 420 - 440 V where both measure-

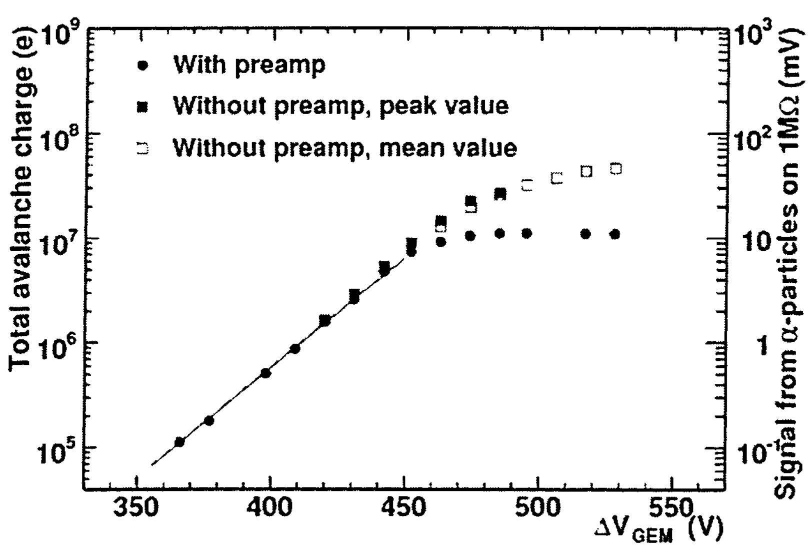

Figure 5.7: Pulse height of the signal from α-particles measured with and without preamplifier as a function of GEM voltage. For the measurement with the preamplifier only mean values are plotted. For the measurement without the pre-amplifier both mean and most probable values are plotted (solid and open squares respectively).

ments could be performed and the pre-amplifier was still far from saturation. At $\Delta V_{GEM} > 490\ V$ the pulse-height resolution deteriorates considerably and the mean value (instead of the peak value) of the pulse-height distribution was used. Fig. 5.7 shows clearly that the signal from α-particles deviates from the exponential dependence when the total charge in the avalanche exceeds the value of 10^7 electrons, leading to saturation when it reaches $\sim 4\times10^7$e. (The saturation observed at 10^7 e is due to the saturation of the pre-amplifier).

This saturation effect is of prime importance for the anticipated application of the HBD in the PHENIX experiment where a small number of photoelectrons are to be detected in a high multiplicity environment of charged particles. It indicates that the total charge produced by a heavily ionizing particle is limited to below the Raether limit [89] and consequently its ability to cause a discharge is strongly suppressed.

The discharge probability was measured with segmented large triple-GEM detector. The results are shown in Fig. 5.8. Two measurements are presented in the figure, the measurement in the presence of α-particles and the measurement without α-particles . In both cases the gain was monitored at each voltage with the ^{55}Fe source. The dependence of the gain on voltage is presented in the figure together with the spark frequency as a function of the GEM voltage. The duration of each measurement was ~ 2000 s, i.e. the maximum number of sparks counted in the highest point was about 20. The present detector shows

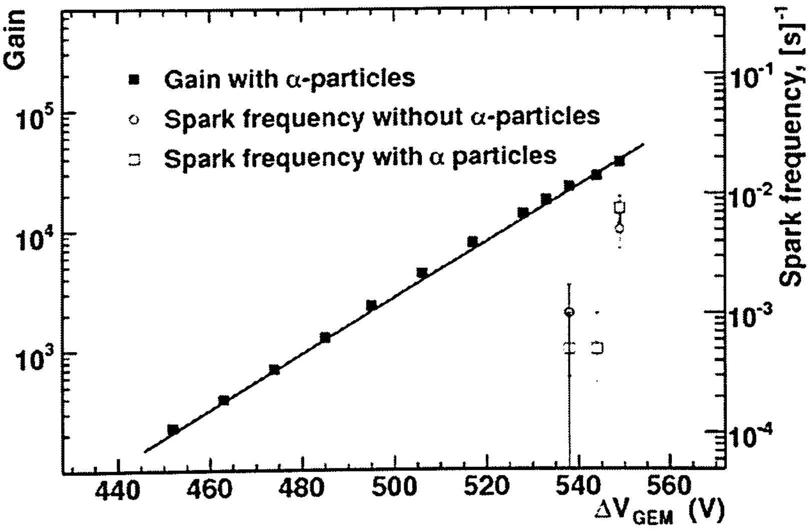

Figure 5.8: Spark frequency and detector gain as a function of voltage across GEM with and without α-particles irradiation.

non-negligible spark probability at a gain $\geq 2 \times 10^4$. The results demonstrate that the discharge limit does not depend on the presence of α-particles in the sensitive volume of the detector. Rather it seems that only local defects in the GEMs can provoke discharges and limit the gain of the device. During the series of tests the detector experienced a total number of 40 sparks but no sign of any degradation was observed in its performance and all three GEMs were still fully operational at the end of the tests.

5.4.3 Operation with the CsI reflective photocathode

In all the tests with the CsI photocathode a mercury lamp was used for irradiation. In order to determine the total emission from the photocathode itself without any amplification in the GEMs, a positive voltage between GEM1 and the mesh was applied, thus collecting the emitted photo-electrons in the mesh. The study of the triple GEM detector with a reflective photocathode was performed with $E_D = 0$ or slightly negative.

Fig. 5.9 shows the current to the PCB as a function of the GEM voltage for the small GEM setup. The measurements were done in Ar/CO_2 and CF_4. In the CF_4 curve one can clearly see two regions well described by two exponential dependencies on ΔV_{GEM} (see lines in Fig. 5.9): an initial slow increase of current at lower voltages related to the increase of the extraction of the photo-electrons from the CsI surface into the holes of GEM1 and a steep exponential increase at higher voltages due to amplification in the

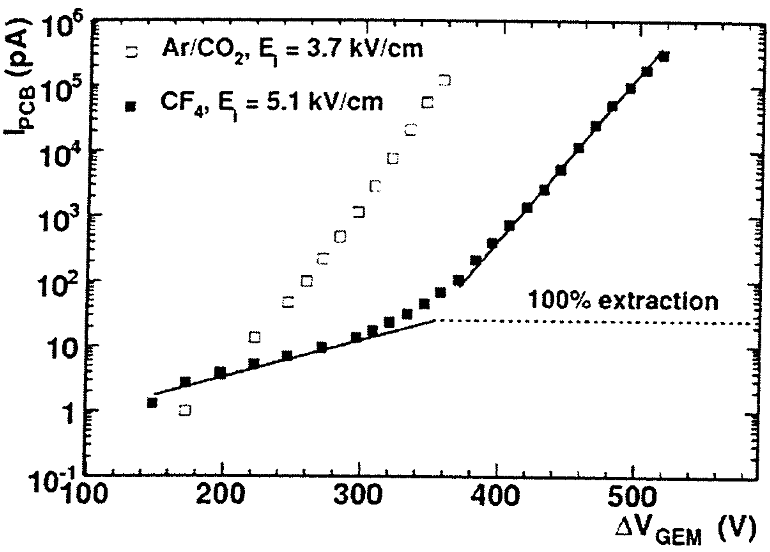

Figure 5.9: Current to the PCB as a function of ΔV_{GEM} .

GEMs. In Ar/CO$_2$ these two regions are not so clearly separated because amplification in this mixture starts at lower voltages. The electron extraction cannot exceed the maximum level of 100% indicated by the dashed line in Fig. 5.9 and corresponding to the photo-electron collected in the mesh. Thus, the gain is determined as the ratio between the current to the PCB and the extraction current. The latter is given by the first exponential curve up to $\Delta V_{GEM} = 350\ V$ and by the 100% extraction value at higher values of ΔV_{GEM} .

The gain as a function of ΔV_{GEM} for the setup with the reflective photocathode is shown in Fig. 5.10. In the same figure the data obtained with X-ray irradiation (^{55}Fe) are also shown in order to demonstrate that the different methods of gain measurement give similar results.

5.4.4 Ion back-flow in the triple GEM detector operating with a reflective photocathode.

The flow of positive ions to the CsI layer is one of the potential damaging factors that can cause aging of the photocathode [88, 90–93]. This factor is called ion back-flow and defined as the ratio between the current to the top electrode of GEM1 and the current to the PCB. This ratio depends on both the ion current itself and on the fraction of electron current flowing to the PCB. This is a convenient definition as it allows us to estimate the actual ion current from the measured signal at the PCB. In order to measure the current to

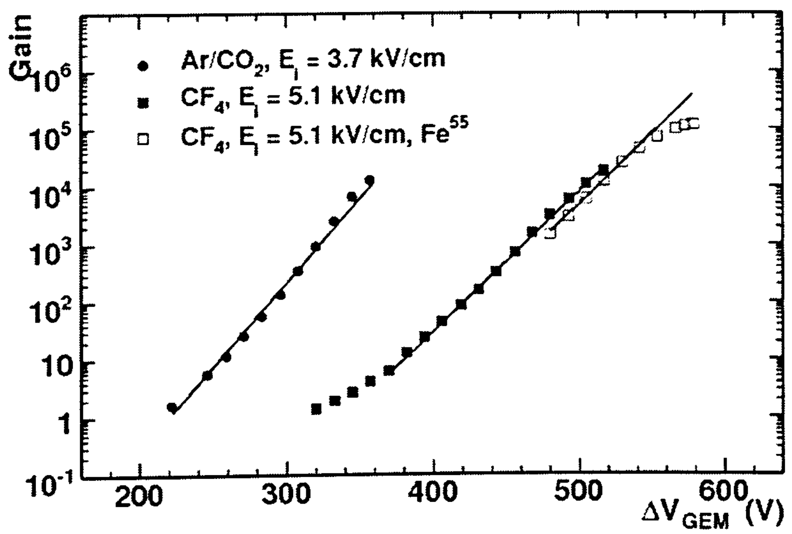

Figure 5.10: Gain as a function of ΔV_{GEM} for Ar/CO2 and CF$_4$ measured with the UV-lamp. For CF$_4$, the gain curve with ^{55}Fe is also shown. The lines are exponential fits to the data.

the photocathode the voltage was supplied separately to the top electrode of GEM1 with a CAEN N126 power supply. The voltages to all other electrodes were supplied through the resistive chain.

In Fig. 5.11 the ratio of the current to the photocathode and the current to the PCB (ion back-flow factor) as a function of gain is shown for different conditions. The errors on the plots are mainly due to the limited accuracy of the photocathode current measurements. The value of the induction field was changed by changing the corresponding resistor in the chain and the value indicated in the caption (5.1 kV/cm) is reached at a gain of 10^4.

In Fig. 5.11a one can see that in spite of the very different transport properties of the gases used in the measurements no significant dependence of the ion back-flow factor on the nature of the gas is observed as a function of gain and for different induction fields. The insensitivity of the ion back-flow factor to the particular gas at moderate gains is similar to that seen in [92]. It means that the efficiency of the transport of electrons and ions through the GEMs is the same for both gases and does not depend on diffusion.

The insensitivity of the ion back-flow factor to the electric field between the GEMs and in the GEM is demonstrated in Fig. 5.11b. Here the value of the ion back-flow factor as a function of gain is shown for three different electrostatic conditions: 1) standard, when the transfer field is equal to 3.4 kV/cm for both gaps and the induction field is equal to 5.1 kV/cm (the values refer to a gain of 10^4), 2) enhanced transfer field in both gaps, 3) reduced field in GEM1. From Fig. 5.11b one can see that neither variation in electrostatic conditions between nor inside the GEMs affect significantly the ion back-flow factor.

The only parameter which affects the value of the ion back-flow in our case is the induction field. Fig. 5.11c shows the value of the ion back-flow factor as a function of the gain for 3 values of the induction field. The field in the induction gap does not affect the ion flow itself as ions are produced in the holes of the last GEM or in their vicinity, collected into the holes and then transported to the top gap. The only factor that is affected is the electron flow from GEM3 to the PCB. Thus the ion back-flow factor being higher than one at low induction field means that a fraction of the electrons is collected at the bottom face of GEM3 and consequently the amount of ions reaching the photocathode can be larger than the amount of electrons collected at the PCB. The increase of the induction field improves the electron collection efficiency at the PCB and reduces the value of the ion back-flow factor. It is clear from the figure that for E_I above 5 kV/cm the collection efficiency does not increase significantly resulting in a minimum value of the ion back-flow factor of $\sim$ 0.7 at a gain of 10^4, consistent with results of [90, 91].

5.4.5 HBD response to minimum ionizing particles, α-particles and photoelectrons

A hadron blind detector is characterized by its insensitivity to hadrons, *i.e.* by a high hadron rejection factor while keeping a high detection efficiency for electrons. The hadron blindness property of the proposed detector is achieved by reversing the direction of the drift field E_D thereby pushing most of the ionization charges towards the mesh. With this reversed or negative drift field configuration, photoelectrons released from the CsI photocathode are still effectively collected into the GEM holes due to the strong electric field inside the holes which is typically of the order of 100 kV/cm. The hadron rejection factor and the photoelectron detection efficiency were systematically studied as a function of the drift field in measurements with α-particles , UV-photons and pions of 1 GeV/c (using secondary beam of negative particles (mainly pions) at KEK).

Fig. 5.12 shows the pulse height distribution, after pedestal subtraction, measured at KEK with 1 GeV/c pions for various values of E_D. The signal is expressed in terms of the primary ionization charge, using the ^{55}Fe spectrum measured under identical conditions. For E_D = +1 kV/cm, the measured mean amplitude is $\sim$18 e corresponding to a primary ionization of 120 charges/cm or 54 eV/ion-pairs (assuming an energy loss of

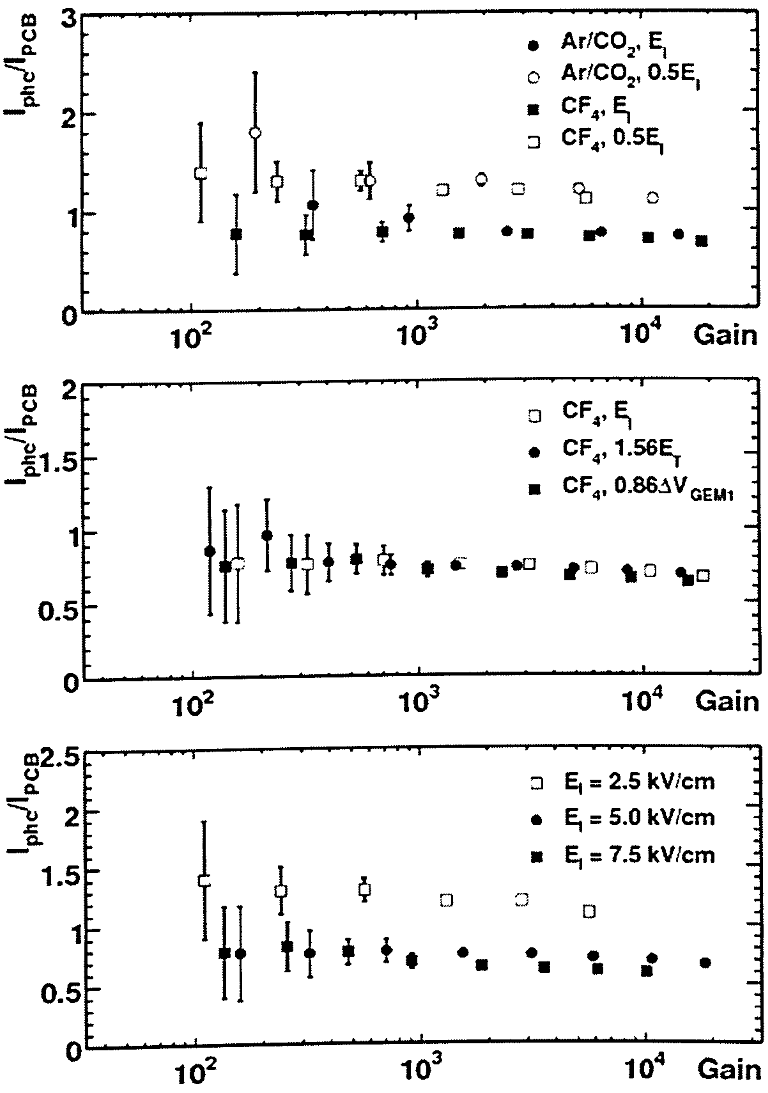

Figure 5.11: Ion back-flow factor as a function of gain. a) Comparison of ion back-flow factor for Ar/CO$_2$ and CF$_4$ and two different induction fields: standard $E_I = 5.1$ kV/cm and 0.5 E_I. The values refer to a gain of 10^4; b) Ion back-flow factor for different electrostatic conditions in the region between GEM1 and GEM3. c) Ion back-flow factor for 3 different values of the induction field.

dE/dx = 7 keV/cm). The spectrum is well reproduced by a Landau distribution characteristic of the energy loss of a minimum ionizing particle (MIP). The spectrum remains practically unchanged as long as E_D is positive as shown for two cases in the upper panels of the Fig. 5.12. When E_D is negative there is a sharp drop in the pulse height as the primary charges get repelled towards the mesh. The mean amplitude drops to approxi-

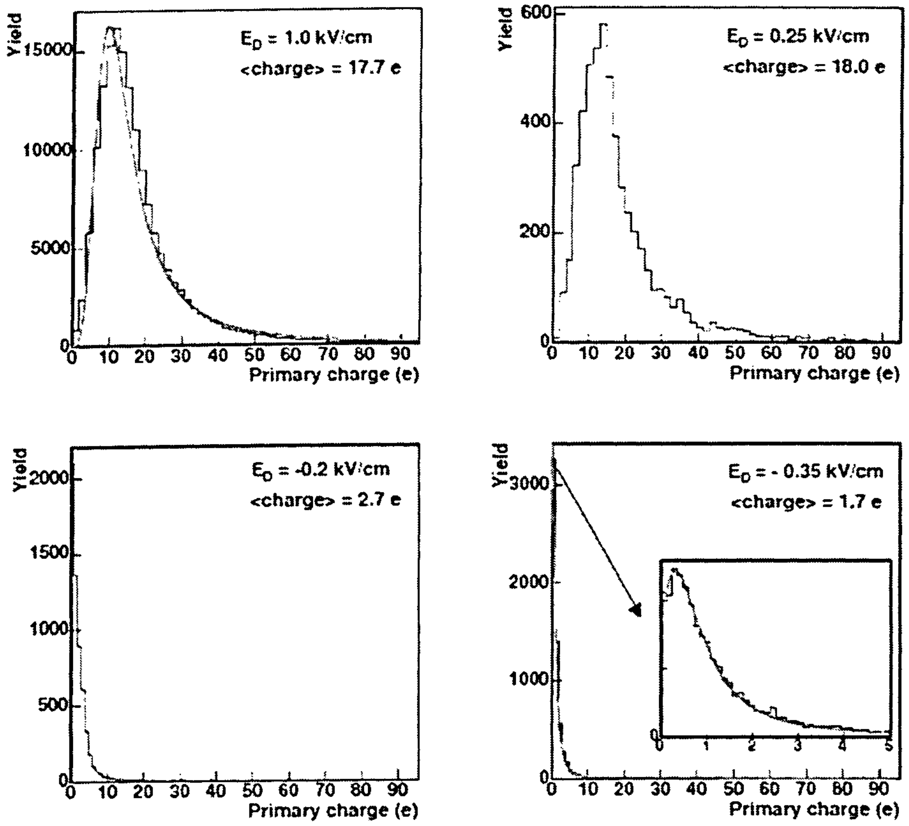

Figure 5.12: Pulse height spectra measured with 1 GeV/*c* pions at various values of the drift field E_D in the gap between the mesh and the upper GEM. The solid lines in the upper left and bottom right panels represent fits to Landau distributions of the measured spectra.

mately 10% of its value for a positive field. The remaining amplitude results from the collection of ionization charges (i) from a thin layer above the first GEM surface and (ii) from the entire first transfer gap which are subject to a two-stage amplification. The mean amplitude vs. E_D is shown in Fig. 5.13. The figure shows also the results of similar measurements performed with α-particles . In both cases the results are practically identical. The amplitude decreases sharply when the polarity of the drift field is switched and this occurs within a ΔE_D range of ~0.1 *kV*/cm.

The hadron rejection factor derived from the pion spectra measured at negative drift fields is shown in Fig. 5.14 as a function of a cut on the pion signal expressed in units of the primary charge. The rejection is limited by the long Landau tail and depends on the amplitude threshold that can safely be applied without compromising the electron ef-

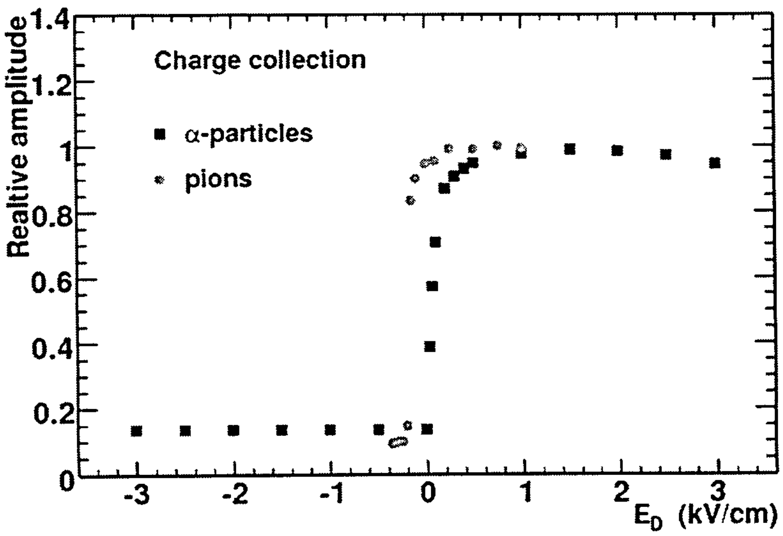

Figure 5.13: Collection of ionization charge vs. the drift field E_D in the gap between the mesh and the upper GEM.

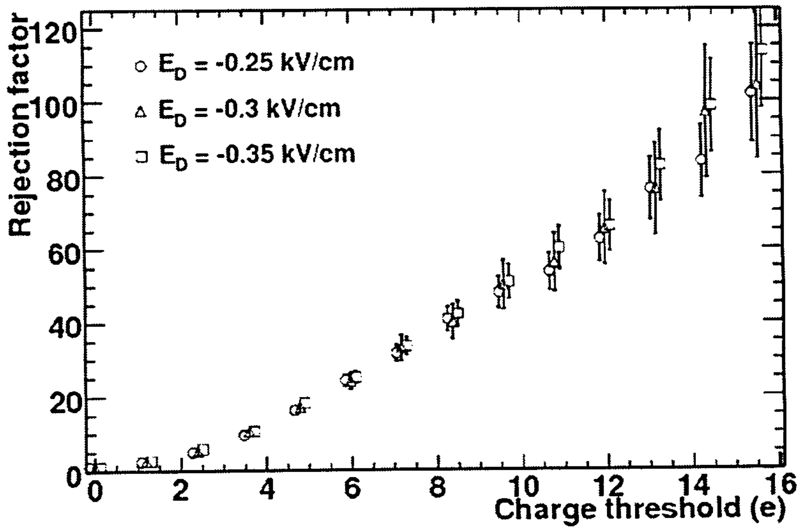

Figure 5.14: Hadron rejection factor derived from the pion pulse height distribution measured at negative drift field as a function of a cut on the pion signal expressed in units of the primary ionization charge. The error bars represent the statistical uncertainties.

ficiency. Rejection factors of the order of 50 can be achieved with an amplitude threshold of ~10 e. A much higher rejection factor is achieved by combining the amplitude response with the hit size. As already mentioned the pad readout consists of hexagonal pads with a size somewhat smaller than the blob size. Under these conditions charged hadrons produce single-pad hits whereas electrons most probably produce multiple pad hits thereby providing an additional powerful handle on the charged hadron rejection.

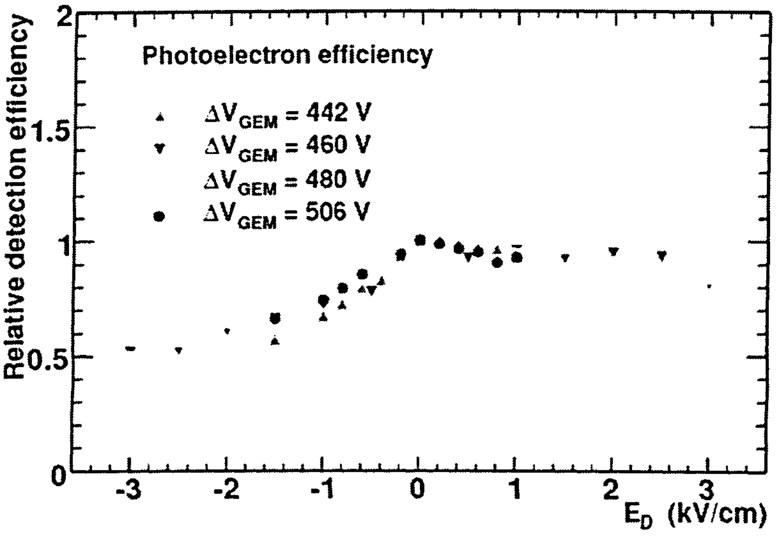

Figure 5.15: The photoelectron detection efficiencies at different gains vs. the electric field in the gap between the mesh and upper GEM.

Similar measurements to determine the electron detection efficiency were performed with UV-photons from a Hg lamp irradiating the CsI photocathode through the UV-transparent CaF_2 window. The current was measured at the PCB for values of the HV accross the GEMs varying from 442 to 506 *V* and corresponding to a gas gain variation of more than a factor of 40. The results are shown in Fig. 5.15. The various measurements have been normalized to 1 at E_D =0 to represent the relative detection efficiency and to allow an easy comparison between the measurements. The relative detection efficiency is practically independent of the field across the GEMs. The current slightly increases as the positive drift field decreases, reaching a maximum at 0 *kV*. A mild decrease in the current is observed as the drift field becomes more and more negative demonstrating that the detection efficiency of the photoelectrons remains very high even at negative drift fields of 1 *kV*/cm. Combining the results of Fig. 5.13 and Fig. 5.15 one sees that the best performance is achieved by applying a slightly negative field in the drift gap. The results presented here are consistent with those of [94].

5.4.6 CsI Quantum efficiency

The absolute quantum efficiency (QE) of the CsI was measured by a large number of groups. (See [88, 90, 95] for a comprehensive review and further references). Most of the measurements are in reasonable agreement with each other. However, none of these measurements were performed at a wavelength below 150 nm (or a photon energy above 8.3 *eV*). Since CF_4 is transparent up to 11.5 *eV* it was important to extend the measurements of the absolute QE of CsI as much as possible.

The determination of the absolute QE requires an absolutely calibrated light source, which is not available in most laboratories. Therefore, usually a relative method is used, namely the recording of the sample response relative to a "known" reference. In these measurements a calibrated photomultiplier tube (PMT) is used as a reference.

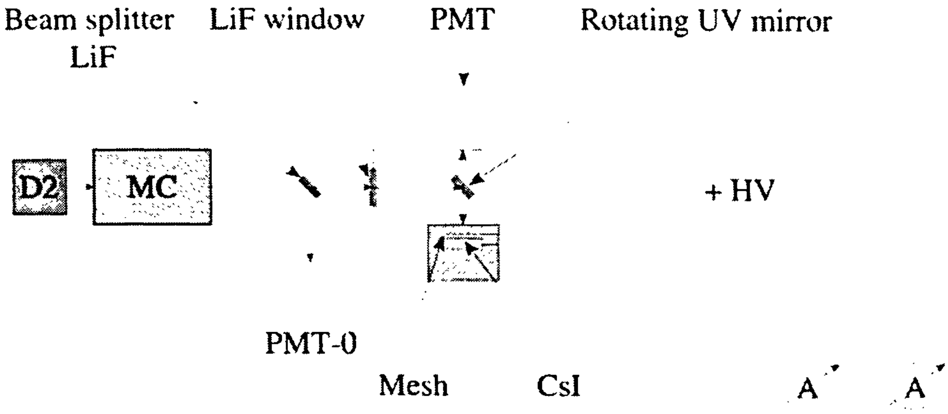

Figure 5.16: Schematic view of the experimental setup for measuring the quantum efficiency of the CsI layer.

The experimental setup used for the determination of the absolute quantum efficiency of the CsI layer is shown in Fig. 5.16. It includes a vacuum ultraviolet (VUV) monochromator (Jobin Ivon H20, 115-500nm) equipped with a deuterium lamp (L7293, 115-320nm), coupled via a *LiF* window (cut-off at 105 nm) to a detector box. The monochromator box also includes a *LiF* beam splitter which splits the beam between photomultiplier PMT-0 and the detector box. PMT-0 serves as a normalization to monitor the deuterium lamp intensity. The detector box included an absolutely calibrated photomultiplier tube PMT (Hamamatsu R6836) on one side and on the other side a box containing a small (3×3 cm^2) GEM foil on which a 2500Å layer of CsI was evaporated. Above the foil and at a distance of 1.5 *mm* from it was a mesh electrode which was at a positive voltage with respect to the foil. The detector box also had a UV-mirror which served to deflect the beam alternatively to the CsI layer and to the PMT. Collimators of 8 *mm* diameter were placed in front of the mesh and PMT, making sure that the solid angle seen by the photomultiplier and the CsI layer were exactly the same. By rotating the UV-mirror the current was measured in turn over the whole wavelength range on both devices.

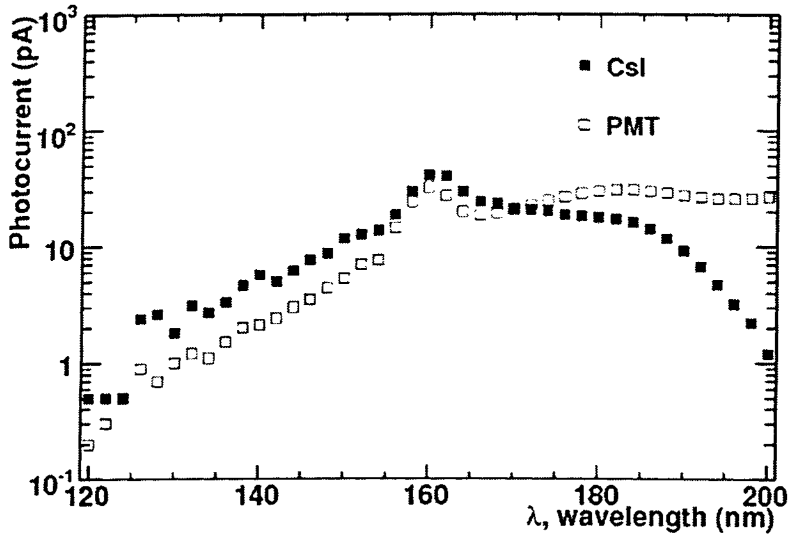

Figure 5.17: Photocurrent of CsI and PMT as function of wavelength.

The current of the CsI and photomultiplier as measured in vacuum is shown in Fig. 5.17. The measurements were done over the wavelength range of 120 - 200 nm (E = 6.2 - 10.3 *eV*). The measurements were repeated with CF_4 gas at atmospheric pressure. The total path in CF_4 was 23 cm. The absolute quantum efficiency of the CsI layer at a given wavelength λ is given by

$$(QE)_{CsI}(\lambda) = \frac{(QE)_{PMT}(\lambda) \times I_{CsI}(\lambda)}{I_{PMT}(\lambda) \times C1 \times C2} \tag{5.1}$$

where $(QE)_{PMT}(\lambda)$ is the absolute quantum efficiency of the PMT at the wavelength λ, I_{CsI} (λ) - the CsI photocathode current measured at that wavelength, $I_{PMT}(\lambda)$ - the PMT photomultiplier current at λ, C1 - the mesh transparency (C1 = 0.81), and C2 - the opacity of the CsI layer due to the GEM holes (C2 = 0.833).

Fig. 5.18 shows the CsI absolute quantum efficiency in vacuum and CF_4 plotted as a function of the photon energy. (Plotting the quantum efficiency as a function of photon energy has the advantage that the figure of merit N_0 is simply given by the area under the points). The present results are in very good agreement with those of [95] which covered

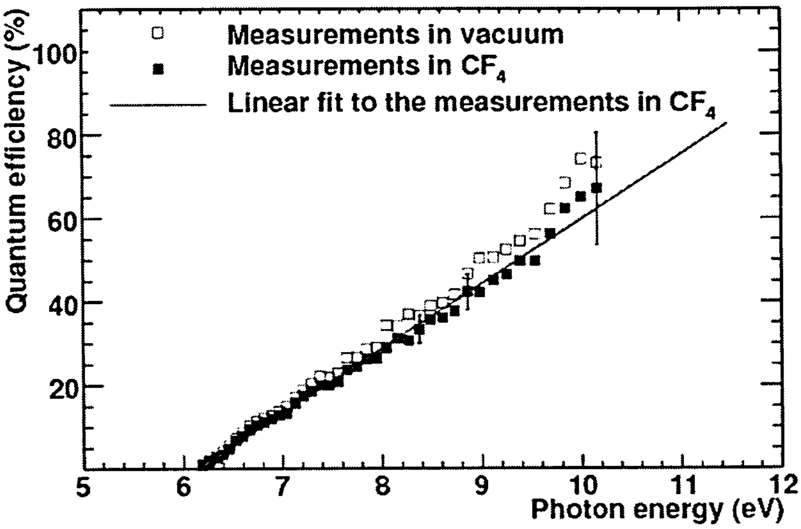

Figure 5.18: Absolute quantum efficiency of CsI in vacuum and CF_4 over bandwidth 6.2 - 10.3 *eV*.

the range 6-8.3 *eV*. The range of the measurements shown in Figs. 5.17 & 5.18 (120 - 200 nm, or 6.2 - 10.3 eV) was limited by the light intensity of the deuterium UV-lamp at $\sim$ 0.3 *eV*. A figure of merit N_0 derived over this bandwidth is 459 cm^{-1} (414 cm^{-1}) or an average QE value of 31% (28%) in vacuum (CF_4). However the useful range of UV-photons in the HBD extends up to the CF_4 cut-off which is at 11.5 *eV*. Extrapolating the data of Fig. 5.18 to 11.5 *eV* under the assumption of a linear dependence of the quantum efficiency vs. photon energy gives a figure of merit N_0 = 822 cm^{-1} or an average quantum efficiency of 55% in CF_4. For a 50 cm long radiator this N_0 value would correspond to $\sim$35 photo-electrons (after taking into account the losses due to the entrance mesh and the holes of the top GEM).

5.4.7 Aging studies

One can identify two possible sources of detector degradation under irradiation:

- Aging of the CsI photocathode due to ion back-flow and possible chemical reactions with active radicals formed in electron-ion avalanches in CF_4.
- Aging of the GEMs due to etching of metal or insulator surfaces and/or polymerization of pollutants from avalanches in CF_4 at the metal or insulator surfaces.

Both processes are determined by the total charge flowing through the detector which is the product of the photo-electron current collected into the holes of the first GEM and the total gain of the triple-GEM system. Assuming a gain of $\sim 10^4$ in the detector the total CF_4 charge flow through the HBD photo-detector is conservatively estimated to be 10-20 $\mu C/\mathrm{cm}^2$/year. Thus aging tests of the detector module were performed up to an accumulated charge between 100 and 200 $\mu C/\mathrm{cm}^2$ to represent several years of HBD operation.

The aging tests were performed so as to decouple the degradation of the photocathode from the deterioration of GEMs. We used two sources of radiation: a UV Hg-lamp and an ^{55}Fe X-ray source. The UV-lamp was used for continuous irradiation of the detector under test and the current to PCB was monitored. From time to time (once per 1-2 hours) the UV irradiation was stopped and the ^{55}Fe source was inserted into the detector for a short gain monitoring. During UV irradiation the electric field in the drift gap was kept at zero whereas during the X-ray irradiation the drift field was set to $\sim$1 kV/cm.

In Fig. 5.19 the results of two aging tests are shown. The first test (Fig. 5.19, top) was performed with a small triple-GEM detector. The test took about 1 day and the total charge accumulated was 140 $\mu C/\mathrm{cm}^2$. Based on our estimate this charge corresponds to about 10 years of HBD operation. It is seen that the gain derived from the measurements of the current during UV-irradiation and the gain measured from ^{55}Fe irradiation are very close to each other. After an initial gain drop of $\sim$10% in the first 2 hours, the performance was stable within 2%. The second aging test was performed with a large segmented triple-GEM set. This test was done at a lower rate than the first one and the detector accumulated a total charge of $\sim$150 $\mu C/\mathrm{cm}^2$ in 4 days (rather than in one day). As seen in the bottom panel of Fig. 5.19, the gain variations during the test did not exceed 20% and during the second half of the test they were even $\leq 5\%$. In the first 10 hours of the irradiation the gain derived from UV irradiation and the one determined from the measurements with ^{55}Fe source differed by $\sim$20%. This result indicates that the photocathode efficiency or collection efficiency of the photo-electrons into the first GEM holes was higher during that period.

After the first 10 hours both gains converged to the same value and followed a very similar dependence. As a result of these tests one can conclude that both photocathode efficiency and GEM gain do not exibit any dramatic change which can be interpreted as degradation of the detector.

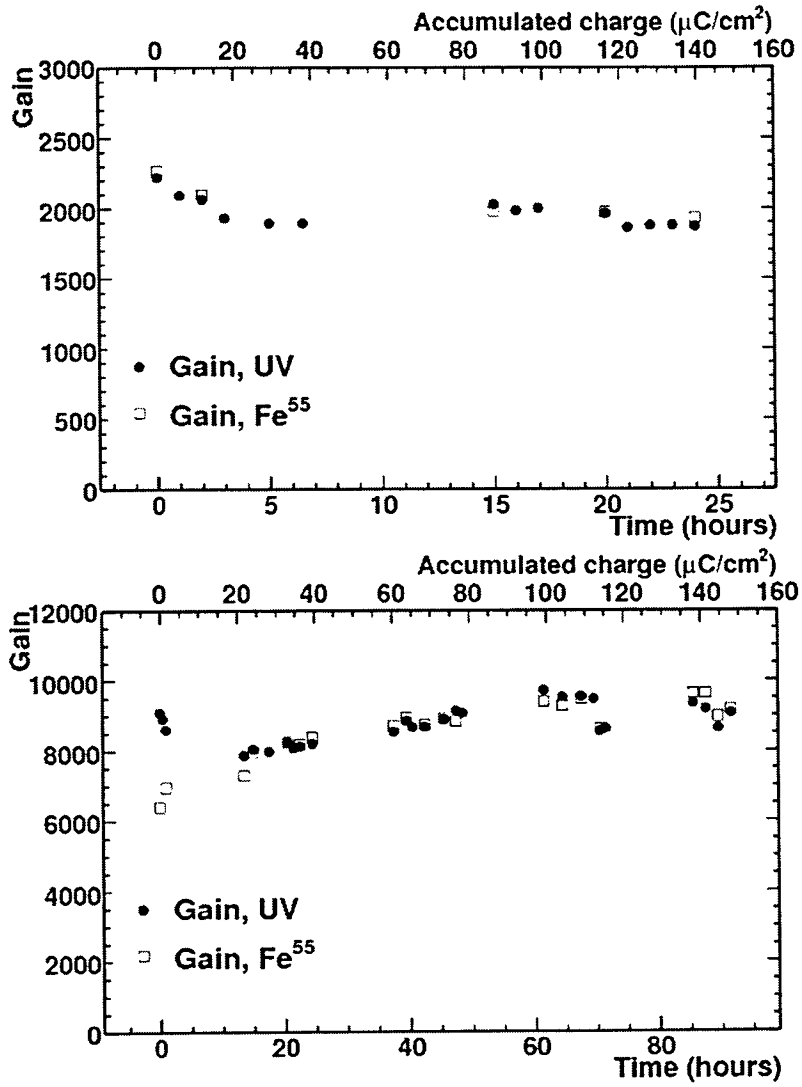

Figure 5.19: Results of aging tests with 3×3 cm (top panel) and 10×10 cm (bottom panel) triple GEM detector with CsI reflective photocathode. Open squares corresponds to the measurements with ^{55}Fe , solid squares represents the measurements with UV-irradiation.

5.5 HBD Construction

The R&D results demonstrated the validity of the proposed concept and the PHENIX collaboration approved the construction of the HBD detector as an upgrade project. The final mechanical design is shown on the left panel of Fig. 5.20. It consists of the two identical arms with a polygonal shape. Each arm covers 135° in azimuth and $|\eta| < 0.45$, so the acceptance of the HBD is larger than the acceptance of a PHENIX central arm which covers 90° in azimuth and $|\eta| < 0.35$. This allows for an efficient rejection of close pairs when only one track falls inside the fiducial acceptance of PHENIX. Each arm has six panels and each panel is equipped with two triple *GEM* detector modules with a size of $\sim 23 \times 27$ cm^2. The exploded view of the HBD panel and its components are shown on the right panel of Fig. 5.20 [96].

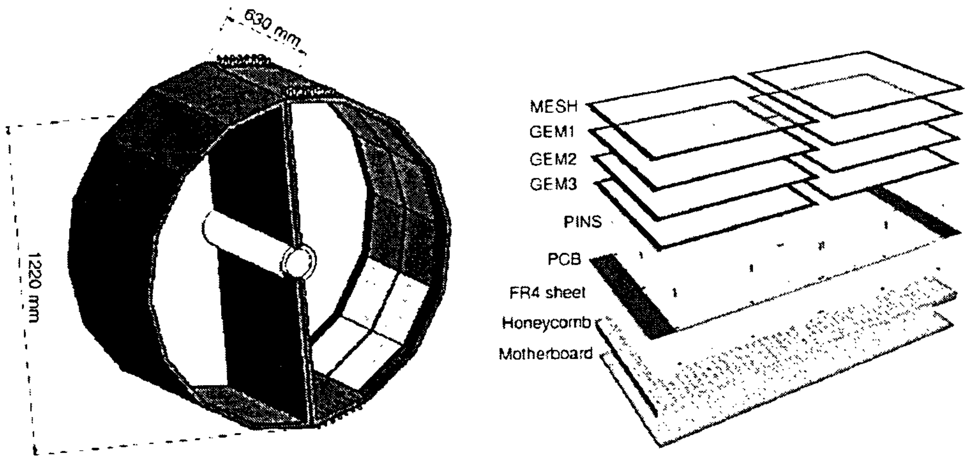

Figure 5.20: The final design of the HBD detector (left panel). Exploded view of the HBD panel

The construction stage was completed and the final HBD vessel has been installed in the PHENIX detector and is presently being commissioned with first in-beam operation foreseen in the RHIC Run of 2007.

Chapter 6

Summary

This thesis presented the analysis of the ϕ-meson production measured through the e^+e^- decay channel in $Au+Au$ and $d+Au$ collisions and through the K^+K^- decay channel in $Au+Au$ collisions at $\sqrt{s_{NN}}$ = 200 GeV using the PHENIX detector at the Relativistic Heavy Ion Collider at BNL. The obtained results include the transverse mass distribution, the centrality dependence of the yield, inverse slope parameter and the line-shape properties (mass and width) of the ϕ meson.

The first simultaneous measurement of the ϕ-meson production via the e^+e^- and K^+K^- decay channels as a function of centrality shows a possible increase of the yield in the dielectron channel with respect to the kaon one which could be related to the restoration of chiral symmetry. The line-shape analysis of the ϕ meson through the K^+K^- decay channel shows consistency of the mass centroid and width with the PDG values with a high precision of 1 MeV/c^2 ruling out hadronic re-scattering as a possible mechanism of the ϕ-meson yield difference in the two decay channels presented in this work.

As discussed in Section 1.3.3, theoretical models predict sizable changes in the ϕ meson mass and/or width which could manifest themselves in dramatic changes of the branching ratios of the ϕ meson decay via the leptonic and hadronic channels. The results presented in this thesis hints at a difference in the ϕ meson yield derived from the K^+K^- and the e^+e^- decay channels that could signal such in-medium modifications of the two branching ratios. However, the experimental errors are too large and a more definite statement about this difference cannot be made with the present data set and with the present capabilities of the PHENIX detector. The present results show neither a modification in the $\phi \rightarrow K^+K^-$ line shape analysis nor a clear difference in the branching ratios. The quality of the data did not allow us to perform a meaningful shape analysis in the $\phi \rightarrow e^+e^-$ decay channel. The large error bars prevent us also from making detailed comparisons with models. However, they leave ample room for some of the models listed inTable 1.2 to be compatible with the data.

The measured ratios of ϕ/π and ϕ/K point to the similarity in the production of hidden strangeness (ϕ), non-strange particles (π) and particles with open strangeness (kaons) at RHIC energy. The flatness of the ϕ/K ratio is in agreement with the measurements at lower energies while the centrality dependence of the ϕ/π ratio shows a trend different to that observed at the AGS and SPS energies.

Figure 6.1: WIS heavy-ion team and final HBD detector

Finally, the measurements in the dielectron channel using the PHENIX detector showed the need of an improvement of the PHENIX detector capability to measure low-mass dielectrons. A qualitatively new step in the measurement of low-mass dileptons is expected with the PHENIX detector upgrade with the Hadron Blind Detector - a novel Čerenkov detector proposed and developed by our group at the Weizmann Institute. This thesis presented a detailed description of the concept of the HBD and the results of a comprehensive R&D program carried out to demonstrate the validity of the proposed concept.

Bibliography

[1] M. Gell-Mann. *A schematic model of baryons and mesons.* Phys. Lett., **8** (1964) 214–215. 1.1

[2] G. Zweig. *An SU(3) model for strong interaction symmetry and its breaking. 2.* unpublished, 1964. 1.1, 1.3.2

[3] Y. Ne'eman. *Derivation of strong interactions from a gauge invariance.* Nucl. Phys., **26** (1961) 222–229. 1.1

[4] Edward V. Shuryak. *Quantum chromodynamics and the theory of superdense matter.* Phys. Rept., **61** (1980) 71–158. 1.1

[5] F. Karsch. *Lattice QCD at high temperature and density.* Lect. Notes Phys., **583** (2002) 209–249. 1.1

[6] Z. Fodor and S. D. Katz. *Critical point of QCD at finite T and μ, lattice results for physical quark masses.* JHEP, **04** (2004) 050. 1.1

[7] Benjamin W. Lee. *Chiral Dynamics.* Gordon and Breach, New York, 1972. 1.1

[8] R. Rapp and J. Wambach. *Chiral symmetry restoration and dileptons in relativistic heavy-ion collisions.* Adv. Nucl. Phys., **25** (2000) 1. 1.1

[9] S. Klimt, M. Lutz, and W. Weise. *Chiral phase transition in the SU(3) Nambu and Jona-Lasinio model.* Phys. Lett., **B249** (1990) 386–390. 1.1

[10] D. Boyanovsky. *Phase transitions in the early and the present universe: From the big bang to heavy ion collisions*, 2001, hep-ph/0102120. 1.2

[11] M. Harrison, T. Ludlam, and S. Ozaki. *RHIC project overview.* Nucl. Instr. and Meth., **A499** (2003) 235–244. 1.2, 2.1

[12] Berndt Muller. *Physics and signatures of the quark - gluon plasma.* Rept. Prog. Phys., **58** (1995) 611–636. 1.3

[13] John W. Harris and Berndt Muller. *The search for the quark-gluon plasma.* Ann. Rev. Nucl. Part. Sci., **46** (1996) 71–107. 1.3

[14] W. M. Yao *et.al. Review of particle physics.* J. Phys., **G33** (2006) 1–1232. 1.1

[15] S. Okubo. *ϕ meson and unitary symmetry model.* Phys. Lett., **5** (1963) 165–168. 1.3.2

[16] J. Iizuka. *Systematics and phenomenology of meson family.* Prog. Theor. Phys. Suppl., **37** (1966) 21–34. 1.3.2

[17] J. Rafelski and B. Muller. *Strangeness production in the quark - gluon plasma.* Phys. Rev. Lett., **48** (1982) 1066. 1.3.2

[18] J. Rafelski. *Strangeness production in the quark gluon plasma.* Nucl. Phys., **A418** (1984) 215c–235c. 1.3.2

[19] A. Shor. *ϕ meson production as a probe of the quark gluon plasma.* Phys. Rev. Lett., **54** (1985) 1122–1125. 1.3.2, 1.3.3

[20] G. E. Brown and Mannque Rho. *Scaling effective lagrangians in a dense medium.* Phys. Rev. Lett., **66** (1991) 2720–2723. 1.3.3

[21] Tetsuo Hatsuda and Su Houng Lee. *QCD sum rules for vector mesons in nuclear medium.* Phys. Rev., **C46** (1992) 34–38. 1.3.3

[22] R. Rapp. *Signatures of thermal dilepton radiation at rhic.* Phys. Rev., **C63** (2001) 054907. 1.3.3, 1.2, 1.6

[23] Subrata Pal, C. M. Ko, and Zi-wei Lin. *ϕ meson production in relativistic heavy ion collisions.* Nucl. Phys., **A707** (2002) 525–539. 1.3.3, 1.2

[24] E. Santini, G. Burau, Amand Faessler, and C. Fuchs. *Medium effects on phi decays to dilepton and kaon antikaon pairs in relativistic heavy ion reactions.* Eur. Phys. J., **A28** (2006) 187–192. 1.3.3

[25] D. Lissauer and Edward V. Shuryak. *K meson modification in hot hadronic matter may be detected via ϕ meson decays.* Phys. Lett., **B253** (1991) 15–18. 1.2

[26] Pin-zhen Bi and Johann Rafelski. *Decay of ϕ in hot matter.* Phys. Lett., **B262** (1991) 485–491. 1.2

[27] Jean Paul Blaizot and Ramon Mendez Galain. *ϕ and K mesons in hot dense matter.* Phys. Lett., **B271** (1991) 32–36. 1.2

[28] C. M. Ko, P. Levai, X. J. Qiu, and C. T. Li. *Phi meson in dense matter.* Phys. Rev., **C45** (1992) 1400–1402. 1.2

[29] M. Asakawa and C. M. Ko. *Phi meson mass in hot and dense matter.* Nucl. Phys., **A572** (1994) 732–748. 1.2

[30] M. Asakawa and C. M. Ko. *Seeing the QCD phase transition with phi mesons.* Phys. Lett., **B322** (1994) 33–37. 1.2

[31] M. Asakawa and C. M. Ko. *Secondary phi meson peak as a indicator of QCD phase transition in ultrarelativistic heavy ion collisions.* Phys. Rev., **C50** (1994) 3064–3068. 1.2

[32] H. Kuwabara and T. Hatsuda. *ϕ meson in nuclear matter.* Prog. Theor. Phys., **94** (1995) 1163–1168. 1.2

[33] Chungsik Song. *Effective mass of ϕ mesons at finite temperature.* Phys. Lett., **B388** (1996) 141–146. 1.2

[34] Abhijit Bhattacharyya, Sanjay K. Ghosh, S. C. Phatak, and Sibaji Raha. *In-medium effects on the ϕ meson.* Phys. Rev., **C55** (1997) 1463–1466. 1.2

[35] Wade Smith and Kevin L. Haglin. *Collision broadening of the phi meson in baryon rich hadronic matter.* Phys. Rev., **C57** (1998) 1449–1453. 1.2

[36] Y. Akiba *et.al. Production of ϕ mesons in central ^{28}Si + ^{196}Au collisions at* 14.6A GeV/*c*. Phys. Rev. Lett., **76** (1996) 2021–2024. 1.4

[37] B. B. Back *et.al. Production of ϕ mesons in Au + Au collisions at* 11.7A GeV/*c*. Phys. Rev., **C69** (2004) 054901. 1.4, 1.7, 4.12, 4.4.2, 4.13

[38] B. Alessandro *et.al. ϕ production in Pb - Pb collisions at* 158 GeV/*c per nucleon incident momentum.* Phys. Lett., **B555** (2003) 147–155. 1.4, 1.8

[39] S. V. Afanasev *et.al. Production of ϕ mesons in p+p, p+Pb and central Pb+Pb collisions at E_{beam}* = 158A GeV. Phys. Lett., **B491** (2000) 59–66. 1.4, 1.8

[40] Edward V. Shuryak. *What have we learned and want to learn from heavy ion collisions at CERN SPS.* Nucl. Phys., **A661** (1999) 119–129. 1.4

[41] D. Adamova *et.al. Leptonic and charged kaon decay modes of the ϕ meson measured in heavy-ion collisions at the CERN SPS.* Phys. Rev. Lett., **96** (2006) 152301. 1.4, 1.8, 4.4.2, 4.13

[42] A. De Falco *et.al. ϕ production in p-A and In-In collisions.* Nucl. Phys., **A774** (2006) 719–722. 1.4, 4.4.2, 4.13

[43] R. Muto *et.al. First observation of ϕ-meson mass modification in nuclear medium.* Nucl. Phys., **A774** (2006) 723–726. 1.4, 1.9, 4.3, 4.10

[44] R. Muto et al. *Evidence for in-medium modification of the ϕ meson at normal nuclear density.* Phys. Rev. Lett., **98** (2007) 042501. 1.4, 1.9

[45] C. M. Ko and B. H. Sa. *Phi meson production in hadronic matter.* Phys. Lett., **B258** (1991) 6–10. 1.4

[46] F. Klingl, T. Waas, and W. Weise. *Modification of the ϕ meson spectrum in nuclear matter.* Phys. Lett., **B431** (1998) 254–262. 1.4

[47] D. Cabrera and M. J. Vicente Vacas. *Phi meson mass and decay width in nuclear matter.* Phys. Rev., **C67** (2003) 045203. 1.4

[48] M. Naruki et al. *Experimental signature of the medium modification for ρ and ω mesons in 12 GeV p+A reactions.* Phys. Rev. Lett., **96** (2006) 092301. 1.4

[49] D. Trnka et al. *First observation of in-medium modifications of the ω meson.* Phys. Rev. Lett., **94** (2005) 192303. 1.4

[50] G. Agakichiev et al. *e^+e^- pair production in Pb+Au collisions at 158 GeV per nucleon.* Eur. Phys. J., **C41** (2005) 475–513. 1.4

[51] S. Damjanovic et al. *First measurement of the rho spectral function in nuclear collisions.* Nucl. Phys., **A774** (2006) 715–718. 1.4

[52] K. H. Ackermann *et.al. STAR detector overview.* Nucl. Instr. and Meth., **A499** (2003) 624–632. 2.1

[53] B. B. Back *et.al. The PHOBOS detector at rhic.* Nucl. Instr. and Meth., **A499** (2003) 603–623. 2.1

[54] M. Adamczyk *et.al. The BRAHMS experiment at rhic.* Nucl. Instr. and Meth., **A499** (2003) 437–468. 2.1

[55] K. Adcox *et.al. PHENIX detector overview.* Nucl. Instr. and Meth., **A499** (2003) 469–479. 2.1

[56] M. Allen *et.al. PHENIX inner detectors.* Nucl. Instr. and Meth., **A499** (2003) 549–559. 2.2.3

[57] C. Adler *et.al. The RHIC zero-degree calorimeters.* Nucl. Instr. and Meth., **A499** (2003) 433–436. 2.2.3

[58] K. Adcox *et.al. PHENIX central arm tracking detectors.* Nucl. Instr. and Meth., **A499** (2003) 489-507. 2.2.3

[59] K. Adcox *et.al. Construction and performance of the PHENIX pad chambers.* Nucl. Instr. and Meth., **A497** (2003) 263–293. 2.2.3

[60] M. Aizawa *et.al. PHENIX central arm particle id detectors.* Nucl. Instr. and Meth., **A499** (2003) 508-520. 2.2.3

[61] L. Aphecetche *et.al. PHENIX calorimeter.* Nucl. Instr. and Meth., **A499** (2003) 521–536. 2.2.3

[62] K. Adcox *et.al. Measurement of single electrons and implications for charm production in* $Au+Au$ *collisions at* $\sqrt{s_{NN}}$ = 130 GeV. Phys. Rev. Lett., **88** (2002) 192303. 2.2.3

[63] S. S. Adler *et.al. Centrality dependence of charm production from single electrons measurement in au + au collisions at s(nn)**(1/2) = 200-gev.* Phys. Rev. Lett., **94** (2005) 082301. 2.2.3

[64] Sergey A. Butsyk. *Study of open charm production in* $p+p$ *collisions at* $\sqrt{s_{NN}}$ = 200 GeV. PhD thesis, Stony Brook Unversity, 2005. 2.2.3

[65] S. S. Adler *et.al. PHENIX on-line systems.* Nucl. Instr. and Meth., **A499** (2003) 560–592. 2.3.1

[66] Miklos Gyulassy and Xin-Nian Wang. *HIJING 1.0: A Monte Carlo program for parton and particle production in high-energy hadronic and nuclear collisions.* Comput. Phys. Commun., **83** (1994) 307. 3.2.2

[67] S. S. Adler et al. *Systematic studies of the centrality and* $\sqrt{s_{NN}}$ *dependence of* $\frac{dE_T}{d\eta}$ *and* $\frac{dN_{ch}}{d\eta}$ *in heavy ion collisions at mid-rapidity.* Phys. Rev., **C71** (2005) 034908. 3.2.2

[68] C. Y. Wong. *Introduction to high-energy heavy ion collisions.* World Scientific Publishing Co. Pte. Ltd., Singapore, 1994. 3.2.4

[69] Beat Hahn, D. G. Ravenhall, and Robert Hofstadter. *High-energy electron scattering and the charge distributions of selected nuclei.* Phys. Rev., **101**(3) (1956) 1131–1142. doi: 10.1103/PhysRev.101.1131. 3.2.4

[70] G. I. Kopylov. *Like particle correlations as a tool to study the multiple production mechanism.* Phys. Lett., **B50** (1974) 472–474. 3.5.1

[71] D. Drijard, H. G. Fischer, and T. Nakada. *Study of event mixing and its application to the extraction of resonance signals.* Nucl. Instr. and Meth., **A225** (1984) 367. 3.5.1

[72] D. L'Hote. *About resonance signal extraction from multiparticle data: combinatorics and event mixing methods.* Nucl. Instr. and Meth., **A337** (1994) 544–556. 3.5.1

[73] Ralf Averback. *EXODUS a new lepton-pair generator.* http://www.phenix.bnl.gov/phenix/WWW/publish/ralf/talks/montauk-2001/, 2001. 3.7

[74] S. S. Adler *et.al. Production of* ϕ *mesons at mid-rapidity in* $\sqrt{s_{NN}}$ = 200 GeV *Au+Au collisions at RHIC.* Phys. Rev., **C72** (2005) 014903. 4

[75] Stephen C. Johnson, Barbara V. Jacak, and Axel Drees. *Rescattering of vector meson daughters in high-energy heavy ion collisions.* Eur. Phys. J., **C18** (2001) 645–649. 4.3

[76] Richard Seto. *Light vector mesons from* $d+Au$ *in PHENIX.* J. Phys., **G30** (2004) S1017–S1022. 4.4.1, 4.4.2

[77] Yu. Riabov. *Measurement of leptonic and hadronic decays of* ω- *and* ϕ*-mesons at RHIC by PHENIX*, 2007, nucl-ex/0702022. 4.4.1, 4.4.2

[78] S. S. Adler *et.al. Identified charged particle spectra and yields in* $Au+Au$ *collisions at* $\sqrt{s_{NN}}$ = 200 GeV. Phys. Rev., **C69** (2004) 034909. 4.4.1

[79] Claudia Hohne. *System-size dependence of strangeness production in heavy-ion collisions at 158 A GeV.* PhD thesis, Philipps-Universitat Marburg, 2003. 4.12, 4.4.2

[80] John Adams *et.al.* *ϕ meson production in Au+Au and $p+p$ collisions at $\sqrt{s_{NN}}$ =* 200 GeV. Phys. Lett., **B612** (2005) 181–189. 4.4.1

[81] C. Alt et al. *System-size dependence of strangeness production in nucleus nucleus collisions at $\sqrt{s_{NN}}$* = 17.3 GeV. Phys. Rev. Lett., **94** (2005) 052301. 4.4.2, 4.13

[82] Eftychios Felix Matathias. *Identified particle production in $p+p$ and $d+Au$ collisions at RHIC energies.* PhD thesis, Stony Brook Unversity, 2004. 4.4.2

[83] Alberica Toia. *Measurement of low mass dielectron continuum in $\sqrt{s_{NN}}$* = 200 GeV *Au + Au collisions in the PHENIX experiment at RHIC.* Eur. Phys. J., **C49** (2007) 243. 5.1, 5.1

[84] A. Kozlov *et.al.* *Development of a triple GEM UV-photon detector operated in pure CF_4 for the PHENIX experiment.* Nucl. Instr. and Meth., **A523** (2004) 345–354. 5.1, 5.3.1, 5.4.2

[85] Z. Fraenkel *et.al.* *A hadron blind detector for the PHENIX experiment at RHIC.* Nucl. Instr. and Meth., **A546** (2005) 466–480. 5.1, 5.4.2

[86] A. Kozlov Z. Fraenkel, B. Khachaturov, A. Milov, D. Mukhopadhyay, D. Pal, I. Ravinovich, I. Tserruya, and S. Zhou. *The PHENIX Collaboration. Technical Note* 391. http://www.phenix.bnl.gov/phenix/WWW/publish/tserruya/1-06-HBD-proposal.ps, 2001. 5.2

[87] F. Sauli. *GEM: A new concept for electron amplification in gas detectors.* Nucl. Instr. and Meth., **A386** (1997) 531–534. 5.2

[88] B. K. Singh, E. Shefer, A. Breskin, R. Chechik, and N. Avraham. *CsBr and CsI UV photocathodes: New results on quantum efficiency and aging.* Nucl. Instr. and Meth., **A454** (2000) 364–378. 5.3.1, 5.4.4, 5.4.6

[89] H. Raether. *The development of the electron avalanche in the spark canal.* Zeitschrift fur Physik, **112** (1939) 464–489. 5.4.2

[90] D. Mormann, A. Breskin, R. Chechik, and B. K. Singh. *On the efficient operation of a CsI-coated GEM photon detector.* Nucl. Instr. and Meth., **A471** (2001) 333–339. 5.4.4, 5.4.6

[91] D. Mormann, A. Breskin, R. Chechik, and D. Bloch. *Evaluation and reduction of ion back-flow in multi-GEM detectors.* Nucl. Instr. and Meth., **A516** (2004) 315–326. 5.4.4

[92] A. Bondar, A. Buzulutskov, Lev I. Shekhtman, and A. Vasiljev. *Study of ion feedback in multi-GEM structures.* Nucl. Instr. and Meth., **A496** (2003) 325–332. 5.4.4

[93] F. Sauli, S. Kappler, and L. Ropelewski. *Electron collection and ion feedback in GEM-based detectors.* IEEE Trans. Nucl. Sci., **50** (2003) 803–808. 5.4.4

[94] D. Mormann, A. Breskin, R. Chechik, P. Cwetanski, and B. K. Singh. *A gas avalanche photomultiplier with a CsI-coated GEM.* Nucl. Instr. and Meth., **A478** (2002) 230–234. 5.4.5

[95] A. Breskin. *CsI UV photocathodes: History and mystery.* Nucl. Instr. and Meth., **A371** (1996) 116–136. 5.4.6, 5.4.6

[96] I. Tserruya. *Report on the Hadron Blind Detector for the PHENIX experiment.* Nucl. Instr. and Meth., **A563** (2006) 333–337. 5.5